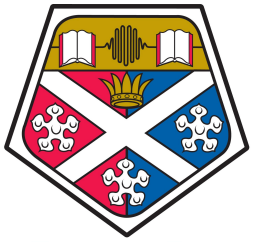

University of Strathclyde

Experimental investigation of the emission of high-brightness extreme ultraviolet radiation from laser-plasma interactions

Lewis Ramsay Reid

A thesis presented for the degree of Doctor of Philosophy in Physics

Department of Physics, University of Strathclyde

Supervisors:

Prof. Dino A. Jaroszynski

Dr Enrico Brunetti

2018

This thesis is the result of the author's original research. It has been composed by the author and has not been previously submitted for examination which has led to the award of a degree.

Signed:

Date:

Abstract

The laser wakefield accelerator is a novel particle accelerator that takes advantage of the large electric fields generated by separating oppositely charged particles in plasma. The ponderomotive force of an intense, ultra-short duration, laser pulse drives density waves in under-dense plasma to create an accelerating structure similar to that of a radio-frequency cavity, but with a longitudinal field strength more than a thousand times larger, and travelling at a velocity close to that of light. Electrons can gain a sufficiently high longitudinal velocity on reaching the back of the accelerating structure to become trapped inside it. These injected electrons then "surf" the plasma wave to reach energies that can exceed several GeV on the centimetre scale. This enables millimetre sized acceleration stages that act as ultra-compact table-top sources of both high energy particles and radiation beams.

To date, theoretical and experimental work on radiation production from the laser wakefield accelerator has focussed on the emission of few keV to 1 MeV photons from electrons undergoing betatron oscillations inside the plasma structure. This thesis, in contrast, presents one of the first experimental investigations of radiation emitted at extreme ultraviolet wavelengths approaching the water window. The spectral, spatial and coherence properties of radiation beams produced by the laser plasma interaction are measured. In addition, a Kirkpatrick-Baez microscope focusing optic is developed for proof-of-principle application experiments to demonstrate the usefulness of the source. The spectra of hard x-ray betatron radiation is measured and first tests of the Kirkpatrick-Baez microscope undertaken to focus the radiation to a small spot size.

Extreme ultraviolet (XUV) radiation has been observed between 3 and 31 nm with

a large number of photons (7.6×10^{13} photons sr^{-1} at 20 nm) passing through the spectrometer slit. Measurements with a series of double slits show that the source has a high degree of longitudinal coherence with a source size diameter of 50 µm. The source size and spectral measurements give a calculated peak brightness of 6.4×10^{27} photons/s/mm^2/$mrad^2$/0.1% BW, occurring at 7.5 nm, assuming the duration of the radiation pulse is Fourier limited to 11 as.

Acknowledgements

The completion of a PhD thesis is never achieved by a single person but rather by a single candidate supported in many different ways by those around them. In particular, the completion of this thesis would have not been possible without the following:

- Prof. Dino Jarozynski for allowing me to take on such an interesting and challenging topic and for his constant support and guidance throughout the duration of my PhD.
- Dr Enrico Brunetti for helping me build my understanding of the theory required for laser wakefield acceleration, teaching me how to build and run experiments, methods of data analysis, discussions on interpretation and getting me started with PIC codes that produced a few excellent figures in this thesis.
- Dr Gregor Welsh for keeping the laser on and running in the challenging (and wet!) conditions in the Colville laboratory.
- Dr Enrico Brunetti, Dr Gregory Vieux and Dr Gregor Welsh for spending countless hours in the laboratory collecting data with me during the XUV run at the beginning of my project while answering all of my technical questions and curiosities about all of the experimental equipment and how it all worked.
- Dr Mohammed Shahzad for his assistance in procuring and setting up the KB microscope
- Dr Roman Spesyvtsev, Dr Mohammed Shahzad, Dr Antoine Maitrallain and Dr Wentao Li for working tirelessly on getting the laser to work as well as possible

in the SCAPA laboratory and working with me on setting up the beamline for the x-ray spectrum and x-ray focusing experiments.

- Tom McCanny and Tommy McGrory for their technical support.

- My examiners Professor Greg Tallents and Dr Carol Trager-Cowan for taking time to review this thesis and for helping me to improve this manuscript.

- My fellow students, Karolina Kokurewicz, Giorgio Battaglia, Maria Weikum, Lucas Iñigo Gamiz and Andrzej Kornaszewski among others, for your advice and discussions.

- All of the adult leaders and young people of the 1^{st} Kilsyth Scout group for providing me with the opportunity to escape from work and think about something else on a regular basis. In particular, Marion, Richard, Ewan, Robert, Fiona, Robbie, Kelly and Tim, regular pack nights and weekend camps with you has been my privilege.

- Finally and most importantly to my family, Mum, Dad and Charlotte, for celebrating the good days with me and supporting me through the tough ones.

Role of the author

Experimental design, equipment alignment and data collection for the XUV campaign was performed by the author with support and supervision from Dr Enrico Brunetti, Dr Gregory Vieux and Dr Gregor Welsh. Particle in cell simulations were done by the author with data visualisation using a program written by Dr Enrico Brunetti. Data analysis, including scripts, is the work of the author with the exception of the XUV spectra data where software written by Dr Enrico Brunetti was used. Data for the x-ray spectrum and focusing measurements were recorded with the aid of Dr Roman Spesyvtsev, Dr Mohammed Shahzad, Dr Antoine Maitrallain and Dr Gregory Vieux. The single photon counting script was written in collaboration with Dr Roman Spesyvtsev.

Contents

Chapter 1

Introduction

This thesis presents an experimental investigation of the emission of extreme ultraviolet (XUV) radiation with wavelengths between 3 and 31 nm, and hard x-rays with a few keV photon energy produced by the interaction of high intensity laser pulses with underdense plasma. The experiments presented were conducted on the Advanced Laser Plasma High-energy Accelerators towards x-rays (ALPHA-X), beamline using the Terahertz to Optical Pulse Source (TOPS) 40 TW laser, initially in the ALPHA-X laboratory and subsequently at the Scottish Centre for the Applications of Plasma-based Accelerators (SCAPA). The commissioning of a new Kirkpatrick-Baez microscope focusing optic is also presented, which includes alignment for investigating the feasibility of using radiation from laser wakefield accelerators in potential applications.

1.1 Accelerators as a tool for science and industry

Since their initial development, in the early 20^{th} century, particle accelerators have become ubiquitous and powerful tools for both basic and applied science. Accelerators in the form of colliders are perhaps the best known to the general public. They have enabled exploration of the structure of matter, which has lead to the discovery of elementary particles, including the Higgs Boson by CERN in 2012 [1, 2]. However, most accelerators are used for medical treatment [3, 4], isotope production [5], and numerous industrial applications, including sterilisation and polymer processing [6]. Many accel-

erators are dedicated to producing secondary radiation in the form of electromagnetic radiation across the whole spectrum from terahertz frequencies to energetic gamma rays. The photon beams thus produced have numerous applications including imaging in medical and security settings, diffraction experiments to determine the structure of molecules and semiconductors, and time-resolved spectroscopy to measure reaction paths of molecules.

Radiation is produced from particle accelerator beams when the charged particles are accelerated, which can be produced by several mechanisms. Bremsstrahlung radiation is produced when particles incident on nuclei decelerate, giving rise to emission of high energy photons [7]. Inducing periodic motion of charged particles also gives rise to the emission of radiation. Undulators and wigglers use a series of permanent magnets with alternating field direction to give the particles an oscillation perpendicular to their propagation direction [8]. These devices can produce radiation from the microwaves to the hard x-ray region of the electromagnetic spectrum, with wavelengths as short as 0.1 nm and peak brilliance as high as 2×10^{34} photons/s/mm^2/mrad^2/0.1% BW [9, 10]. Similarly, and relevant to this thesis, betatron motion in the focussing field of a laser wakefield accelerator causes quasi-periodic "wiggler" motion, which results in synchrotron radiation. This is described in more detail in chapter 2.5. The electromagnetic radiation beam properties (such as photon energy, coherence, pulse duration etc.) are determined by the properties of the accelerated particle beam (e.g. energy, energy spread, charge pulse duration).

Most particle accelerators are based on radio frequency (RF) cavities or travelling wave structures. Particles are pushed by the electric field of microwaves resonating in evacuated cavities or wave-guide structures. The size of the cavity and frequency of the accelerating wave are tuned such that particles move from one cavity to the next as the sign of the wave changes from positive to negative so that they always experience an accelerating field. These accelerators are extremely reliable producing high energy charged particles (electrons, protons or ions) with high beam quality (low energy spread and low emittance). However, the maximum accelerating field that can exist inside them is limited by electrical breakdown of the cavity walls to about

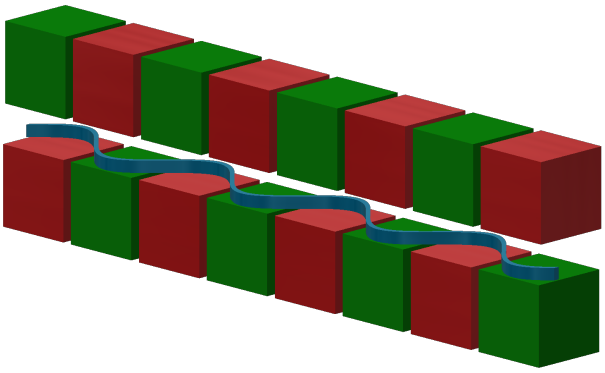

Figure 1.1: Sketch of undulator consisting of a series of permanent magnets with alternating field directions which gives rise to oscillations in the electron trajectory (shown in blue) as a beam of charged particles pass through it.

100 $\mathrm{MV\,m^{-1}}$, thus TeV accelerators such as the Large Hadron Collider (LHC) are kilometres in circumference. The electron gun is the first element in the accelerator chain and also compression stages in the accelerator line, which determine the bunch duration of the electron beam at the point of use. The shortest pulse durations are obtained using photo-injectors. The duration of the electron bunch is limited by the duration of the laser pulse so electron beams in RF cavity accelerators are usually limited to $30 - 100$ fs.

These bunch duration limitations can be overcome using a plasma-based accelerator since plasma is already fully broken down the maximum electric field only depends on the plasma density. The bunch duration is determined by the injection mechanism, which can be controlled by varying the plasma density to produce attosecond bunches [11, 12].

1.2 Properties of Plasma

Plasma is a partially or fully ionised quasi-neutral medium, where positively charged ions and unbound negatively charged electrons interact mainly via long-range electric and magnetic forces that lead to collective motion (leading to density waves). It is often referred to as the fourth state of matter after solids, liquids and gasses, and it

is estimated that more than 99% of the observable universe is in the plasma state of matter.

For collective effects in ionised gas or plasma to exist the length of the plasma must be larger than the Debye shielding length [7, 13]. On a microscopic scale, plasma electrons experience the Coulomb force that attracts them towards plasma ions so as to neutralise the plasma. The electric field due to an additional (test) charge in plasma, which makes the plasma non-neutral, only acts on other charged particles over a finite distance known as the Debye shielding length, beyond which the plasma acts as if it is neutrally charged. The distance from a test charge where the thermal energy ($k_B T_e$) is equal to the electrostatic potential energy defines the edge of the shielding cloud. The radius of this cloud is the Debye length and is given by

$$\lambda_D = \sqrt{\frac{\epsilon_0 k_B T_e}{e^2 n_e}}, \tag{1.1}$$

where ϵ_0 is the permittivity of free space, k_B the Boltzmann constant, T_e the electron temperature and e the electron charge. n_e is the plasma electron number density, usually expressed in electrons per cubic centimetre (cm^{-3}). For collective effects to dominate the behaviour of plasma, its volume should be much greater than a sphere with radius equal to the Debye length and there should be many particles within this Debye sphere, i.e. $n_e \lambda_D^3 \gg 1$.

The force due to the electric field between plasma electrons and ions results in a natural oscillation of electrons in the plasma at the plasma frequency, which depends on the electron number density. The plasma frequency is given by

$$\omega_p = \sqrt{\frac{n_e e^2}{\epsilon_0 m_e}}, \tag{1.2}$$

where m_e is the electron mass. If the electron velocity is high then the relativistic correction to the electron mass must be made and the plasma frequency becomes a function of both plasma electron number density and electron mass. The simple wave relationships can be applied to the plasma frequency to find its wavelength ($\lambda_p = 2\pi c/\omega_p$) and period ($T_p = 2\pi/\omega_p$), which are important length and time scales for

plasma based accelerators.

The dispersion relation for electromagnetic waves, such as a laser pulse, in an unmagnetised plasma is given by

$$\omega^2 = c^2k^2 + \omega_p^2, \tag{1.3}$$

which has a cut off frequency below which waves cannot propagate and are evanescent. The lowest frequency wave that can propagate in plasma has frequency $\omega = \omega_p$ so if the electromagnetic wave frequency is less than the plasma frequency ($\omega < \omega_p$), the plasma is considered as overdense and the laser pulse is reflected at the plasma-vacuum boundary and is evanescent in the plasma. If the electromagnetic wave frequency is greater than the plasma frequency ($\omega > \omega_p$) then the plasma is said to be underdense and the wave can travel through the plasma. All of the work presented in this thesis uses underdense plasma.

1.3 Laser driven plasma accelerators

The acceleration of charged particles using plasma density waves is a broad field. The acceleration mechanism, particle species being accelerated and particle beam properties depend upon the laser, plasma and beam parameters, all of which evolve in time. This section highlights a few different configurations of plasma accelerator.

1.3.1 The laser wakefield accelerator

The laser wakefield accelerators discussed in this thesis are driven by single, high peak intensity ($> 10^{18}$ W cm^{-2}), ultra-short (fs) duration lasers pulse that excites density waves trailing behind them at the laser group velocity in underdense plasma ($10^{18} - 10^{19}$ cm^{-3}). Electrons travelling around the perimeter of the plasma wave or evacuated bubble, form a sheath where some electrons can become trapped inside of it. This process is called self-injection: injected electrons surf the electric field of the plasma wave to reach high energies (MeV to GeV) in millimetres due to the ultrahigh electric field arising from the charge separation in the wake, which is described in more detail in chapter 2.

This concept was first proposed by Tajima and Dawson in 1979 [14], but it wasn't until the development of lasers based on chirped pulse amplification in 1985 by Strickland and Mourou [15] that these theoretical and computational ideas could be tested in the laboratory. In 1995 Modena et al., [16] demonstrated the production of a laser-driven plasma wave with an accelerating gradient of over 100 $\mathrm{GV\,m^{-1}}$, which is three orders of magnitude higher than in radio frequency (RF) cavity or travelling wave particle accelerators. Due to limitations in the peak laser power and laser pulse duration at the time, early plasma acceleration experiments were carried out in the self-modulated [17–23] regime or using the beat wave scheme [24–27]. These experiments used either external injection or self trapping injection to reach energies of up to 100 MeV, but with an exponentially decaying energy spectrum [16, 19, 28–30]. However, in 2004 a series of papers known as the "Dream-Beam" papers, presented the first demonstration of acceleration of quasi-monoenergetic electrons [31–33]. The paper by Mangles et al. [31] was part of the Strathclyde-led ALPHA-X project. This experimental progress in demonstrating stable acceleration confirmed simulations carried out in 2002 by Pukhov and Meyer-ter-Vehn [34], which predicted the "bubble" regime. In this case, plasma electrons are fully evacuated from the region behind the laser, creating a string of accelerating cavities where electrons can be trapped and accelerated. Figure 1.2 shows a computer simulation of a laser wakefield accelerator in the bubble regime make using the particle in cell technique. The green to blue colours represent the electron number density of the plasma where the bubble like shape of the plasma wave can be seen. The dark blue indicates regions of high plasma density. The pale blue to pink colour scale shows the positions and energy of electrons that have become trapped inside the plasma wave which are experiencing the strong accelerating field of the wave. Laser parameters were chosen to match those available in the Strathclyde laboratories. To date, the highest energy electron beam recorded is 7.8 GeV in a 20 cm capillary discharge waveguide using 850 TW laser pulses [35]. Since then, the aim of research in the field has diversified into reaching higher electron energies [36, 37], controlling injection to improve the quality of electron beams via density downramp injection [11, 38–43] or ionisation injection [44–49] and conducing proof of principle experiments for applica-

tions of plasma accelerators [50–60].

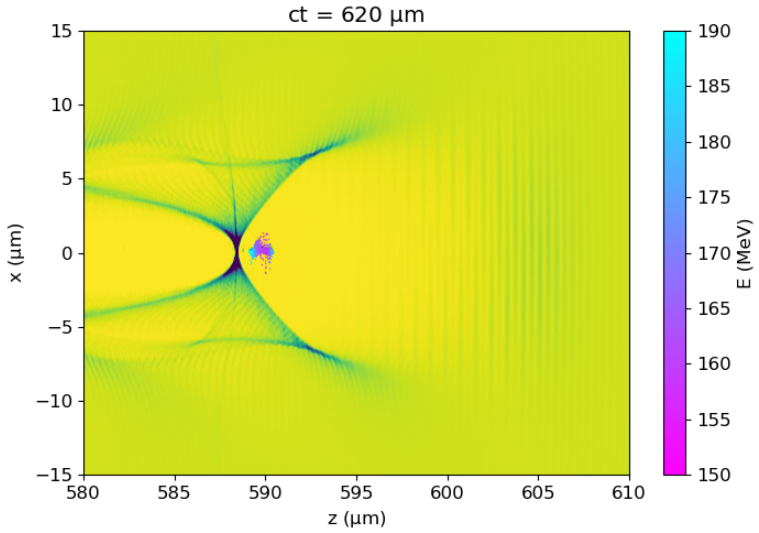

Figure 1.2: Simulation showing laser wakefield acceleration in the bubble regime. A fully evacuated density wave behind the laser can be seen with self-injected electrons with energies greater than 150 MeV shown. Simulation was performed using fbpic PIC code, for a laser pulse with wavelength 800 nm, energy 1.40 J, pulse duration 35 fs, focus radius 7 µm and plasma density 7×10^{18} cm^{-3}.

The laser wakefield accelerator can also be made to act as a source of electromagnetic radiation using a number of different mechanisms. Synchrotron radiation is naturally emitted through betatron oscillations of the electrons inside the bubble [61–63] or by steering them into an external undulator [58, 64, 65]. High-energy electrons incident on a solid target create bremsstrahlung radiation in the hard x-ray region [66–69]. Ultrashort electron bunches passing through a metal foil emit coherent transition radiation in the terahertz region [70–72]. Thomson and Compton backscattering have also been proposed as methods of producing gamma rays with laser driven accelerators [73], and the earliest experiments using an all optical set up produced photons with energies up to a few keV [74, 75]. Improvements in the electron beam quality have led to photons up to 9 MeV, and with narrow energy spreads and high brightness [76–79].

The main configurations of laser wakefield accelerators employ a gas jet, gas cell or capillary discharge waveguide.

Gas jet

Gas jets are nozzles which release a supersonic jet of gas that is timed to coincide with the incoming high power laser pulse, an example of which is shown in figure 1.3. Typically the outlet for the gas is a few millimetres in diameter (1 to 5 mm) and operate with gas backing pressures in the order of tens of bar using a pure gas of low atomic number which is easily ionised by the laser. For a given nozzle geometry, changing the gas pressure and the height of the laser above the top of the nozzle allows the electron density of the plasma can be controlled. Gas jets often are designed to give a flat density profile for several millimetres of laser propagation but colliding gas jets [42] and the insertion of razor blades [38–40, 43] into the gas can be used to shape the longitudinal profile of the plasma density and control electron injection into the plasma wake and thus electron acceleration. Controlling electron injection and acceleration with gas jets has also been achieved using a gas mixture, where the plasma created by a low atomic number (Z) gas is used to excite a plasma wave for acceleration and a high Z gas is ionised by the centre of the laser beam trapping electrons inside the wave, this method is known as ionisation injection [44–49]. Tilting of the gas jet towards or away from the laser can be used to control the length and gradient of the plasma density profile, from vacuum to the peak plasma density, to tune the electron energy by using the density gradient to delay dephasing [80]. All of the experiments presented in this thesis have been conducted using the 511 nozzle designed by Dr Constantin Aniculaesei [80] in his PhD thesis which has a 2 mm diameter outlet where the nozzle was kept at 90° to the laser beam axis with pure helium gas to create the plasma.

Capillary discharge waveguide

Capillary discharge waveguides [81, 82] have been used to extend the length of the laser plasma interaction up to 20 cm [35]. In a capillary discharge waveguide, gas is injected into a few hundred micron diameter channel machined into a material such as Alumina where it is preionised by a high voltage discharge [83]. Cooling against the walls of the capillary produces a parabolic plasma density profile, which acts to guide the laser [84–86]. This enables acceleration over many Rayleigh lengths of the

Figure 1.3: Photograph of brass gas jet with 1 mm diameter gas outlet.

laser beam allowing record energies to be reached. Capillary discharge waveguides use an order or magnitude lower plasma density and therefore have a longer dephasing length. The capillary discharge waveguides previously investigated at the University of Strathclyde were machined in-house (see Figure 1.4) with a low power titanium sapphire laser with 1 kHz repetition rate [51, 87] ablating the surface of the capillary material with an average power of 500 µW.

An alternative to gas jets and capillaries is the gas cell. This traps gas inside a chamber, which is ionised by the laser similar to a gas jet. The geometry of the inside of the gas cell can be shaped to give a longitudinal profile to trigger and trigger and control electron injection into the plasma wave. Gas cells have been used up to a few centimetres, producing electrons up to a few GeV [36].

1.3.2 Other plasma based accelerators

Multiple pulse

Low intensity laser beams are not capable of exciting non-linear plasma waves sufficient for electron injection into the wake. However, a series of laser pulses spaced

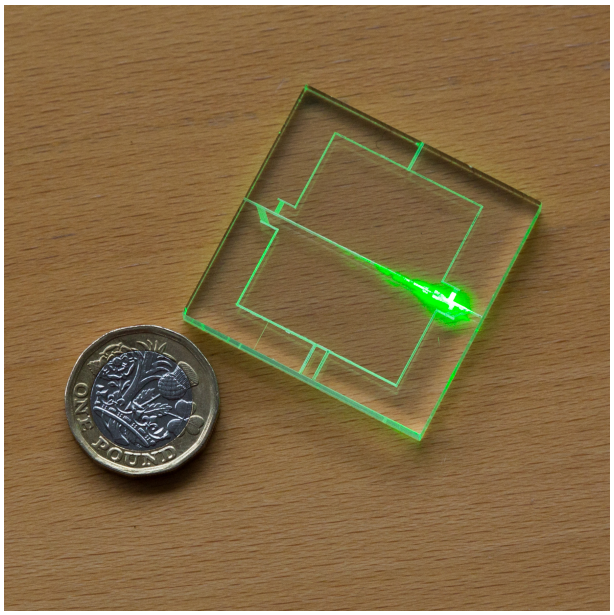

Figure 1.4: Photograph of 40 mm Capillary discharge waveguide illuminated with a laser pointer to show the capillary waveguide and gas inlets.

by the plasma period can resonantly excite an electron density wave [88–90]. In this configuration of the plasma accelerator, the wakefields driven by each of the pulses coherently add up, resulting in a plasma wave amplitude that grows towards the back of the pulse train. Multiple pulse laser wakefield acceleration requires lasers with only tens to hundreds of millijoules of energy per pulse but at repetition rates in the tens of kilohertz. Beamsplitters and delay lines are used to create the pulse train at the correct frequency [91]. Recent progress has been made demonstrating the growth of the plasma wave amplitude with a laser repetition rate lower than the plasma period. However, electron injection and acceleration has not yet been achieved [92]; current laser technology has been cited as the limiting factor of this scheme.

Self-modulated

Similar to multiple pulse laser wakefield acceleration, self modulated acceleration also employs the use of a train of laser pulses but these are created in the plasma itself from a single long (picosecond) pulse [17–23]. Modulations in the laser profile along the

propagation axis are caused by producing regions of self-focusing and diffraction, due to Raman forward scattering, which are equally spaced resulting in a pulse train with separation between pulses equal to the plasma period. To be in the self modulated regime, the laser pulse incident on the plasma must be of sufficient power for self-focusing to occur (see chapter 2.4.3) and the pulse length ($L = c\tau_p$) must be longer than the plasma wavelength ($\lambda_p = \frac{2\pi c}{\omega_p}$). This is a much simpler way of creating a pulse train compared with multiple pulse laser wakefield acceleration. However, this scheme has near constant electron injection into the wake resulting in electron beams with very large energy spreads [16, 19, 21, 93–95].

Beatwave

The plasma beatwave accelerator is a concept first introduced by Tajima and Dawson in there original paper describing the acceleration of charge particles in plasma waves [14]. This configuration of plasma accelerator uses two co-propagating laser pulses instead of a single high peak power pulse to excite a strong wakefield in a plasma [24, 25, 96], where the two laser pulses have frequencies that differ by the plasma frequency, ($\Delta\omega = \omega_1 - \omega_2 = \omega_p$). When the pulses overlap, the interference pattern between them creates an electromagnetic beatwave that resonantly drives a plasma wave generated through the ponderomotive force, which generates a high amplitude plasma wave. The first experiments using in the plasma beatwave accelerator externally injected an electron bunch into the plasma wave and showed accelerating fields of several $\mathrm{GV\,m^{-1}}$ [26, 27, 97, 98].

Particle beam driven plasma accelerators

Intense laser pulses are not the only option for driving wakefields, it is also possible to excite wakes using a charged particle beam, which is known as plasma wakefield acceleration (PWFA) [99]. In this case, the Coulomb force of the "driver beam" pushes plasma electrons by repelling (in the case of an electron driver) or attracting (in the case of a proton driver) electrons, and sets up a plasma wave in a similar way to the ponderomotive force of a short laser pulse. Proof of principle experiments are under way at

a small number of dedicated facilities. Generation of a wakefield and a demonstration of the large accelerating field for a electron driver has been done at SLAC (Stanford linear accelerator) where they doubled the energy of a "witness" electron bunch initially at 42 GeV in 85 cm, giving an average accelerating gradient of 52 GV m^{-1} [100]. The Advanced Wakefield Experiment (AWAKE) project at CERN uses a high energy bunch of protons to drive a wakefield [101, 102]. Electron acceleration was first demonstrated in 2018 where an electron witness beam, with initial energy 18.84 MeV, was externally injected into the wakefield and accelerated up to 2 GeV. The wakefield was excited by a 400 GeV proton pulse from the Super Proton Synchrotron in a 10 m long Rubidium plasma with density $\sim 10^{14}$ cm^{-3} [103]. Another dedicated plasma wakefield acceleration experiment at DESY in Hamburg has been first to demonstrate the self-modulated instability for a particle beam driver that the DESY and AWAKE experiments rely upon for wakefield excitation [104].

Overdense plasma accelerators

If the plasma is overdense, the laser cannot propagate through it to generate a wake. However, the laser-plasma interaction in this case can accelerate protons [105, 106]. The simplest case is target normal sheath acceleration (TNSA) [107] where a high intensity laser pulse is incident on a thin (µm) metal target. In this case, the laser does not travel through the target but the laser field drives a high current of electrons through it creating a sheath on the rear surface resulting in a space-charge electric field that pulls protons out of the target, accelerating them to non-relativistic energies up to 100 MeV [108, 109]. Many variants on this concept exist, such as radiation pressure acceleration (hole boring [110], light sail [111]) acceleration and relativistic induced transparency acceleration [112–114] where the change of plasma frequency due to relativistic increase in electron mass makes the plasma transparent to the laser allowing it to propagate through the otherwise overdense plasma.

Chapter 2

Theory of laser wakefield acceleration

This chapter gives an overview of the theory of the laser wakefield accelerator and discusses factors that limit the final energy of accelerated particles. Finally, the production of radiation from plasma electrons is discussed.

2.1 Electron motion in an intense laser field

A laser pulse comprises oscillating electric ($\mathbf{E}$) and magnetic ($\mathbf{B}$) fields that travels through space. For laser wakefield acceleration a laser with a high peak intensity is required, which is the power per unit area and proportional to the square of the electric field. However, for calculations and simulations in laser plasma interactions, it is more convenient to express the $\mathbf{E}$ and $\mathbf{B}$ fields in terms of the potentials as they directly infer the transverse velocity of the electron in the field. The normalised vector potential a_0 is proportional to the vector potential $\mathbf{A}$ and ϕ is the scalar potential, where $\mathbf{E} = -\partial\mathbf{A}/\partial t - \nabla\phi$, $\mathbf{B} = \nabla \times \mathbf{A}$ [7]. The normalised potential can be written as

$$\mathbf{a} = \frac{e\mathbf{A}}{m_e c}, \tag{2.1}$$

where the amplitude of the normalised vector potential is given by

$$a_0 = \frac{eE_0}{\omega m_e c}. \tag{2.2}$$

The normalised vector potential can be expressed in terms of two experimental measurable quantities, the laser intensity and the central laser wavelength, as

$$a_0 = \sqrt{\frac{Ie^2\lambda^2}{2\pi^2\epsilon_0 m_e^2 c^5}} = \sqrt{\frac{I[\mathrm{Wcm^{-2}}]\lambda^2[\mu\mathrm{m}^2]}{1.368\times10^{18}}}. \tag{2.3}$$

The normalised vector potential gives the threshold where the relativistic correction to the particle mass becomes significant and its motion is influenced by both electric and magnetic fields. Laser plasma interactions are said to be in the relativistic regime when $a_0 > 1$.

The motion of particles in an electromagnetic field is governed by the Lorentz equation. For a single electron or proton, the Lorentz force exerted by low intensity laser fields is given by

$$\frac{d\mathbf{p}}{dt} = -e(\mathbf{E} + \mathbf{v}\times\mathbf{B}), \tag{2.4}$$

where $\mathbf{p}$, e and v are the particle momentum, charge and velocity respectively. $\mathbf{E}$ and $\mathbf{B}$ are the applied electric and magnetic fields from the laser pulse. If the field strength is low, then the velocity of a test particle in the field is small therefore the $\mathbf{v}\times\mathbf{B}$ component can be neglected and the motion of the particle is linear and can be solved by integrating the force equation in time. The electric field of a plane wave travelling along z and polarised in the x direction is given by

$$E_x = E_0\cos(\omega t), \tag{2.5}$$

where ω is the angular frequency of the wave with units $\mathrm{rad\,s^{-1}}$. Given that the momentum of a test electron in the field is $p = m_e v$, in the x direction, integration of the Lorentz equation gives the velocity and position the electron,

$$v = \frac{eE_0}{\omega m_e} \sin(\omega t), \tag{2.6}$$

and

$$s = \frac{-eE_0}{\omega^2 m_e} \cos(\omega t). \tag{2.7}$$

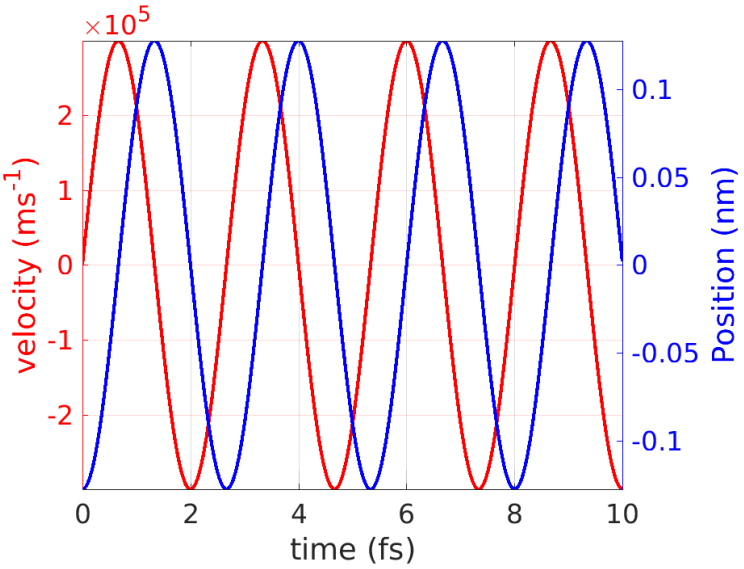

Figure 2.1: Motion of single electron in low intensity electromagnetic wave with $a_0 = 0.001$ and wavelength 800 nm.

Figure 2.1 shows the electron motion and velocity in a low intensity laser field by solving equations 2.7 and 2.6 where the motion of the electron is purely in the direction of the laser polarisation. From equation 2.6, it can be seen that the largest velocity the electron reaches is given by $v_{\max} = \frac{eE_0}{\omega m_e}$, when $\sin(\omega t) = 1$. If this maximum velocity is normalised against the speed of light then the normalised vector potential is returned, $a_0 = v_{\max}/c = \frac{eE_0}{\omega m_e c}$.

As the field strength becomes large, the electron velocity and therefore its momentum also becomes large. When the normalised momentum of the electron approaches unity, $mv/mc \approx 1$, the motion is said to be relativistic and the contribution from the magnetic field of the laser can no longer be neglected. The full Lorentz equation must therefore be solved to calculate the trajectory of the particles which includes the magnetic, $\mathbf{B}$ field, and a relativistic correction to the electron momentum, $\mathbf{p} = \gamma m_e \mathbf{v}$ where

$\gamma = \sqrt{1 + (v^2/c^2)}$ is the electron Lorentz factor. The relativistic Lorentz force can be written as

$$\mathbf{F} = \frac{d\gamma \mathbf{v}}{dt} = \frac{-e}{m_e}(\mathbf{E} + \mathbf{v} \times \mathbf{B}). \tag{2.8}$$

The magnetic field pushes on a test electron in the direction of laser propagation, which is perpendicular to both the electric and magnetic fields of the laser. The equations of motion were solved by Meyer-ter-Vehn, Pukhov and Sheng [115], where the magnitudes of the fields are assumed to be large, and assuming $a_x = a_0 \cos(\omega\tau)$

$$x(\tau) = \frac{ca_0}{\omega} \sin(\omega\tau), \tag{2.9}$$

and

$$z(\tau) = \frac{ca_0^2}{4}(\tau + \frac{1}{2\omega} \sin(2\omega\tau)), \tag{2.10}$$

where the transform $\tau = t - z(t)/c$ gives the phase of the wave and is also the proper time of the electron. Figure 2.2 shows that for low laser intensities, the electron moves mainly in the direction of the electric field. As a_0 increases, the motion in the direction of the laser propagation becomes significant and is the dominant motion when $a_0 > 1$.

The electron motion in the z direction along the laser propagation axis has two components, a constant electron drift motion given by $z(\tau) = \frac{ca_0^2}{4}\tau$, with average velocity $v_{\text{drift}} = ca_0^2/(4 + a_0^2)$, plus an oscillatory motion. When the motion is calculated in the reference frame of the drift motion, the shape of the oscillatory motion can be seen to be a figure of eight trajectory around the test particle's initial position. The figure of eight motion is shown in figure 2.3 where the motion in the x and z directions are normalised against the laser wavevector $k = 2\pi/\lambda$.

2.2 The ponderomotive force

The ponderomotive force is the radiation pressure of the laser pulse that is responsible for the transfer of momentum between the laser field and plasma particles. In the

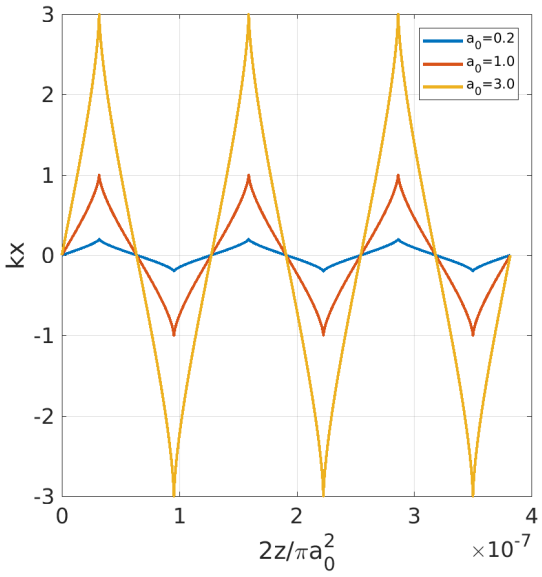

Figure 2.2: Solutions to equations 2.9 and 2.10 to show motion of single electron in electromagnetic wave with wavelength 800 nm and vector potentials, $a_0 = 0.2$ (blue), 1.0 (red) and 3.0 (yellow).

classical case ($\gamma \approx 1$) the ponderomotive force can be expressed in the form [116, 117]

$$\mathbf{F}_p = -\frac{e^2}{2m_e\omega^2}\nabla\mathbf{E}^2 = -m_e c^2 \nabla\left(\frac{\mathbf{a}^2}{2}\right), \tag{2.11}$$

for an electric field of the form in $\mathbf{E}(\mathbf{r}, t) = \mathbf{E}(\mathbf{r})\cos(\omega t)$ and neglecting the effect of the $\mathbf{v} \times \mathbf{B}$ component of the Lorentz force. The magnitude of the ponderomotive force is proportional to the square of the time-averaged electric field so acts to push plasma particles away from regions of high laser intensity. For a laser envelope with a Gaussian profile, plasma particles are pushed away from the laser axis. In a given laser field, the magnitude of the ponderomotive force is much larger for plasma electrons compared to more massive protons and ions, however the direction of the ponderomotive force is the same for positively and negatively charged particles. The magnitude $\mathbf{F}_p$ scales with λ^2, so the force is larger for longer wavelength laser drivers. In the relativistic case, the electron quiver motion described in section 2.1 needs to include the effect of increase in

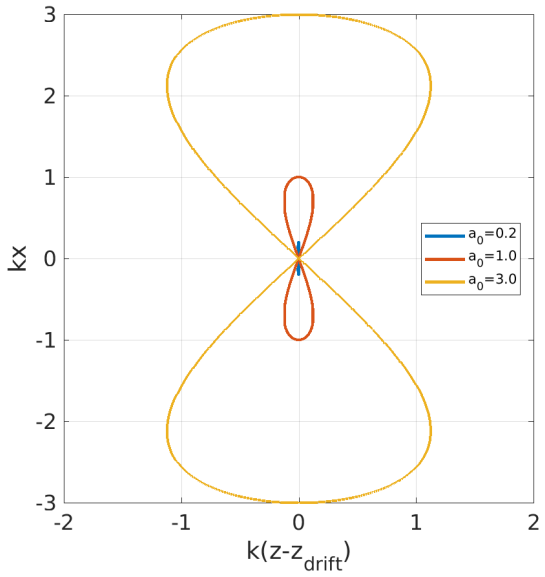

Figure 2.3: Motion of single electron in electromagnetic wave with laser vector potentials $a_0 = 0.2$ (blue), 1.0 (red) and 3.0 (yellow) and wavelength 800 nm moving in the reference frame at the electron drift velocity, v_{drift}. Plot was obtained by solving 2.9 and 2.10 with the drift motion in the z direction subtracted.

electron mass. The relativistic treatment of the ponderomotive force gives [118, 119]

$$F_p = -\frac{e^2}{2\bar{\gamma} m_e} \nabla A^2 = \frac{m_e c^2}{2\bar{\gamma}} \nabla a_0^2. \tag{2.12}$$

2.3 Laser wakefield acceleration

The concept behind the laser wakefield accelerator (LWFA) has been introduced in chapter 1. The plasma density wake created by the ponderomotive force of a high power laser pulse in underdense plasma can lead to charge separation that produces extremely high fields suitable for accelerating charged particles such as electrons or positrons. The wake structure depends primarily on the plasma density (n_e) and the laser intensity. At low laser intensities, ($a_0 \ll 1$), the wave produced is sinusoidal and only perturbs the electron density by a few percent resulting in a modest electric field. Because self injection is unlikely, a separate electron bunch from a linac can be used as an injector, but the it is usually very challenging to obtain a sufficiently short

injection bunch to ensure a low energy spread as well as requiring precision timing between the electron and laser beams. At high laser intensities ($a_0 > 1$) the plasma wave becomes highly nonlinear, and the peak density at the back of the wave can be being several times the background density. The magnitude of the accelerating field is also much larger than for the linear case. Furthermore, the trajectories of electrons in the sheath begin to cross in the non-linear regime, leading to wavebreaking and the self-injection of electrons into the back of the wave. Unlike the linear case, however, modelling nonlinear plasma waves require numerical simulations.

2.3.1 The linear regime

As a laser pulse propagates through a plasma, the ponderomotive force acts to push particles away from regions of high laser intensity. Since the ion mass is much greater than the electron mass and the frequency the laser pulse is high, ions are only slightly perturbed from their initial position and can be considered as stationary. Electrons, however, are significantly perturbed by the laser pulse, which results in charge separation and a large Coulomb force that acts as a restoring force. Since the electrons acquire a finite velocity, they oscillate around the plasma ions. Using a plasma fluid model and assuming a cold plasma (no thermal motion of plasma particles and perfect Debye shielding such that there is no electric field outside of the shielding cloud), and no laser evolution with time, the wakefield from the laser can be derived using the Poisson equation, the continuity equation and the fluid momentum equation. The density wave behind the laser is given by [117]

$$\left(\frac{\partial^2}{\partial t^2} + \omega_p^2\right)\frac{\delta n}{n_0} = \frac{c^2\nabla^2 a^2}{2}, \tag{2.13}$$

and the corresponding potential in the plasma due to charge separation is

$$\left(\frac{\partial^2}{\partial t^2} + \omega_p^2\right)\phi = \frac{\omega_p^2 a^2}{2}, \tag{2.14}$$

where n_0 is the background plasma density, $\delta n/n_0 = (n - n_0)/n_0$ is the normalised amplitude of the density wave, $\phi = \frac{e\Phi}{m_e c^2}$ is the normalised scalar potential, and $\nabla^2 a^2$ is

the rate of change of the intensity of the laser pulse envelope. These equations can be solved analytically for a given laser intensity distribution in three spatial dimensions. For example, a Gaussian laser pulse of the form

$$a(z,t) = a_0 \exp\left[-\left(\frac{k_0 z - \omega_0 t}{\sqrt{2}k_p L}\right)^2\right], \tag{2.15}$$

has been shown [120, 121] to excite a wakefield with accelerating (longitudinal) electric field of the form

$$\mathbf{E}(z,t) = E_{\mathrm{wb}} \frac{\sqrt{\pi} a_0^2}{4} k_p L \exp\left(\frac{-k_p^2 L^2}{4}\right) \cos\left(k_0 z - \omega_0 t\right) \mathbf{e}_z, \tag{2.16}$$

where k_0 and ω_0 are the laser wavevector and angular frequency, respectively, k_p is the plasma wavevector and $L = c\tau$ is the laser pulse length. E_{wb} is the maximum accelerating electric field in the linear regime, referred to as the cold non-relativistic wavebreaking field [122], which can be simply obtained from Gauss's law, assuming a 100% density perturbation

$$\nabla \cdot \mathbf{D} = \rho, \tag{2.17}$$

using $\mathbf{D} = \epsilon_0 \mathbf{E}$ and that the charge density is the product of the electron charge and the number density $\rho = e n_e$,

$$\nabla \cdot \mathbf{E} = \frac{\rho}{\epsilon_0} = \frac{e n_e}{\epsilon_0}. \tag{2.18}$$

Using the transform $\nabla \rightarrow ik$ and rewriting the wavevector as a angular frequency, $\omega = ck$, gives

$$\left(\frac{\omega}{c}\right) \mathbf{E} = \frac{e n_e}{\epsilon_0} \tag{2.19}$$

The peak electric field amplitude is obtained assuming a uniform plasma and a plasma wave phase velocity approaching c so $k = k_p = \omega_p / c$. The plasma density on the right hand side can then be written in terms of its frequency $n_e = \omega_p^2 \epsilon_0 m_e / e^2$,

$$E_{\mathrm{wb}} = \frac{m_e c \omega_p}{e}. \tag{2.20}$$

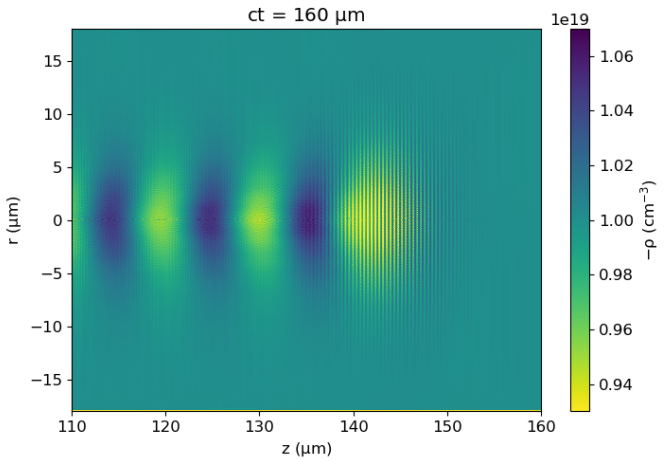

Figure 2.4: Simulation of electron number density performed for linear wakefield using fbpic with $a_0 = 0.5$, $\lambda_0 = 800$ nm, $w_0 = 10$ µm, $n_e = 1.0 \times 10^{19}$ cm^{-3}, $\tau_{\mathrm{FWHM}} = 30$ fs, longitudinal resolution 20 nm, radial resolution 39.1 nm. The simulation box is 20 µm in the radial direction and 50 µm in the longitudinal direction.

A simulation of a wakefield is shown in figure 2.4, which was obtained using the fully relativistic particle-in-cell (PIC) code fbpic [123] for a Gaussian laser pulse with peak normalised vector potential of $a_0 = 0.5$. Line out plots (figure 2.5) from the simulation show the regular sinusoidal variation in both the density perturbation and the magnitude of the longitudinal electric field (E_z), and also the $\pi/2$ phase lag between them. In the linear regime, the size of the perturbation is small, on the order of a few percent (7% for the example parameters from figure 2.5). Even for the low intensity lasers required to remain in the linear regime, the peak accelerating field (10 GV m^{-1} using parameters from figure 2.5) is much larger than the highest possible accelerating fields in RF accelerators ($\sim$ 100 MV m^{-1}), which are limited by electrical breakdown of the cavity walls.

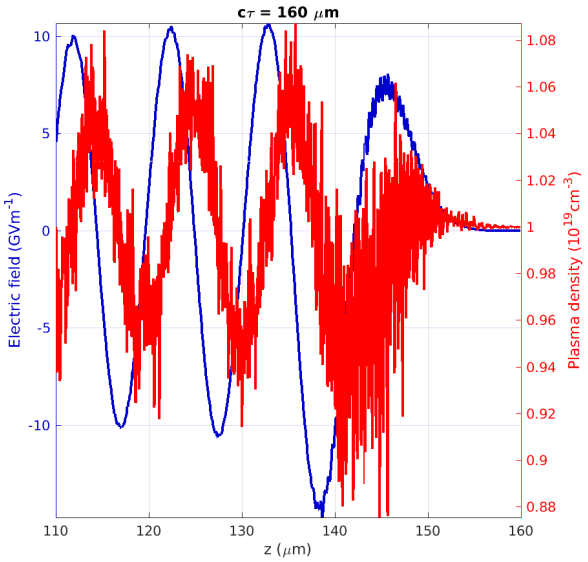

Figure 2.5: Lineout plots along $r = 0$ of plasma density wave and longitudional electric field from simulation in figure 2.4

2.3.2 The nonlinear regime

When the electric field amplitude of the laser becomes larger than the wavebreaking field and a_0 is larger than one, the plasma wave becomes nonlinear as a result of the plasma electrons exhibiting relativistic effects when they are experiencing the ponderomotive force of the laser pulse driving the wave. For a Ti:Sapphire laser with central wavelength of 800 nm, commonly used in laser wakefield experiments, the intensity threshold for the nonlinear regime, from equation 2.3, is 2.14×10^{18} W cm^{-2} (equivalent to a 940 mJ laser with pulse duration 35 fs, focused to a waist radius of 20 µm), which is easily achievable with current laser technology. The plasma density wave is no longer sinusoidal and the wavefronts of the wave become curved, as shown in figure 2.6, which is the same simulation as figure 2.4 but with a normalised laser vector potential increased from $a_0 = 0.5$ to 2.0.

In the nonlinear regime, electron streams overlap at the back of the wave and creating regions with a very high density. The gradient of electron density is large in the nonlinear regime resulting in a saw-tooth field pattern in the longitudinal (z)

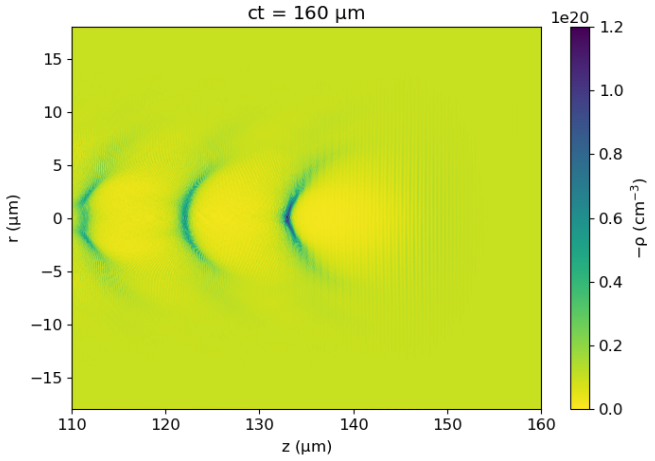

Figure 2.6: Simulation of electron number density of a nonlinear wakefield using fbpic, with $a_0 = 2$, $\lambda_0 = 800$ nm, $\omega_0 = 10$ µm, $n_e = 1.0 \times 10^{19}$ cm^{-3}, $\tau_{\mathrm{FWHM}} = 30$ fs, longitudinal resolution 20 nm, radial resolution 39.1 nm. The simulation box is 20 µm in the radial direction and 50 µm in the longitudinal direction.

direction. These nonlinear fields are ideal for accelerating charged particles.

In 2002 Pukhov and Meyer-ter-Vehn [34] predicted, through simulation, a regime for laser wakefield acceleration where electron beams with narrow energy spreads can be accelerated using laser pulses with duration shorter than a plasma period and $a_0^2 \gg 1$. In this case, electrons are fully evacuated [34, 124–126] from the region behind the laser pulse creating a string of accelerating "bubbles", where particles can be trapped and accelerated [31–33], which is referred to as the bubble (or blow-out) regime. In this case, the bubble is most efficiently generated when the plasma is "matched" to the laser pulse, i.e., when it satisfies the condition

$$k_p r_{\mathrm{B}} \simeq k_p w_0 = 2\sqrt{a_0}, \tag{2.21}$$

where $k_p = \omega_p/c$ is the plasma wavevector, r_{B} is the radius of the plasma bubble, w_0 is the laser spot size and a_0 is the laser normalized vector potential. With the matching condition satisfied, the bubble radius is simply

$$r_B \approx \frac{2\sqrt{a_0}}{k_p}. \tag{2.22}$$

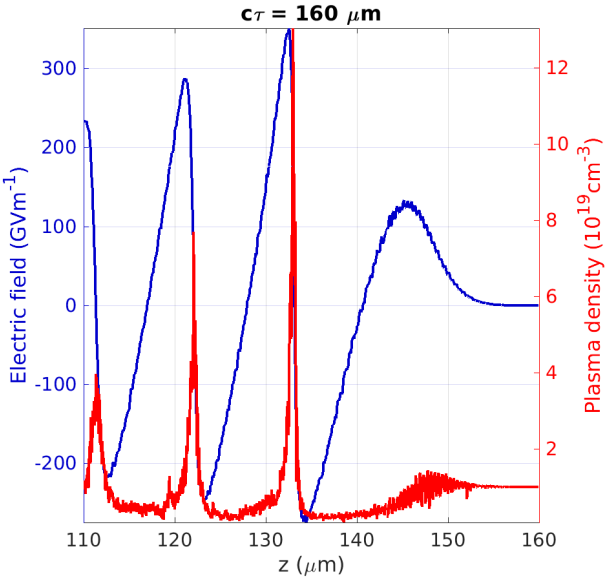

Figure 2.7: Lineout plots along $r = 0$ of the plasma density wave or wake and the corresponding longitudinal electric field, from the simulation in figure 2.6

An example of this is shown in figure 2.8 where the circular blow out shape is marked. The simulation performed using fbpic is for a 350 TW laser pulse ($E = 8.75$ J, $\tau_{\mathrm{FWHM}} = 25$ fs) matched to a plasma density of $n_e = 1.3 \times 10^{19}$ cm^{-3}.

In the bubble regime, it is possible for some electrons crossing at the back of the bubble to have a longitudinal velocity exceeding that of the bubble. If this condition is met then these electrons inject into the plasma bubble, where they can be accelerated by the fields inside the bubble in a process referred to as self-injection. Further work using particle in cell simulations by Gordienko et al., [127] in 2005 and Lu et al., in 2007 [128] gave scaling laws for laser wakefield acceleration in the bubble regime including estimates of the maximum number of electrons that can be injected into the wake and the final energy of these accelerated electrons for self-injection. Both sets of scaling laws assume $a_0 > 1$, a pulse length approximately equal to the plasma wavelength ($c\tau \sim \lambda_p$) and a laser power greater than the critical power for self focusing.

In the simulations performed by Lu et al. [128], it is assumed that the accelerating fields are linear, with an average value of $E_{\mathrm{wb}}/2$ and that $2 < a_0 < 4$, which gives a

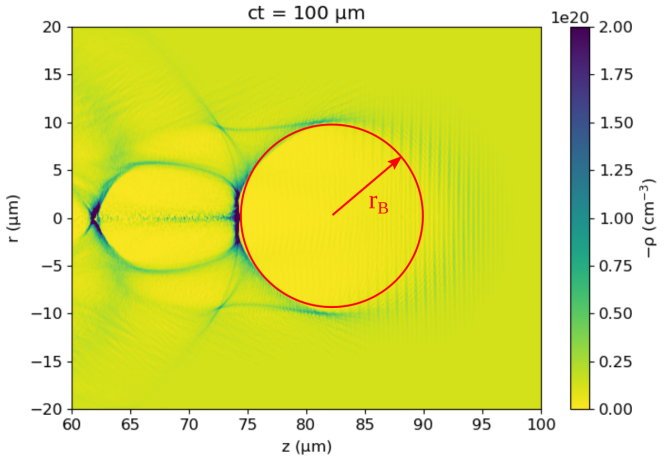

Figure 2.8: Simulation of electron number density wave in the bubble regime with the bubble radius marked. Parameters chosen for 350 TW laser pulse with waist matched to the plasma density. $a_0 = 8.428$, $\lambda_0 = 800$ nm, $w_0 = 8.56$ µm, $n_e = 1.3 \times 10^{19}$ cm^{-3}, $\tau_{\mathrm{FWHM}} = 25$ fs.

total of

$$N_{\mathrm{Lu}} \simeq \frac{8}{15}\frac{1}{k_0 r_e}\sqrt{\frac{P}{m_e^2 c^5/e^2}}, \tag{2.23}$$

electrons becoming trapped inside the wake. Here, k_0 is the laser wave vector and $r_e = e^2/(4\pi\epsilon_0 m_e c^2) \approx 2.82$ fm is the classical electron radius and P is the laser power. This relationship can be expressed in terms of the experimental observables, by multiplying out the constants to give

$$N_{\mathrm{Lu}} \simeq 2.5 \times 10^9 \frac{\lambda[\mu\mathrm{m}]}{0.8}\sqrt{\frac{P[\mathrm{TW}]}{100}}. \tag{2.24}$$

According to Gordienko [127], who took into account beam loading (that is the effect of the electrons trapped in the wake), and assuming $a_0 \gg 1$, a similar scaling equation is obtained

$$N_{\mathrm{Gordienko}} \simeq \frac{1.8}{k_0 r_e}\sqrt{\frac{P}{m_e^2 c^5/e^2}}. \tag{2.25}$$

The maximum energy that these injected electrons can reach was investigated by both authors. The highest energy that electrons can reach in the bubble regime occurs

when the length of the plasma is equal to both the pump depletion length and the dephasing length. The simulations performed by Lu et al. [128] give

$$\Delta E_{\mathrm{Lu}} \simeq m_e c^2 \left(\frac{P}{m_e^2 c^5/e^2}\right)^{1/3} \left(\frac{n_c}{n_e}\right)^{2/3}, \tag{2.26}$$

which has a stronger dependence on plasma parameters than laser ones. In practical units, equation 2.26 is expressed as

$$\Delta E_{\mathrm{Lu}}[\mathrm{GeV}] \simeq 1.7 \left(\frac{P\,[\mathrm{TW}]}{100}\right)^{1/3} \left(\frac{10^{18}}{n_e\left[\mathrm{cm}^{-3}\right]}\right)^{2/3} \left(\frac{0.8}{\lambda\,[\mu\mathrm{m}]}\right)^{4/3}. \tag{2.27}$$

For higher laser intensities assumed by Gordienko [127], the peak electron energy scales as

$$\Delta E_{\mathrm{Gordienko}} \simeq 0.65 m_e c^2 \sqrt{\frac{P}{\frac{m_e^2 c^5}{e^2}}} \frac{c\tau}{\lambda}, \tag{2.28}$$

assuming the laser pulse length ($c\tau$) is less than the bubble radius r_{B}. The scaling obtained by Gordienko [127] demonstrates the dependence of the final energy of the electrons on laser parameters for high laser intensities. The scaling laws (figure 2.9) show that GeV energies are achievable in a single acceleration stage. However, lasers with high peak powers of hundreds of terawatts to petawatts are required to reach the critical power for self-focusing required for guiding the laser for a sufficient distance to reach these energies. To reach higher energies still, external laser guiding using capillaries (introduced in chapter 1.3.1) or staging of multiple laser wakefield accelerators is required [129–134].

2.4 Final energy limitations

2.4.1 Pump depletion

The energy exciting the plasma wake results in a continuous loss of laser energy as it travels through the plasma, which results in "pump depletion". If the electrons in the wake travel beyond the "depletion length", they begin to lose energy. The depletion length is the distance a laser pulse travels in a plasma until it no longer has sufficient

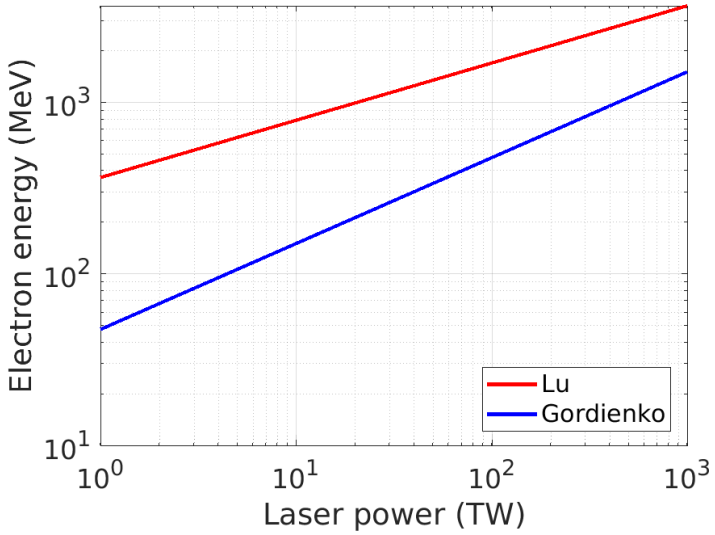

Figure 2.9: Maximum electron energy in bubble regime according to scaling laws from Lu [128] (equation 2.26) and Gordienko [127] (equation 2.28). Calculations were performed for a laser wavelength of 800 nm, pulse duration 35 fs and plasma density 1×10^{18} cm^{-3}.

energy to drive the plasma wave. It can be found by equating the energy in the laser pulse with the energy left behind in the plasma wake to give [117, 135, 136]

$$L_{pd} = \frac{\lambda_p^3}{\lambda^2}\left(\frac{2}{a_0^2}\right) \quad a_0^2 \ll 1, \tag{2.29}$$

or

$$L_{pd} = \frac{\lambda_p^3}{\lambda^2}\left(\frac{\sqrt{2}a_0}{\pi}\right) \quad a_0^2 \gg 1. \tag{2.30}$$

For typical experimental parameters, the depletion length is of the order of a few millimetres. Overcoming pump-depletion to reach ultra-high electron energies can be achieved by concatenating many stages, each having their own laser driver [129–134].

2.4.2 Dephasing

The plasma wave travels behind the laser pulse at approximately its group $v_g = c\sqrt{1-\left(\omega_p^2/\omega_0^2\right)}$. However, injected electrons quickly reach a velocity close to that of the speed of light in vacuum. Electrons therefore advance towards the front of the

wake. When they reach approximately the half way point in the bubble, the electric field reverses and begins to decelerate the electrons causing them to lose energy. The dephasing length is therefore the distance travelled by the plasma wake before injected electrons reach this half way point, which occurs at [117, 135]

$$L_d = \frac{\lambda_p^3}{2\lambda^2} \quad a_0^2 \ll 1, \tag{2.31}$$

or

$$L_d = \frac{\lambda_p^3}{2\lambda^2}\left(\frac{\sqrt{2}a_0}{\pi N_p}\right) \quad a_0^2 \gg 1, \tag{2.32}$$

where N_p is the number of plasma periods that the trapped electrons are behind the laser pulse.

The effect of dephasing can be reduced by controlling the plasma density profile. This can be achieved in capillary discharge waveguides by reducing the radius of the capillary as a function of longitudinal position in the plasma to give a positive plasma density a gradient from entrance to exit [86, 137, 138]. As the wake propagates through the plasma, the plasma wavelength decreases and the bubble contracts in size during the acceleration ($r_{\mathrm{B}} \propto 1/\sqrt{n_e}$) which continuously advances the point at which the electrons begin to dephase. Trapped electrons remain in the accelerating region of the wake for a larger distance compared to a uniform plasma density which can extend the useful length of plasma accelerators and also allow higher electron energies to be reached.

2.4.3 Laser diffraction and self-focusing

A focused laser pulse will diffract beyond the focus position and therefore will only have sufficient intensity to drive a plasma wave over a short range given by the Rayleigh length. The laser spot size increases by a factor of $\sqrt{2}$ after one Rayleigh length, therefore the peak intensity falls by a factor of 2 and a_0 by a factor of $\sqrt{2}$. To excite a plasma wake the Ti:sapphire laser beam must be focused to a small spot with a correspondingly small Rayleigh length, which would usually set an upper length for the plasma accelerator, less than 2 mm. However, sufficiently high intensity laser beams

will self-focus in plasma because of relativistic effects. For a Gaussian transverse profile beam with $a_0^2 \gg 1$ plasma electrons close to the laser axis will experience a different refractive index than those further way from the axis. The relativistic correction to the electron mass, $m_e = \gamma_\perp(r) m_{e0}$, will result in a radially dependent plasma frequency $\omega_{p\ rel} = \sqrt{n_e e^2/(\epsilon_0 \gamma_\perp(r) m_{e0})}$, where $\gamma_\perp(r) = \sqrt{1 + a(r)^2}$. The refractive index of a plasma is given by

$$\eta = \sqrt{1 - \frac{\omega_p^2}{\omega_0^2}}, \tag{2.33}$$

therefore, in the case where the plasma frequency has a radial dependence this becomes

$$\eta(r) = \sqrt{1 - \frac{n_e e^2}{\omega_0^2 \epsilon_0 \gamma_\perp(r) m_{e0}}}. \tag{2.34}$$

The phase velocity of the laser pulse, $v_{\mathrm{ph}}(r) = c/\eta(r)$, is largest where the refractive index is small, which occurs in regions where the relativistic effects are small. The result of this is that light at the edges of the Gaussian pulse travel with a greater velocity than the more intense centre. The result of this is that the intensity profile of the pulse in a plasma acts as a positive lens that focuses the laser beam. The threshold laser power for relativistic self-focusing is given by [139]

$$\begin{aligned} P_c &= 2\frac{m_e c^5}{e^2}\left(\frac{\omega_0}{\omega_p}\right)^2, \\ P_c\ [\mathrm{GW}] &\simeq 17.4\left(\frac{\omega_0}{\omega_p}\right)^2 \mathrm{GW}. \end{aligned} \tag{2.35}$$

If the effect due to relativistic self-focusing is equal and opposite to the diffraction of the laser then it can propagate through the plasma with a constant spot size. In this case the laser is said to be "matched" to the plasma, which occurs when $a_0 \geq 2$ [128].

Guiding laser pulses over longer distances still can also be realised using a performed transverse density profile, such as by a capillary discharge waveguide, which prevents diffraction. In this case, gas-filled capillary is ionised to form plasma using an electrical discharge prior to the arrival of the laser pulse. The hot plasma cools against the walls of the capillary producing a linear temperature gradient (in thermal equilibrium)

that results in a parabolic density profile peaking close to the walls of the capillary [81, 85, 86, 139]. The refractive index, equation 2.33, becomes a function of radius, and for an electron number density given by

$$n_e(r) = n_e + \Delta n_e \left(\frac{r}{r_{\mathrm{ch}}}\right)^2, \tag{2.36}$$

where r is the position from the laser axis, r_{ch} the channel radius of the capillary and Δn_e the difference in plasma density between $r = 0$ and $r = r_{\mathrm{ch}}$, then the refractive index of the plasma can be written as

$$\eta(r) = \sqrt{1 - \frac{n_e e^2}{\epsilon_0 m_e \omega_0^2}} \approx 1 - \frac{1}{2}\frac{n_e(r) e^2}{\epsilon_0 m_e \omega_0^2}. \tag{2.37}$$

It can be expanded using equation 2.36 to give

$$\eta(r) \approx 1 - \frac{1}{2}\frac{n_e e^2}{\epsilon_0 m_e \omega_0^2} - \frac{1}{2}\frac{e^2}{\epsilon_0 m_e \omega_0^2}\Delta n_e \left(\frac{r}{r_{\mathrm{ch}}}\right). \tag{2.38}$$

As in relativistic self-focusing, the refractive index is greater on axis, therefore the plasma density profile acts as a focusing lens. A Gaussian laser pulse in a parabolic plasma channel will propagate without diffraction for a matched laser spot size [81]

$$\omega_M = \sqrt[4]{\frac{r_{\mathrm{ch}}^2}{\pi r_e \Delta n_e}}, \tag{2.39}$$

where $r_e = e^2/(4\pi\epsilon_0 m_e c^2) \approx 2.82$ fm is the classical electron radius.

2.5 x-ray production in laser wakefield accelerators

Electrons injected into the plasma wave at a position displaced from the laser axis experience both a transverse and a longitudinal force, which results in transverse motion known as betatron oscillations. This results in the emission of electromagnetic radiation in the hard x-ray region of the spectrum due to the transverse acceleration of individual particles. The equation of motion of electrons undergoing betatron oscillations can be derived from the fields due to charge separation in the wake and Gauss' law [61, 62, 140–

143]

$$\frac{d\mathbf{p}}{dt} = -\frac{1}{2} m_e \omega_p^2 r_\perp, \tag{2.40}$$

where $r_\perp$ is the transverse position of electrons relative to the laser axis. Electrons undergoing betatron motion oscillate at the betatron frequency, which is given by

$$\omega_\beta = \frac{\omega_p}{\sqrt{2\gamma}}. \tag{2.41}$$

The equation of motion can be integrated to give the path of the electrons as they travel through the plasma. When the longitudinal acceleration of the electrons is neglected, the motion is sinusoidal as shown in the red trace in figure 2.10. When relativistic effects and the longitudinal acceleration of the electrons is taken into account, the amplitude of the oscillations decrease proportional to $\gamma^{1/4}$ [7] and the oscillation frequency decreases proportional to $1/\sqrt{2\gamma}$.

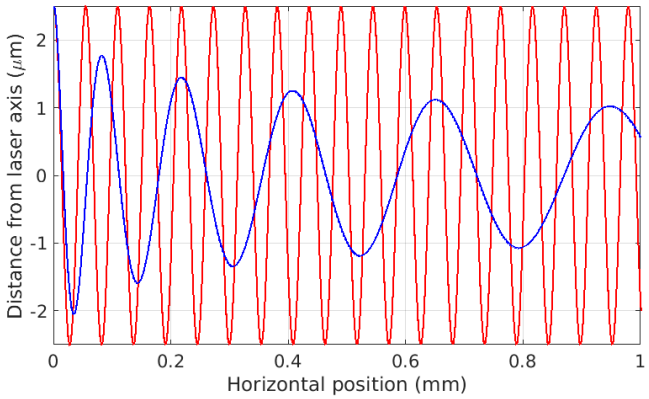

Figure 2.10: Trajectory of a single electron oscillating in an ion channel in the linear (red) and nonlinear (blue) regime. Initial conditions are $r_\beta = 2.5$ µm, $n_e = 1.5 \times 10^{19}$ cm^{-3}, $\gamma_0 = 20$ (10 MeV). In the case of the nonlinear oscillations, the electrons accelerates in a field equal to the cold wavebeaking limit, $E_{wb} \approx 372$ GV m^{-1}.

Betatron oscillations and the process of emitting radiation is analogous to an undulator or wiggler emission [144], where the wiggler strength parameter K is defined as

$$K = a_\beta = k_p \sqrt{\frac{\gamma}{2}} r_\beta, \tag{2.42}$$

where γ is the electron relativistic factor and r_β is the betatron oscillation amplitude.

The radiation spectrum of electrons undergoing betatron oscillations is calculated from the electron trajectory and the Liénard-Wiechert potentials. The amount of radiated intensity per unit angular frequency, per unit solid angle is given by [7]

$$\frac{d^2I}{d\omega d\Omega} = \frac{e^2}{16\pi^2\epsilon_0 c}\left|\int_{-\infty}^{\infty} e^{i\omega[t-\mathbf{n}\cdot\mathbf{r}(t)/c]}\frac{\mathbf{n}\times[(\mathbf{n}-\boldsymbol{\beta})\times\dot{\boldsymbol{\beta}}]}{(1-\boldsymbol{\beta}\cdot\mathbf{n})^2}dt\right|^2, \tag{2.43}$$

where $\boldsymbol{\beta}$ is the electron velocity normalised to c, $\mathbf{n}$ is the direction of observation and $\mathbf{r}(t)$ is the electron position at time t.

When $a_\beta \geq 1$ the synchrotron radiation emitted by an oscillating electron occurs at the resonant frequency as well as harmonics of the resonant frequency [61, 145–148]. In the asymptotic limit, when $a_\beta \gg 1$, the harmonics become so closely spaced that they overlap causing the spectrum to become a broadband continuum. The Liénard-Wiechert potentials can be solved for $a_\beta \gg 1$ giving

$$\frac{d^2I}{d\omega d\Omega} = N_\beta \frac{3e^2}{2\pi^3\epsilon_0 c}\frac{\gamma^2\frac{E}{E_c}}{1+\gamma^2\theta^2}\left[\frac{\gamma^2\theta^2}{1+\gamma^2\theta^2}K_{1/3}^2\left(\frac{E}{E_c}\right)+K_{2/3}^2\left(\frac{E}{E_c}\right)\right]. \tag{2.44}$$

If we consider on axis radiation only where $\theta = 0$ and rewriting the photon angular frequency to photon energy ($E = \hbar\omega$), the radiation for electrons undergoing betatron oscillations becomes [61, 140, 143, 149, 150]

$$\frac{d^2I}{dEd\Omega} = N_\beta \frac{3e^2}{2\pi^3\hbar\epsilon_0 c}\gamma^2\left(\frac{E}{E_c}\right)^2 K_{2/3}^2\left(\frac{E}{E_c}\right), \tag{2.45}$$

where E is the photon energy, N_β is the number of betatron oscillations, γ is the electron relativistic factor and $K_{2/3}$ is the modified Bessel function of the second kind, E_c is the critical energy of the spectrum, which is the photon energy where half of the total emitted energy is below E_c and half is above it, given by [7]

$$E_c = \frac{3\hbar}{4c}\gamma^2\omega_p^2 r_\beta. \tag{2.46}$$

γ and ω_p are both experimental measurable quantities. Figure 2.11 shows the solution to

equation 2.45 for typical electron and plasma parameters obtainable in the Strathclyde laboratory. The broad synchrotron shape to the spectrum can be seen where the critical energy is marked in red.

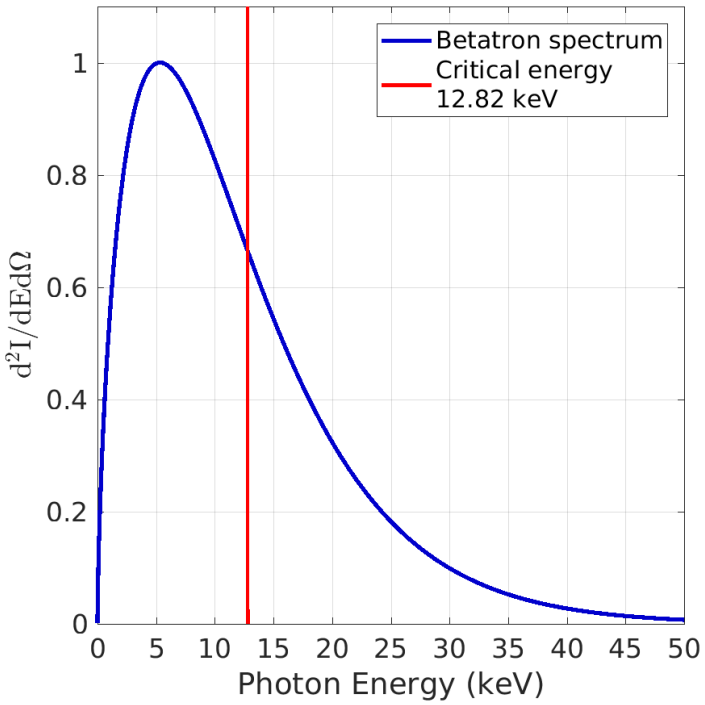

Figure 2.11: Calculated on-axis betatron spectrum for a single electron with energy 130 MeV, $n_e = 1.5 \times 10^{19}$ cm^{-3} and $r_\beta = 2.5$ µm, giving critical energy of 12.8 keV.

Radiation emitted in the direction of laser propagation has a divergence angle inversely proportional to the electron energy and proportional the wiggler strength parameter

$$\theta = \frac{a_\beta}{\gamma}, \tag{2.47}$$

where θ is the half angle of the divergence. For each betatron oscillation, $N_{ph} = (2\pi/9)a_\beta\alpha_f$ photons are emitted per electron, where $\alpha_f \sim 1/137$ is the fine structure constant [151]. Betatron radiation from laser wakefield accelerators can reach the gamma-ray spectral region $>$ 1 MeV [63], pulse durations of tens of femtoseconds [152] and a peak brightness of more than 10^{23} photons/s/mm^2/mrad^2/0.1% BW

[63, 149, 153].

2.6 XUV production in laser wakefield accelerators

The emission of extreme ultraviolet (XUV) radiation from a laser wakefield accelerator has not been study extensively either experimentally or theoretically. Work led by Alexander Pirozhkov in Japan observed forward direction radiation between $80-400$ eV consisting of both even and odd harmonics of the laser frequency [154–157], with a spectral brightness of 40 $\mu J\,sr^{-1}$ or 10^{12} photons sr^{-1} in a single harmonic at 120 eV. Using a 120 TW laser [154, 155] they observed that the brightness decreases exponentially with increase in photon energy. Later experiments observed intense radiation emitted at small angles ($8-18^{\circ}$) from the laser axis and in the plane of the laser polarisation. By imaging the source using a multilayer mirror, they revealed that the radiation arises from two point-like emitters separated by 12 µm, approximately the plasma bubble diameter [156].

The group [156] used simulations to interpret the harmonic radiation as arising from electrons in the bow wave at the point where the trajectories of sheath electron cross. Due to high laser fields at this point electrons oscillate with highly nonlinear motion resulting in the emission photons at both even and odd harmonics of the frequency of the driving laser pulse. Since the electron oscillation in the density spike is high only in the plane of the electric field of the laser pulse, the radiation is emitted as two point-like source separated by the plasma bubble diameter. This was confirmed by focusing the radiation with a spherical mirror where the two spots were observed separated by 12 µm. Figure 2.12 shows a plasma wakefield with the presence of the density spikes described by Pirozhkov et al., using laser and plasma parameters typically used in the Strathclyde laboratory where a smaller than achievable laser waist was chosen to shorten computation time by assuming the laser pulse self focuses from its real value around 50 µm. For the simulation parameters chosen, the laser pulse almost completely fills the bubble since the laser pulse length is approximately equal to the plasma wavelength. The electric field of the laser at the bow wave is high, around

3×10^{12} V m^{-1}, driving the oscillations of the high density spike.

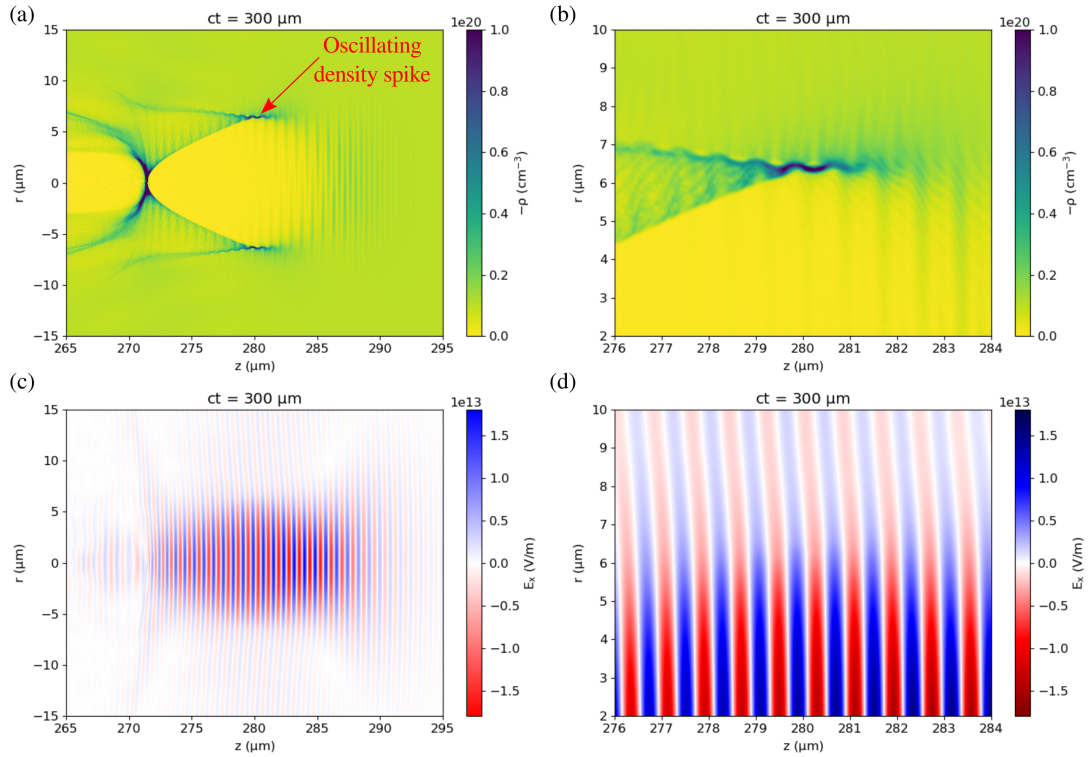

Figure 2.12: (a) and (b) Demonstration of the oscillating density spike in the bow wave of the electron density wave of a laser wakefield accelerator. (a) shows full simulation window and (b) is a blow-up of the region around the cusp. (c) and (d) Electric field of the laser in both the full simulation window (c) and the blow-up around the cusp (d). The simulation was performed in fbpic for a 40 TW laser pulse with initial conditions $a_0 = 3.48$, $\lambda_0 = 800$ nm, $w_0 = 7$ µm, $\tau_{\mathrm{FWHM}} = 35$ fs and plasma density of $n_e = 1.0 \times 10^{19}$ cm^{-3}.

Chapter 3

Experimental facilities

SCAPA is a new facility for experimental laser-plasma interaction physics in Glasgow, Scotland. It houses two high-power short-pulse Ti:sapphire laser systems, based on chirped pulse amplification, with peak powers of 40 TW and 350 TW, respectively. With a repetition rate of 5 Hz and pulse energy of 8.75 J, the SCAPA 350 TW laser is currently (2018) the world's highest average power laser of its kind. A summary of the parameters of the lasers available at SCAPA are shown in table 3.1. The lasers at SCAPA deliver beams to the three shielded experimental areas, known as bunkers, which have been designed to house up to seven experimental beam lines that cater for a wide range of experiments from utilising laser wakefield accelerated electrons for medical applications [57, 158–160] to accelerating ions using thin solid targets [105, 161–163]. The experiments are conducted inside bunkers, which act as radiation shields to protect users from radiation produced by the laser-plasma interaction. The walls of the bunkers are 1 m thick concrete and access to and from them is via an equally thick concrete door that is pneumatically opened and closed on a cushion of compressed air.

All of the experiments presented in this thesis have been conducted using the ALPHA-X (Advanced Laser Plasma High energy Accelerator towards x-rays) beam line and 40 TW laser, initially in its original location in the ALPHA-X laboratory then subsequently in its new location in Bunker C of SCAPA.

	40 TW	350 TW
Central wavelength (nm)	800	800
Energy after compression (J)	1.4	8.75
Pulse duration (fs)	35	25
Repetition rate (Hz)	10	5
Uncompressed probe beam energy (mJ)	30	300
Strehl ratio		≥ 0.85

Table 3.1: Parameters for each of the high-power lasers at the SCAPA facility. Energy given is the laser energy after compression.

3.1 SCAPA 40 TW laser

Ultrashort laser pulses with peak powers of terawatts (10^{12} W) or petawatts (10^{15} W) are generated by chirped pulse amplification (CPA) [15, 164], a technique first developed by Donna Strickland and Gérard Mourou, who were awarded the Nobel prize in physics in 2018 for the impact that CPA lasers have had on science and industry. A CPA system comprises four main components. First, a laser oscillator generates short duration laser pulses of low energy. These pulses are then stretched in time to prevent damage to optical components in subsequent amplification stages. The oscillator pulses are then amplified several billion (10^9) times to the Joule level. Finally, the amplified pulses are re-compressed to femtosecond duration to achieve a high peak power. This section describes each of the stages in a CPA laser with the Strathclyde 40 TW [165] laser as an example, the layout of which is shown in figure 3.1. The Ti:sapphire lasers are commonly used for investigating wakefield acceleration because the emission from the crystal peaks around 800 nm and the bandwidth is extremely broad. Because the ponderomotive force scales with wavelength, infrared lasers are well suited to drive nonlinear plasma waves required for acceleration of quasimonoenergetic electrons. Secondly, the broad bandwidth, from 660 to 1050 nm, implies a Fourier transform that ensures compression to short durations required for efficiently driving plasma waves.

3.1.1 Femtosecond oscillator

The laser oscillator in a chirped pulse amplification laser system acts as the source of ultrashort (fs) pulses of laser light at a regular interval to be amplified. It consists of

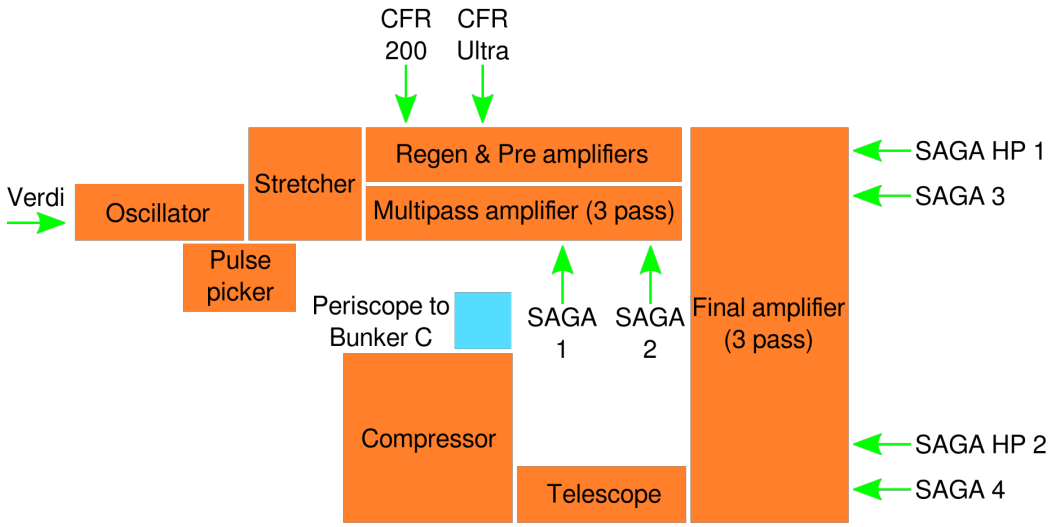

Figure 3.1: Schematic showing the general layout of the 40 TW laser as configured in the SCAPA laboratory. The green arrows represent each of the doubled Nd:YAG pump lasers indicating the section of the laser where they are used.

a laser cavity with a Ti:sapphire crystal as a gain medium, cut at Brewster's angle to reduce losses due to reflection, which is pumped by the second harmonic of a Nd:YAG laser (532 nm). In the case of the oscillator for the 40 TW laser, the titanium sapphire crystal is pumped with a 6 W (Coherent Verdi) continuous wave (CW) laser.

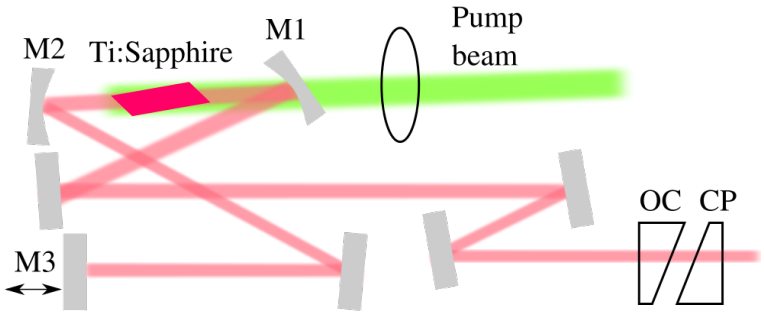

Figure 3.2: Schematic of Femtosource synergy 20s laser oscillator used in the 40 TW laser.

The cavity consists of two mirrors, M1 and M2, which focus light into the Ti:sapphire crystal. The wedges OC and CP (output coupler and compensating plate) maintain stimulated emission by reflecting the majority of the laser light back towards the crystal

but allow an output from the cavity as well as correct for dispersion, which is added to the pulses when they pass through the Ti:sapphire crystal due to self-phase modulation. This is necessary for creating ultrashort pulses [166, 167].

Emission from the crystal results in many longitudinal standing waves existing inside the cavity and a continuous output from it. When the intensity of the laser light inside the cavity becomes high, the Kerr lensing effect inside the titanium sapphire crystal couples the modes of the laser cavity together due to nonlinear self focusing. The interference between the cavity modes results in the creation of a train of short duration laser pulses with a regular spacing from the initial CW light created by the cavity as shown in figure 3.3 [167, 168]. This process is referred to as self mode locking, which was first demonstrated by Spence et al., in 1991 generating pulses less than 300 fs [166].

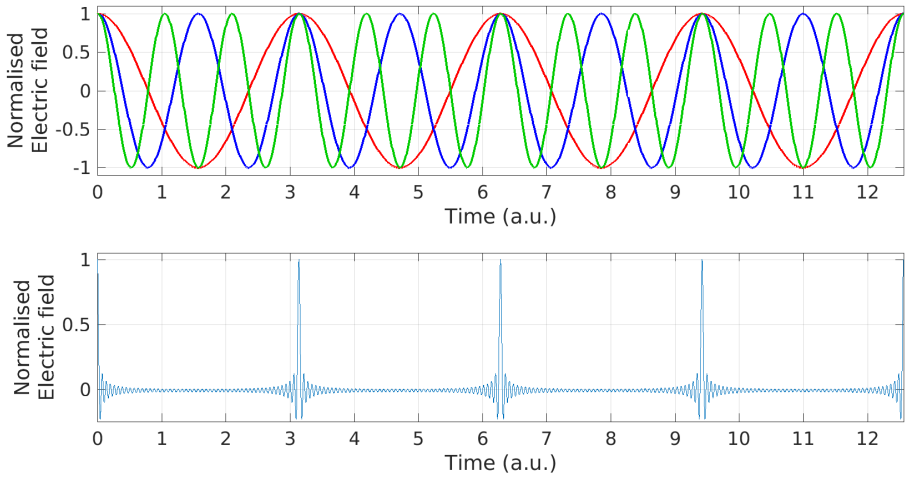

Figure 3.3: (a) First three longitudinal standing waves inside laser oscillator cavity. (b) Summation of 50 cavity modes creating short pulses at regular intervals.

A Kerr lens if formed by the nonlinearities in the refractive index of the crystal, which only become significant at high intensities. The refractive index of a material is the sum of a constant linear component and a nonlinear component proportional to the laser intensity. Since the laser light has a Gaussian intensity profile the refractive index, and therefore the laser group velocity, of the crystal depends upon the radial position of the laser relative to its axis similar to laser self focusing in a plasma described in

section 2.4.3

$$n(r) = n_0 + n_2 I(r), \tag{3.1}$$

where is n_0 the linear refractive index (1.76 at 800 nm), I is the laser intensity and $n_2 \approx 3 \times 10^{-16}$ cm^2 W^{-1} is the Kerr coefficient of Ti:sapphire [169]. Kerr lensing on its own is not sufficient for mode locking to be initiated from noise so a strong fluctuation is induced into the cavity length by perturbing mirror M3 [170, 171]. The oscillator for the 40 TW laser produces $<$ 20 fs duration pulses with 9 nJ energy, central wavelength 800 nm, 40 nm bandwidth and a 75 MHz repetition rate. A measurement of the spectrum is made daily as a health check of the oscillator.

3.1.2 Stretcher and compressor

Stretcher

To prevent damage to optical components that would occur from directly amplifying an ultrashort pulse, pulses from the oscillator are stretched in time by 12,500 times from $\approx$ 20 fs to $\approx$ 250 ps, by adding a positive chirp to the pulse.

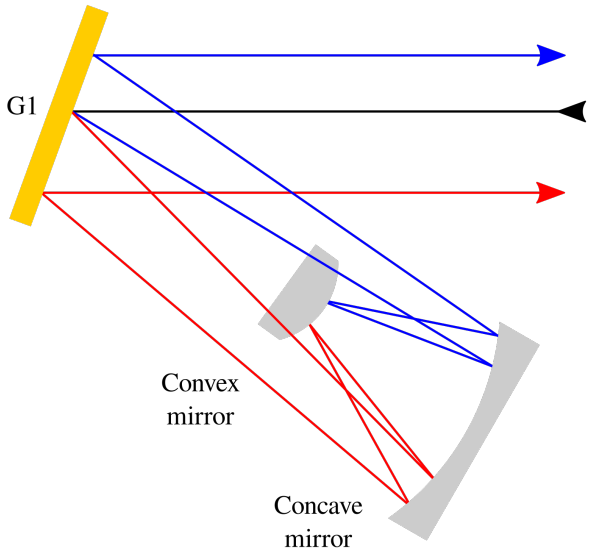

Figure 3.4: Schematic of single pass through the TOPS laser stretcher based on Offner triplet configuration.

The pulse stretching is achieved using a Offner triplet combination [172–174] com-

prised of only reflecting components, a diffraction grating, a concave mirror and a convex mirror where the path length travelled by the laser is a function of wavelength. This design is symmetric so that only symmetrical aberrations (spherical aberrations and astigmatisms) can appear, whereas in a stretcher based on two lenses forming a 1:1 telescope, result in both spherical and chromatic aberrations.

The radii of curvature of the two mirrors is chosen such that the concave mirror has twice the focal length of the convex mirror and they are arranged such that the focal positions of both optics occurs at the same point with magnification of $M = 1$. The grating must be positioned outside the centre of curvature of the two mirrors otherwise the laser pulse duration will remain unchanged. A sketch of the stretcher used in the 40 TW is shown in figure 3.4. In the first pass, the beam diffracts off the grating, passing over the convex mirror to the concave mirror, and then to the convex mirror. The beam then returns to the concave mirror and then under the convex mirror, where it again diffracts off the diffraction grating. A periscope raises the height of the beam and an identical second pass of the stretcher is made. In total the laser impinges on the diffraction grating a total of four times.

Stretching is achieved by shortening the path length for the short wavelength components of the pulse and lengthening the path length of the long wavelength components of the pulse. The stretcher is a highly dispersive element dispersing the frequency components in time. The degree of stretching is determined by the groove spacing of the diffraction grating, the total number of passes through the stretcher and its path length, set by the radius of curvature of the two spherical mirrors. A pulse picker consisting of a Pockles cell, waveplate and polariser then selects a 10 Hz train of pulses from the 75 MHz oscillator beam before passing the beam on to the chain of amplifiers.

Compressor

Once the laser pulse has been amplified to the Joule level, as discussed in section 3.1.3, the beam is directed through a telescope to increase the beam size to 4 cm diameter. This is done to reduce the fluence (energy per unit area) of the beam below the damage threshold of the diffraction gratings used in the compressor.

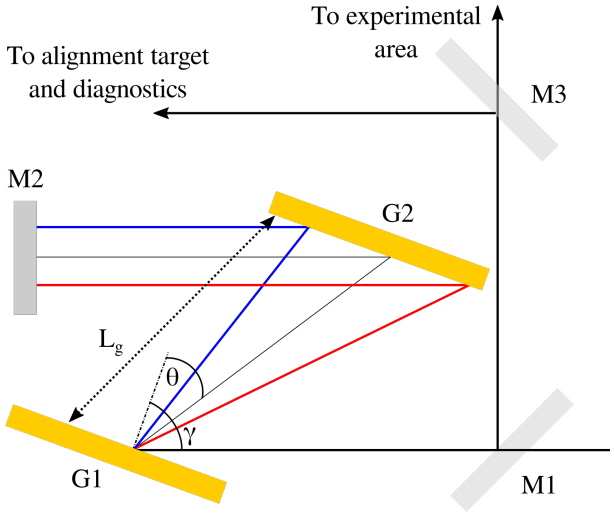

Figure 3.5: Schematic of the ALPHA-X, TOPS, laser compressor. Rooftop mirror M2 directs the beam through two passes of the gratings. Mirror M3 is translated out of the beam path to allow the high power laser to the target area. The distance between the gratings L_{g} can be adjusted by translating grating G2.

The laser pulse compressor is contained within a vacuum chamber and pulses from the telescope enter through a window into the chamber. The laser pulse compressor consists of two parallel gratings that introduce a dispersion that removes the chirp added by the stretcher. The compressor configuration, first described by Treacy in 1969 [175], fully compresses the pulses. By use of mirror M2 two passes of the gratings are made, initially using their top halves and then, on the second pass, the lower half of the gratings.

The optical path length inside the compressor is given by

$$P = \frac{L_{\mathrm{g}}}{\cos(\theta)} \left[1 + \cos(\gamma - \theta)\right], \tag{3.2}$$

where L_{g} is the spacing between the gratings and γ is the angle of the gratings. θ is diffraction angle of the laser beam, which is a function of wavelength according to the grating equation

$$\sin(\theta) = \frac{\lambda}{d} - \sin(\gamma), \tag{3.3}$$

where λ is the radiation wavelength and d is the groove spacing of the grating. Since

the diffracted angle is larger for longer wavelengths, the pulse is negatively chirped and as a result compressed in time. Grating G2 is mounted on a linear motorised translation stage allowing the amount of compression to be controlled and for the optimum pulse duration to be found. The design of the compressor has been a major limitation to the quality of the laser pulses. Clipping on the edges of the gratings and the roof-top mirror (M2) results in a loss of beam energy and a distortion of the beam profile. This introduces spatial and frequency aberrations that limits the focusability and temporal properties of the laser pulse. The compressor compresses the stretched pulses to 35 - 40 fs FWHM with an efficiency of $\approx 67\%$.

3.1.3 Pulse amplifiers

The 40 TW laser at SCAPA amplifies laser pulses using a chain consisting of one regenerative and three multi-pass amplifiers increasing the beam energy from 9 nJ to 2 J.

Regenerative amplifier

The first laser amplifier in the chain is a regenerative amplifier operating at 10 Hz, which raises the energy of the pulse from 9 nJ to 1 mJ using Pockels cells, waveplates and polarisers to control when pulses enter and exit the amplifier cavity.

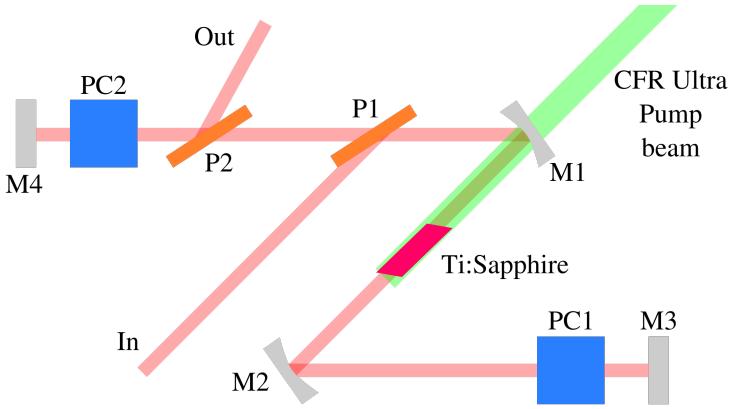

Figure 3.6: Schematic of the regenerative amplifier with mirror M1 - M4, polarisers P1 and P2 and Pockles cells PC1 and PC2.

Laser pulses from the stretcher are horizontally polarised so polariser P1 reflects them into the cavity of the regenerative amplifier. The pulses are trapped inside it by applying a constant potential difference across the Pockles cell PC1, which rotates the polarisation of the light passing through it by 90°. The change in polarisation allows the light make a number of passes of the cavity, between mirrors M3 and M4, before Pockles cell PC2 rotates the polarisation of the pulse back to its original state at a time when the pulse reaches its maximum energy level. The rotation in polarisation by PC2 allows the laser to be reflected out of the cavity by polariser P2, ready for the next amplification stage. The Brewster cut titanium sapphire crystal inside the regenerative amplifier is pumped by a CFR Ultra laser producing 30 mJ, 9 ns pulses at 532 nm.

Multipass amplifier

Pulses from the regenerative amplifier are passed through three multipass amplifiers that direct laser pulses through the gain medium several times at different angles. The layout of a multipass amplifier is shown in figure 3.7.

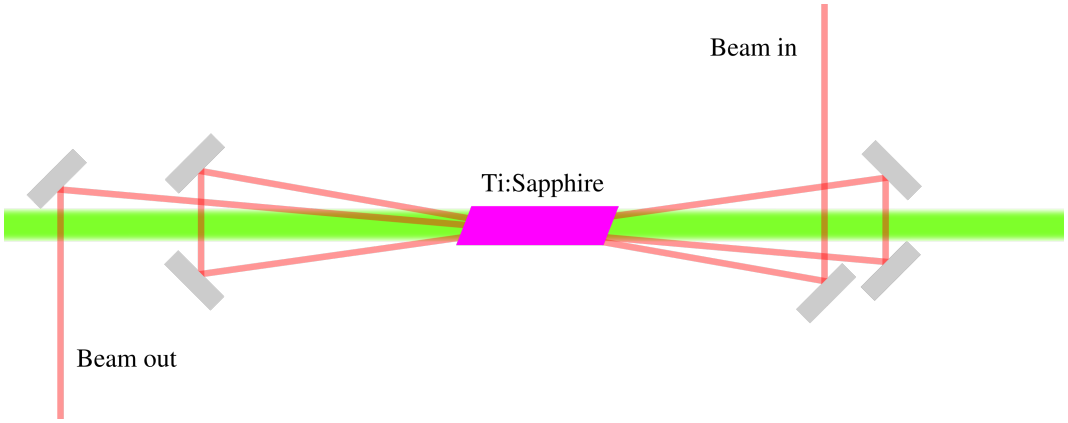

Figure 3.7: Schematic of a 3 pass multipass amplifier as used in the final two amplifier stages. The titanium sapphire crystal is pumped on both sides by the second harmonic of a Nd:YAG laser.

The first multipass amplifier, referred to as the pre-amplifier of the laser chain, directs the beam through a Ti:sapphire crystal five times taking the beam energy from 1 mJ to 12 mJ. The crystal is pumped by a CFR 200 laser operating at a

10 Hz repetition rate with pulse energy and duration of 130 mJ and 9 ns, respectively. The number of passes chosen for the amplifier depends upon the gain saturation of the amplifying medium so after the five passes in the pre-amplifier, the pulse energy saturates. The Ti:sapphire crystal of each of the laser amplifiers is water cooled to prevent thermal lensing inside the crystal. Laser alignment only takes place when the lasers and crystals have reached their operating temperatures (a balance between heating from lasers and the water cooling), to avoid misalignment due to thermal effects.

The pulses are then sent to a second multipass amplifier pumped from either side by a B.M. Industries SAGA laser producing 800 mJ at 532 nm. The pulses traverse the crystal three times, raising the pulse energy from 12 to 320 mJ.

Before entering the final amplifier, the laser spectrum and energy, with and without time delays for the pump lasers in the second multipass, are measured to ensure the correct amplification is being achieved and to check the alignment of the front end of the system. Higher order transverse modes are then removed by focusing the beam through a glass spatial filter to improve the quality of the beam before the laser reaches the final amplification stage. The focused laser intensity even at this stage is high so to prevent nonlinear effects in the air disrupting the beam quality, the spatial filter is kept under vacuum with pressure $\sim 10^{-3}$ mbar. The laser then makes three passes through the final amplifier where a Ti:sapphire crystal pumped by two Thales SAGA HP lasers (1.6 J at 532 nm) and two Thales SAGA lasers (1.2 J at 532 nm). This amplifies the beam to its final energy (before compression) of 2 J.

3.2 Laser beam transport

The most significant change to the laser system between the two experiments presented in this thesis is the laser beam transport from the final amplifier to the spherical focusing mirror. In the first experiment carried out when the laser was in the ALPHA-X laboratory, the laser pulses travelled around 10 m from the final amplifier to the compressor, and then a further 4 m to the spherical mirror. The laser, in its new location inside the SCAPA laboratory, is placed directly above the beam line. The beam transport from the final amplifier to the compressor is now just the length required by

the telescope to expand the beam before compression. From the compressor, a periscope directs the beam through the floor into bunker C, where is reflected by three further mirrors (including the spherical mirror) to focus it onto the target, the distance is totality from the exit of the compressor to the gas jet is 6 m. The shorter transport distance and fewer mirrors results in less beam loss and therefore an increase in energy on target, compared with the previous configuration.

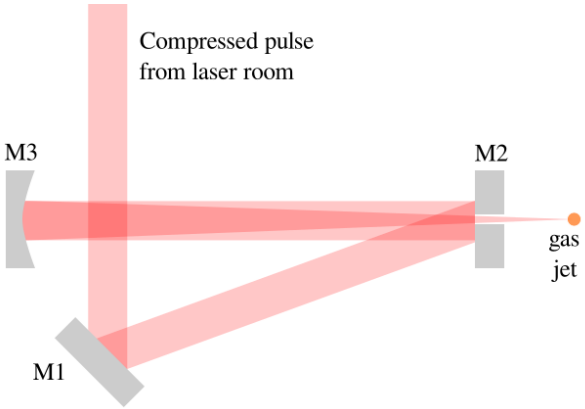

Figure 3.8: Final focusing system for the 40 TW laser, consisting of mirror M1, mirror with 6 mm hole (M2) and the $f = 76$ cm spherical mirror (M3).

The final focusing system in the SCAPA laboratory is shown in figure 3.8. From the output of the compressor, the beam is sent directly into Bunker C using a periscope, mirror M1 then is reflected to the final focusing system, which consists of a plane mirror with a 6 mm diameter hole drilled in it (M2) and a spherical mirror of focal length $f = 76$ cm ($f/18$) that focuses the laser to a point just above the gas jet. Laser alignment is undertaken at the lowest possible power because laser light clipping the edge of the hole in M2 can damage the coating of the mirror and lead to loss of energy and deformation of the beam profile at the focus. The final three optics to focus the laser as in the ALPHA-X/TOPS laboratory. In both cases, the spherical mirror (M3) focuses pulses, back through the mirror M2 to the gas jet. Figure 3.9 shows a typical laser spot, recorded at high power, using a beamsplitter to direct the laser light out of the vacuum chamber to a CCD camera with 4× magnification objective lens. The wings around the main spot are expected since mirror M2 leaves the beam with a hole

in the centre and the intensity distribution matches the Fourier transform of a Gaussian distribution with a hole in the centre. A three dimensional least squares fit is used to calculate the spot diameter with an average value of 52.7 µm in the minor axis and 56.9 µm in the major axis.

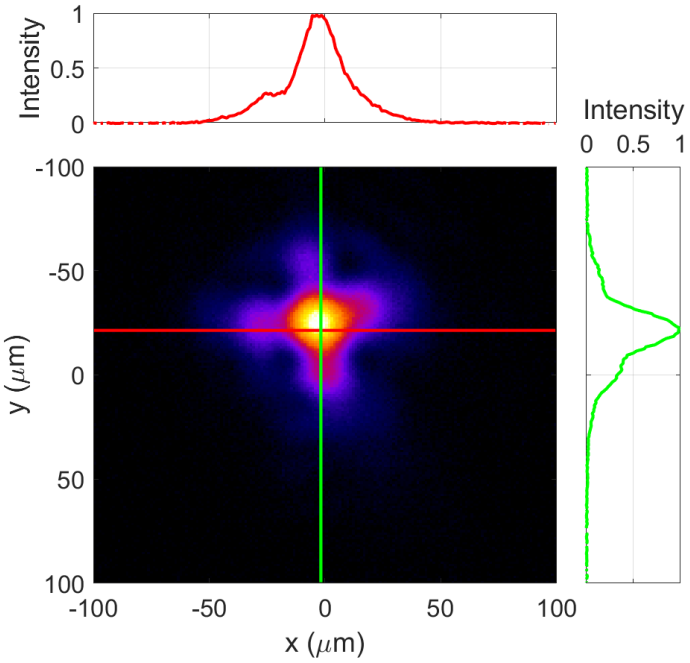

Figure 3.9: Example laser focus at high power. Least squares fit gives spot diameter to $1/e^2$ of 54.5 × 55.6 µm

3.3 ALPHA-X beam line

The ALPHA-X (**A**dvanced **L**aser **P**lasma **H**igh-energy **A**ccelerators towards **X**-rays) beamline [51] is a laser wakefield acceleration beamline inside Bunker C of the SCAPA facility designed to host a wide variety of underdense laser-plasma interaction experiments. An example layout of the beam line in figure 3.10 shows the full suite of available equipment and diagnostics.

Pulses from the 40 TW laser are focused onto the leading edge of a 2 mm diameter outlet supersonic gas jet (described in the next section). Plasma densities between of

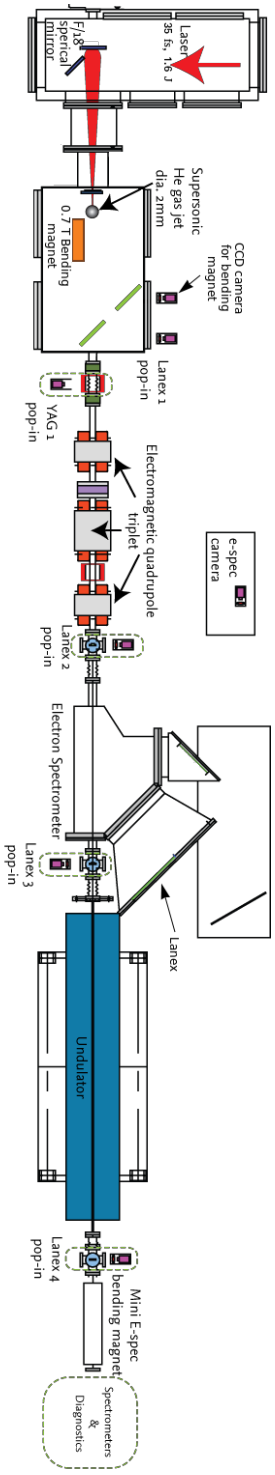

Figure 3.10: ALPHA-X beamline.

1 and 2×10^{19} cm^{-3} are typically used.

A permanent bending magnet, placed 100 mm after the gas jet, is used as a spectrometer to measure the electron beam energy and energy spread. The magnet is 210 mm long and has a field strength of 0.7 T and directs the beam towards two scintillating (Kodak Lanex) screens, marked as Lanex-1 and "CCD camera for bending magnet" in figure 3.10. The two screens act as a low and high energy window with a gap between them corresponding to $100 - 120$ MeV, each of the two screens are imaged individually with their own CCD camera (Pointgrey Flea3).

The high energy screen from the spectrometer can be pushed directly into the laser path to act as a beam profile monitor inside the main interaction chamber, labelled Lanex-1 in figure 3.10, which is positioned at 40° relative to the laser propagation direction. To reduce noise and filter out the laser light, the Lanex is protected with a 50 µm sheet of aluminium foil. There are a number of additional beam profile monitors in the beam line placed at different positions (labelled Lanex 2 – 4 and YAG1) by pneumatically actuated Lanex screens. Fluorescence from the each screen are measured with a monochrome 12-bit Pointgrey Flea2 or Flea3 CCD cameras with objective lenses.

A set of electromagnetic quadrupole magnets 1.2 m after the chamber forms part of the beam transport system. These are used to focus the electron beam into a second electron spectrometer or into an undulator. An electromagnetic spectrometer with maximum field strength of 1.7 T is placed 2.6 m after the gas jet and offers higher resolution than the permanent magnet spectrometer due to the focusing fields in both the horizontal and vertical directions. For a field strength of 0.56 T the resolution of the electromagnetic spectrometer is $0.5 - 1.0$ % in the range $76 - 227$ MeV. Electron spectra are recorded using a Lanex screen placed at the focus of the spectrometer, which is imaged using a 14-bit CCD camera (GRAS-14S5M-C). A 100 period, 1.5 m long undulator ($B = 0.27$ T) can be used to generate ultraviolet light with wavelengths between 70 and 260 nm [58, 176].

3.3.1 Gas jet

The plasma source for the each of the experiments took the form of a gas jet which was designed by Dr Constantin Aniculaesei and described in his PhD thesis [80]. Nozzle 511 was used which has a 2 mm diameter outlet. The nozzle uses a de Laval geometry connected to a fast solenoid Parker valve [177] to allow a supersonic pulse of helium gas to travel through the nozzle and into the vacuum. The valve delivers a short plume of helium gas with backing pressures between 15 and 60 bar. The valve opening duration of 3 ms is timed to coincide with the arrival of laser pulse. Since the laser intensity threshold for ionisation is on the order of 10^{15} W cm^{-2}, the leading edge of the laser pulse is sufficient to ionised the gas creating a plasma. Computational fluid dynamics simulations using ANSYS Fluent, shown in figure 3.11, and courtesy of Dr Enrico Brunetti shows how the plasma density varies as a function of helium gas backing pressure for a constant separation between the laser and the top of the nozzle of 4 mm. The geometry of the nozzle, gas backing pressure and height of the laser relative to the top of the nozzle determine the plasma density as well as the flatness of the density profile which lies between density up and down ramps.

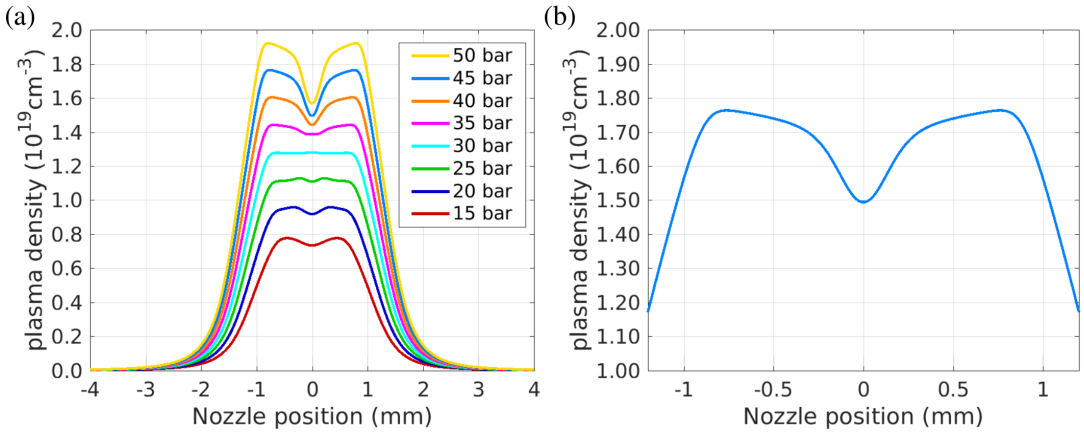

Figure 3.11: Simulated plasma density profiles for 4 mm above 511 nozzle where 0 is the nozzles centre. (a) Density profiles for gas backing pressures between 15 and 50 bar. (b) Density profile at 45 bar only for 1.2 mm either side of the centre of the nozzle. Simulations performed by Dr Enrico Brunetti using ANSYS Fluent.

3.3.2 McPherson spectrometer

The spectra of XUV light from the plasma is measured using a McPherson 248/310 grazing incidence spectrometer, which uses a Rowland circle design of radius 1 metre and 20×25 mm rectangular diffraction grating at a grazing angle of 87°. The entrance slit of the spectrometer has an adjustable width from 1 to 500 µm and a fixed height of 1.5 cm. Although it is optimised for < 50 nm it has a full working range from 1 to 310 nm. For high quality measurements of radiation with wavelengths > 50 nm, a McPherson 234/302 spectrometer is also available in the laboratory. Diffraction gratings with 133.6, 300, 600, 1200 lines mm^{-1}, optimised for different wavelengths can be easily inserted in the 248/310 spectrometer. Raw images of the spectra are recorded using a 1024×256 pixel back-illuminated Newton, Andor CCD camera (DO920P-BN-995) that has a 26 µm pixel size and is optimised for radiation between 10 eV and 10 keV. A calibration for the spectrometer to find the wavelength corresponding to a given column of pixels on the CCD camera is obtained using the transmission edges of the thin metal filters used to block the laser. Aluminium has an L edge at 17 nm, as shown in figure 3.12(a), where the transmission drops by more than an order of magnitude. This is clearly observed in images recorded by the CCD camera, for example in 3.12(b).

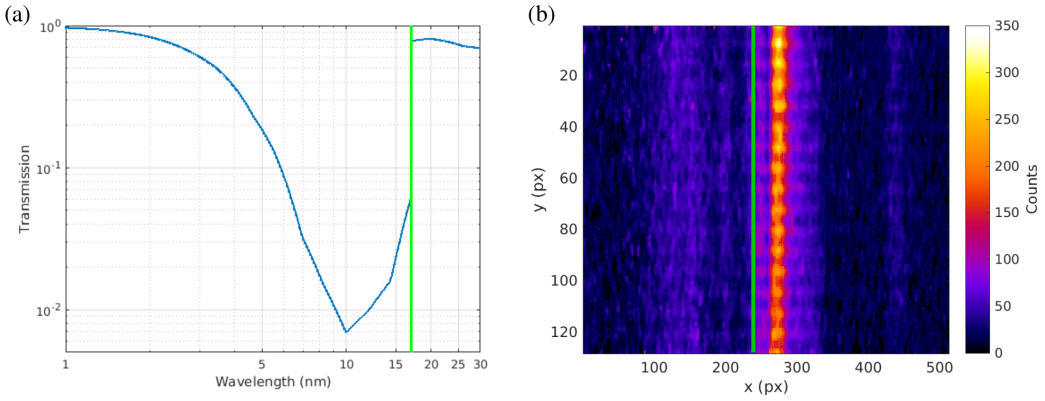

Figure 3.12: (a) Transmission plot for 150 nm thick aluminium filter. (b) Image recorded with McPherson 248/310 spectrometer and Andor Newton camera. In each case, the transmission edge at 17 nm is marked in green.

To provide calibration points from the measured wavelength values, the average position of the peak with each filter from the images recorded with the CCD camera are equated with the average wavelength measured with the same filters. The points obtained (three from double slit and one from the filter transmission) were obtained from a fit to a model for a Rowland circle, where the wavelength at the exit slit is given by

$$\lambda = d\left[\sin(\alpha) - \sin\left(\frac{\cos^{-1}(X)}{r}\right)\right], \tag{3.4}$$

where d is the grating function $\left[1/(\text{grooves/mm}) \times 10^6\right]$, λ is the photon wavelength in nm, α is the angle of incidence in degrees, r is the grating radius in inches, and X is the scanning drive counter reading on the McPherson in inches.

3.3.3 x-ray CCD camera

Images showing the profile of the radiation and the double slit patterns are recorded with a combination of the XUV gazing incidence beamsplitter and the Andor iKon-M (DO934P-BN) back illuminated charged coupled device (CCD) camera. It has a square 13.3 mm sensor with pixel size 13 µm and 1024×1024 pixels. The iKon-M camera has the same sensor material and design as the Newton camera and thus the same spectral range and x-ray response.

The structure of a CCD sensor is shown in figure 3.13(a) where each of the major layers have been labelled. Photons incident on the camera first pass through the electrode structure (or gate electrodes) and a thin oxide layer. They then pass into the photosensitive depletion layer, only photons that deposit their energy in the depletion layer are counted by the camera. If the photon has energy greater than $W = 3.65$ eV, an electron-hole pair is created [179, 180]. Where W is the mean energy required to create an electron hole pair in silicon and is constant between photon energies of 50 to 1500 eV [181]. The free charges move in an electric field of the detector due to a bias voltage across each pixel towards the electrodes so that the electrons can be counted. The number of free electrons and holes created proportional to the incident photon energy so a 1 keV photon will generate $1000/3.65 = 273$ photoelectrons. This

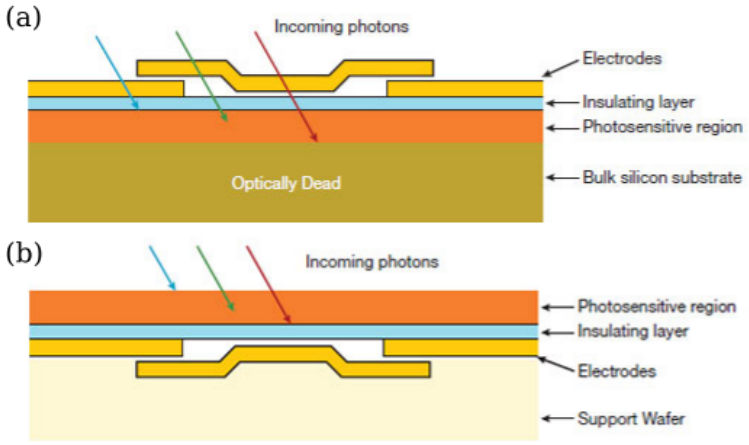

Figure 3.13: Schematic of the cross section of a CCD sensor. (a) Front-illuminated CCD. (b) Back-illuminated CCD. Figure taken from [178]

proportionality between the energy of a photon and number of electrons excited in a pixel of the detector is the basis of the single photon counting method for measuring the x-ray spectrum in chapter 7.

The range of photon energies that can be detected depends upon the thickness of the photosensitive layer and the structure of the electronics photons must pass through to reach it. Some photons, particularly photons in the ultraviolet will be absorbed or reflected by the electrodes and oxide layer so will not be seen by the camera. Similarly, if the photon energy is too high the absorption length of that photon will be greater than the depth of the depletion region resulting in the photon passing through the CCD camera undetected.

The iKon and Newton cameras used in this thesis have sensors that are back-illuminated such that the order of the layers of the electronics which make up the sensor are reversed as illustrated in figure 3.13(b). With the supportive bulk silicon layer almost entirely removed leaving only a thin "dead zone" layer this means that the light absorbing photosensitive region is effectively the first layer of the sensor. This is done to better absorb low energy photons such as photons in the ultraviolet region of the spectrum which would otherwise be absorbed or reflected by the gate electrodes.

The proportion of the total photons incident on the camera that deposit their energy in the depletion layer of the CCD chip is called the quantum efficiency, which takes

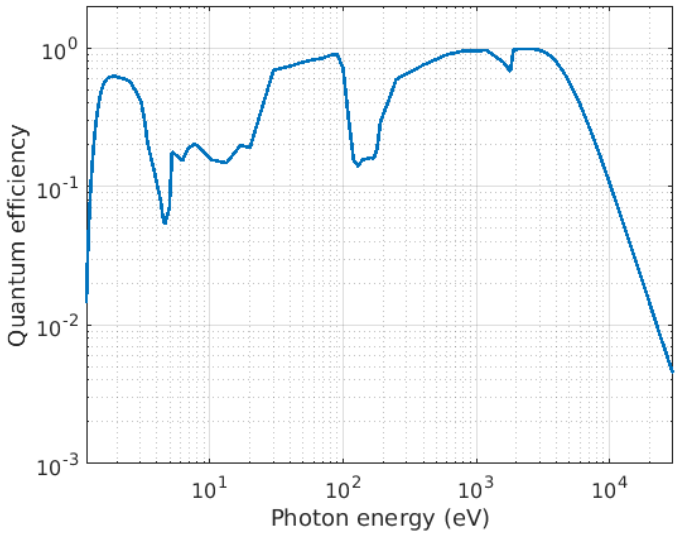

Figure 3.14: Quantum efficiency curve for the Andor iKon-M camera.

into account all the various absorption effects [182]. A quantum efficiency of 0.1 means that one in every ten photons that pass through the camera are detected by it. For the two CCD cameras used in this thesis the quantum efficiency curve as a function of photon energy is given in figure 3.14. The dips that can be seen in the quantum efficiency curve are due absorption edges due to the structure of the silicon atom, for instance the silicon L edge at 100.6 eV can clearly be seen in figure 3.14. We can infer the incident number of photons from the number of counts on the CCD camera. For a pre-amplifier gain 4× and a readout rate of 3 MHz at 16 bit per pixel, the number of photons at a given wavelength is given by

$$N_{ph} = \frac{2.5 \times \text{Counts} \times 100}{\text{Quantum efficiency}} \tag{3.5}$$

where the constant of 2.5 is the CCD sensitivity, a conversion factor between the number of counts in a pixel and the number of electron-hole pairs created which is a result of the analogue to digital converter of the camera. It's value is taken from the calibration preformed by the manufacturer after assembly. The McPherson spectrometer discriminates photons by their wavelength so the photon energy in a particular pixel is

known allowing equation 3.5 to be used. In the case of the profile measurements, the bandwidth of radiation reaching the sensor is limited by the XUV beamsplitter and the metal filters allowing an estimate of the number of photons to be made. To reduce noise from dark current the sensor of the CCD is thermoelectrically cooled to $-70°$C.

To lessen laser light from the high power pulse and prevent hard x-ray betatron radiation from reaching the camera, a 2" diameter planar XUV beamsplitter (NTT-AT) with a Molybdenum coating, grazing at 7.5°, was place directly in the path of the laser axis to reflect XUV light into the CCD camera and transmit laser and betatron photons. Calculation of the reflectivity of the mirror coating using the IMD extension of X-ray Oriented Programs (XOP) [183, 184] is shown in figure 3.15 which calls upon the database for x-ray applications (DABAX) database. This shows that the beamsplitter reflectivity is high in the XUV region made but very poor in the spectral region where betatron radiation is emitted – only a few photons are expected to reach the CCD each shot. All laser radiation should be blocked by the metal filters positioned before the beamsplitter. However, a small amount of laser light is transmitted through pinholes in the filter material, or scattered around the filter carousel. The beamsplitter has a reflectivity $\approx 12\%$ for p-polarised 800 nm photons, which further reduces laser light on the detector.

In analysing the experimental measurement to reconstruct the radiation from the plasma, both the camera quantum efficiency and the mirror reflectivity have been taken into account, in addition to any filters used.

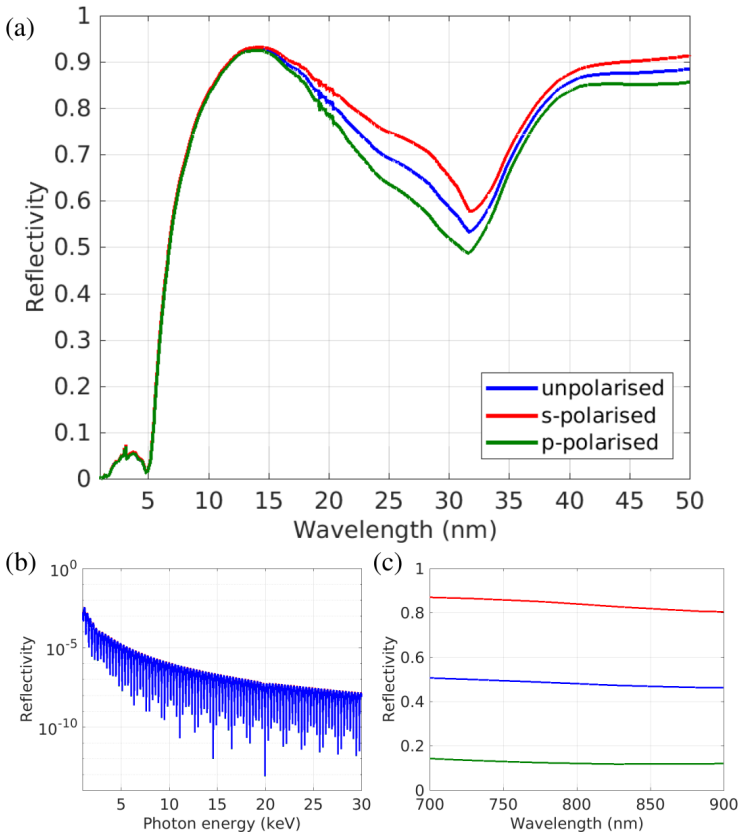

Figure 3.15: Reflectivity curves for the XUV beamsplitter placed at 7.5°, with 15 nm molybdenum coating in the range of (a) the XUV radiation, (b) the betatron radiation and (c) the high power laser pulse.

Chapter 4

Spectral measurements of XUV radiation

This chapter presents an experimental investigation of the emission of XUV radiation in the wavelength range 3−31 nm, emitted directly from the plasma. Spectra are measured using the McPherson 248/310 spectrometer, described in 3.3.2, with the entrance slit set at either 100 or 250 µm (resolution 0.30 or 0.76 nm), placed 3.88 m from the gas jet as shown in figure 4.1. To prevent the high power laser light from entering the spectrometer, a metal filter has been used to block it. However, because no metal filter acted as a perfect short pass filter, the XUV spectra are measured piecewise using three different filter materials: aluminium (Al), zirconium (Zr) and indium (In) separately, which allows the full XUV spectrum to be covered.

Individual measurements are performed in a single shot while simultaneously recording the corresponding image of the plasma filament (observed directly above the gas jet), and the spectrum of high energy electrons (measured using the electromagnetic spectrometer placed at position D1 in figure 4.1). During optimisation of the gas jet position the electron beam is measured with the lanex beam profile monitor (BPM). The beam is focused into the spectrometer using an electromagnetic quadrupole triplet set of magnets, Q1, Q2 and Q3 (with currents 5 A, 4 A, 5 A, respectively). The measurements were taken using the 40 TW laser operating with laser and plasma parameters outlined in table 4.1.

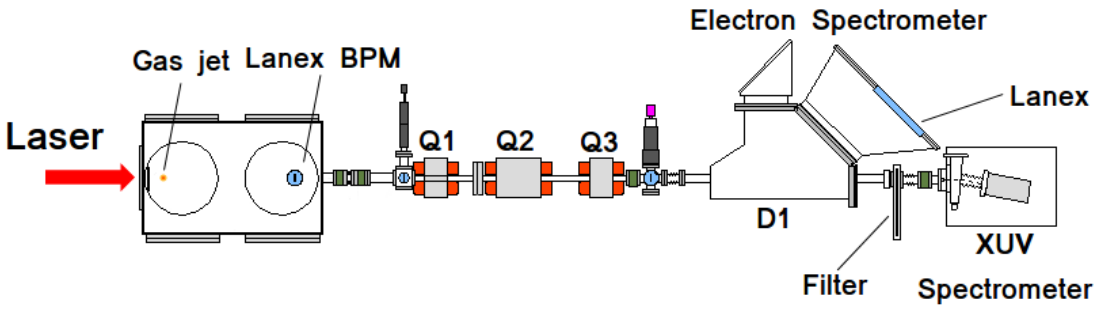

Figure 4.1: Schematic of the ALPHA-X beamline with McPherson spectrometer placed 3.88 m from the gas jet and metal filters placed ≈ 30 cm before the entrance slit of the spectrometer.

Laser energy (before compression)	1.5 J
Pulse duration	≈ 35 fs
Focus diameter ($1/e^2$)	≈ 50 µm
Gas backing pressure	50 bar
Laser height above of nozzle	4.0 mm
Plasma density	1.8×10^{19} cm^{-3}

Table 4.1: Laser and plasma parameters during acquisition of XUV spectral data.

4.1 Aluminium filter

An aluminium filter (obtained from Luxel Corporation [185] on a TF111 frame) with thickness 150 nm is used to measure spectra from ~ 2 nm to ~ 60 nm ($21 - 620$ eV), beyond which the transmission of the spectrometer diffraction grating is poor. As the filter is very fragile, due to its thickness, it is supported by a 70 lines per inch (lpi) nickel mesh. The mesh has pitch of 363 µm, a 30 µm bar width and $10 - 15$ µm thickness, which is consistent with an open area of 82%. This mesh is observable in both the spectral measurements, described in this chapter, and also in the spatial and coherence measurements, described in chapter 5. The correction for the filter transmission takes the mesh into account. When making a measurement, each component of the beamline contributes to the overall efficiency of the system. To correct for the total brightness of the source, the efficiency of the filter, Andor Newton camera and 600 lines mm^{-1} diffraction grating are taken into account, as shown in figure 4.2.

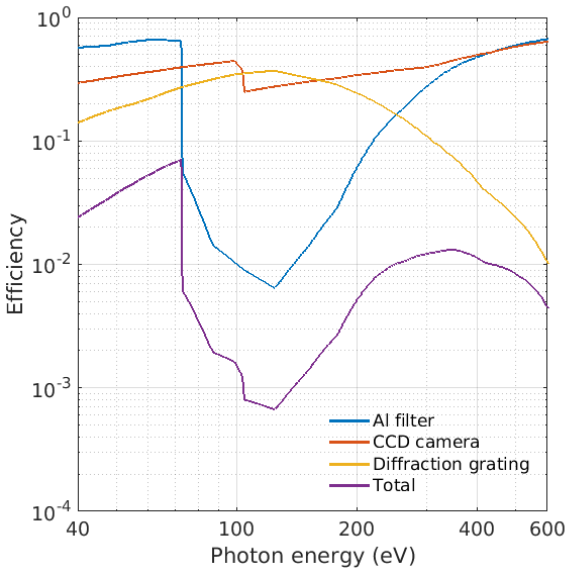

Figure 4.2: Efficiency of each of the components attenuating the signal on the spectrometer. The total efficiency of the beamline is shown in purple.

Images using the aluminium filter, as in figure 4.3, show that the radiation observed is part of a broad spectrum between 3 nm and 30 nm (40 to 400 eV). The filters only allow a narrow window of photon energies to be observed for a given laser shot. The XUV transmission through aluminium has two spectral "windows". The first is for radiation with wavelength longer than the aluminium L edge, occurring at 17 nm (73 eV). The second window of high transmission for aluminium is between 150 eV and 600 eV (2 nm and 8 nm). Not every laser shot produces XUV radiation. 4.4% of laser shots produce radiation at $\sim$ 59 eV and 1% produce radiation $\sim$ 206 eV. At the beginning of each data run, a single shot is recorded, with the laser off, as a background image. This is homogeneous across the whole area of the CCD and has an average value of 300 counts per pixel. Although radiation in the window with photon energies less than the aluminium L edge almost always peaks at 59 eV (21 nm), radiation in this transmission window extends to 41 eV (30 nm), after which the signal drops off. As the efficiency is high at these photon energies it can be concluded that there is a real tail in the XUV radiation spectrum. Data is collected over the course of several days during which time the number of photons fluctuates by three orders of magnitude around an

average and peak number of photons, in the solid angle defined by the spectrometer slit, of 8.60×10^6 and 1.70×10^8 photons (< 73 eV).

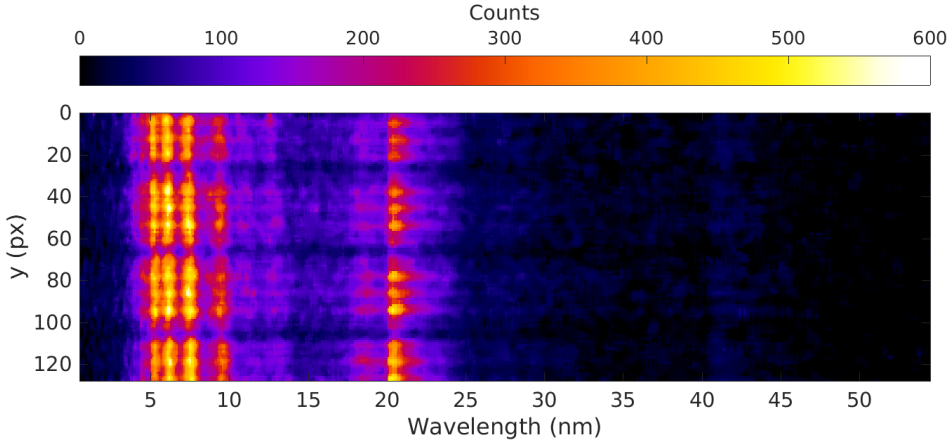

Figure 4.3: Full single shot raw spectral image measured with a 150 nm Al filter and McPherson spectrometer equipped with a 600 lines mm^{-1} diffraction grating with the entrance slit set to 100 µm. This shot shows XUV radiation at both the low energy (> 17 nm) and high energy (< 9 nm) side of the transmission dip of the filter.

The spectral brightness is estimated from the solid angle of the spectrometer entrance slit (1.0×10^{-7} sr 100 µm slit and 2.5×10^{-7} sr for slit width 250 µm). The measurement of the spectra are limited by the small area of the spectrometer entrance slit so an estimate of the total number of photons in the beam cannot be made. In the region beyond the aluminium L edge, corresponding to example spectra in figure 4.4, $(7.6 \pm 1.3) \times 10^{13}$ photons sr^{-1} are measured on average on the spectrometer, after correcting for the grating, CCD camera and filter efficiencies. This corresponds to an average peak brightness of (47.9 ± 6.7) µJ $\mathrm{eV}^{-1}\,\mathrm{sr}^{-1}$ occurring at (59.0 ± 0.2) eV. The best shot contained 1.7×10^{15} photons sr^{-1} with a peak brightness of 829 µJ $\mathrm{eV}^{-1}\,\mathrm{sr}^{-1}$.

Around half of shots in the range 35 eV to 73 eV contained a modulation in their spectra. In this case, two to four peaks can be observed as seen in figure 4.5 where the brightest of the peaks always occurs at 59 eV, the position of the brightest peak in the spectra occurs at the same photon energy in shots containing and not containing modulations. The average distance between peaks in spectra of this type is (6.9 ± 0.2) eV. When a shot exhibited several modulations, the spacing between them is

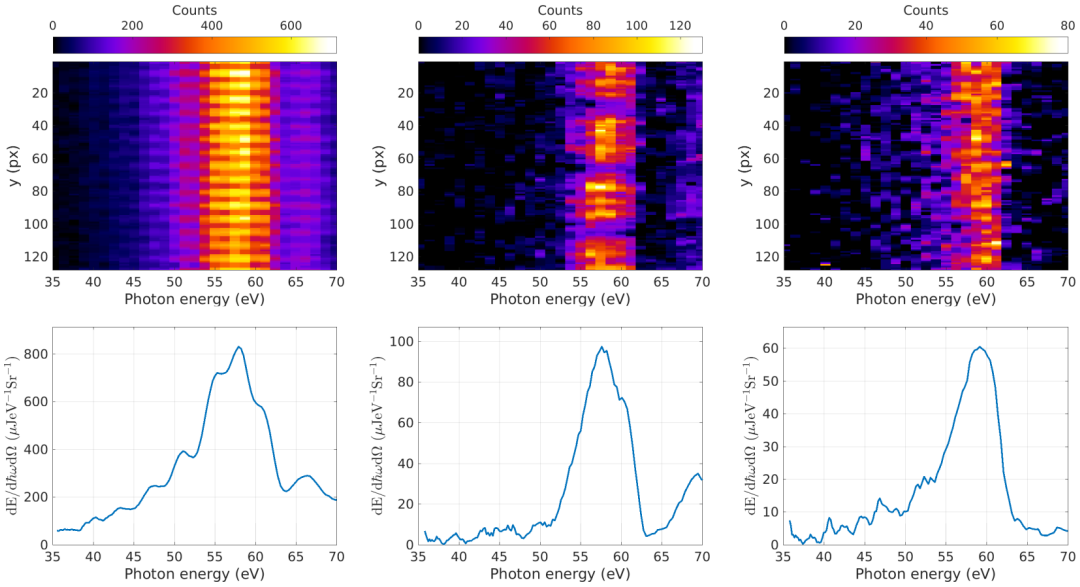

Figure 4.4: Typical corrected spectra, < 73 eV, recorded with a 150 nm Al filter and the McPherson spectrometer using the 600 lines mm^{-1} grating.

constant, although there is a small fluctuation between modulation spacing from shot to shot.

A radiation band is also observed at 29.5 eV (42 nm). However, comparison between the spectra at 59 eV and 29.5 eV show that these are not real spectra but a higher diffraction order from the grating, as shown in the examples in figure 4.6. The data with the photon energy peaking at 42 nm had each value of the photon energy halved to match the values at 21 nm so the structure of the spectra could be compared. The peak of the spectra from the first order is twice that of the second and the features in the spectra match so the signal observed at 29.5 eV is concluded to be the second order of the signal at 59 eV.

The increased transmission of the Al filter on the high photon energy side of the L edge allows radiation > 150 eV (< 8 nm) to be measured. Radiation is observed in this spectral region on 1% of laser shots, and peaks between 159 and 290 eV with an average of (223 ± 19) eV after correcting for filter transmission, CCD quantum efficiency and grating efficiency. Integrating this higher energy part of the XUV spectrum, between 150 and 450 eV, gives $(3.0 \pm 1.9) \times 10^{15}$ photons sr^{-1} and a peak brightness of $(678 \pm$

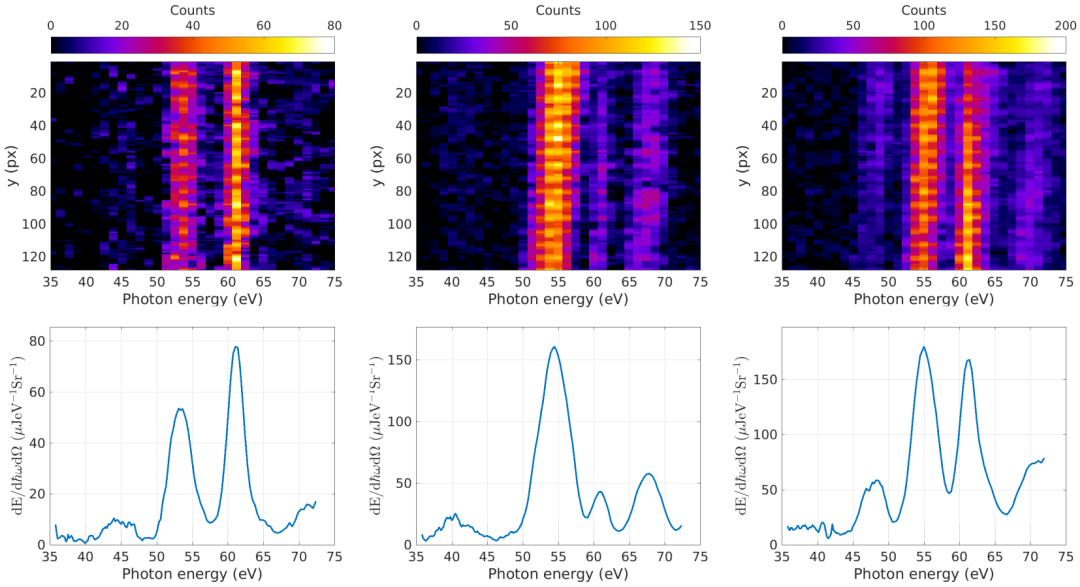

Figure 4.5: Typical spectra exhibiting modulations, < 73 eV, recorded with the 150 nm Al filter and the McPherson spectrometer using a 600 lines mm^{-1} grating. Line-out plots are corrected for the spectrometer grating, Al filter and CCD camera quantum efficiencies.

506) µJ eV^{-1} sr^{-1}. The best shot recorded produced 1.5×10^{16} photons sr^{-1}, consistent with a peak spectral brightness of 3.95 mJ eV^{-1} sr^{-1} at 166 eV. However, only 7 reliable shots were recorded in this region due to overlapping orders of the diffraction grating. Only shots where the first and second orders could be separated were considered in the analysis.

4.2 Zirconium filter

A 206 nm thick zirconium (Zr) filter is employed to investigate emission in the XUV region where the aluminium filter transmission is poor. It has high transmission between 73 and 207 eV ($6 - 19$ nm), as shown in figure 4.8, but, unlike the aluminium filter, it is not supported by a mesh.

For the analysis of the images recorded with the zirconium filter, a careful choice of background image had to be made due to the large amount of (800 nm) laser light leaking through the filter. The shot used as the background was chosen by first identi-

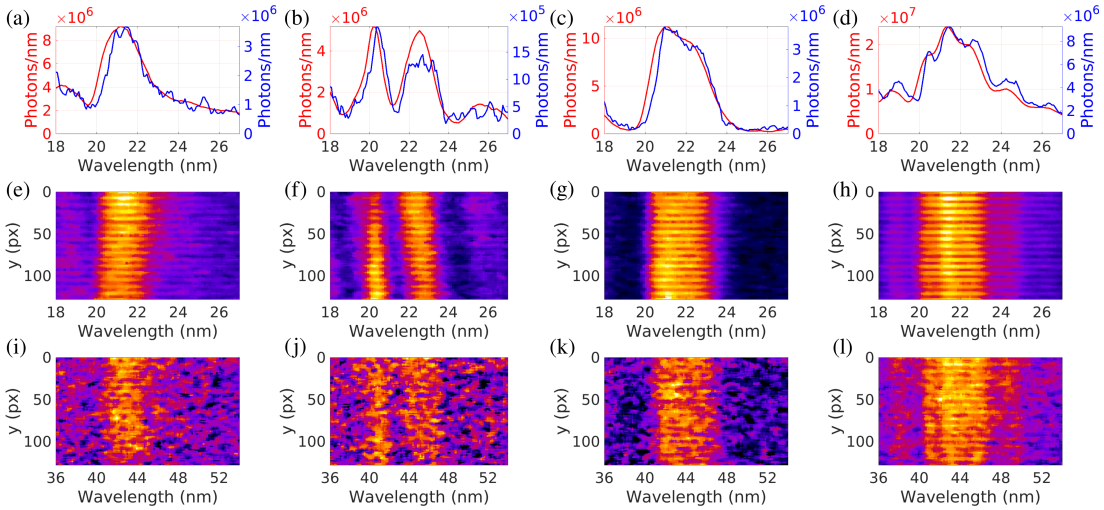

Figure 4.6: Comparison of spectral images at 21 and 42 nm (30 and 60 eV), corrected for the spectrometer grating, Al filter and CCD camera quantum efficiency. (a) - (d) Direct comparison of spectra of second order (blue line) and first order (red line) with wavelength halved to match the second order data. (e) - (h) Spectrometer signal at 21 nm. (i) - (l) Spectrometer signal at 42 nm.

fying all of the shots in a given run of laser shots which are blank, i.e. do not contain XUV radiation. The images are then cropped around the region where the Zr filter transmits XUV ($73 - 207$ eV). The shot which contains the average number counts is found and this image is taken to be the background. A typical raw image from the spectrometer before any processing or background subtraction is shown in figure 4.9.

A region of interest (ROI) between 60 and 200 eV is chosen to include all data except areas of the image where a significant signal due to background light is present. This ROI includes the whole range where the transmission of the zirconium filter is high. An average of $(1.1 \pm 0.30) \times 10^{15}$ photons sr^{-1} per shot is observed, with a maximum of 1.3×10^{16} photons sr^{-1}. The number of photons measured within the spectrometer solid angle gives an average peak brightness of (163 ± 32) µJ eV^{-1} sr^{-1} and a maximum of 1.25 mJ eV^{-1} sr^{-1}. Modulations in the spectra are observed in $> 90\%$ of shots, which can be divided in two distinct groups: the first includes spectra where a large number of peaks (up to 12) with a small spacing are observed. The second group comprises spectra with a small number of peaks (2 to 3) with larger spacing. In a typical shot

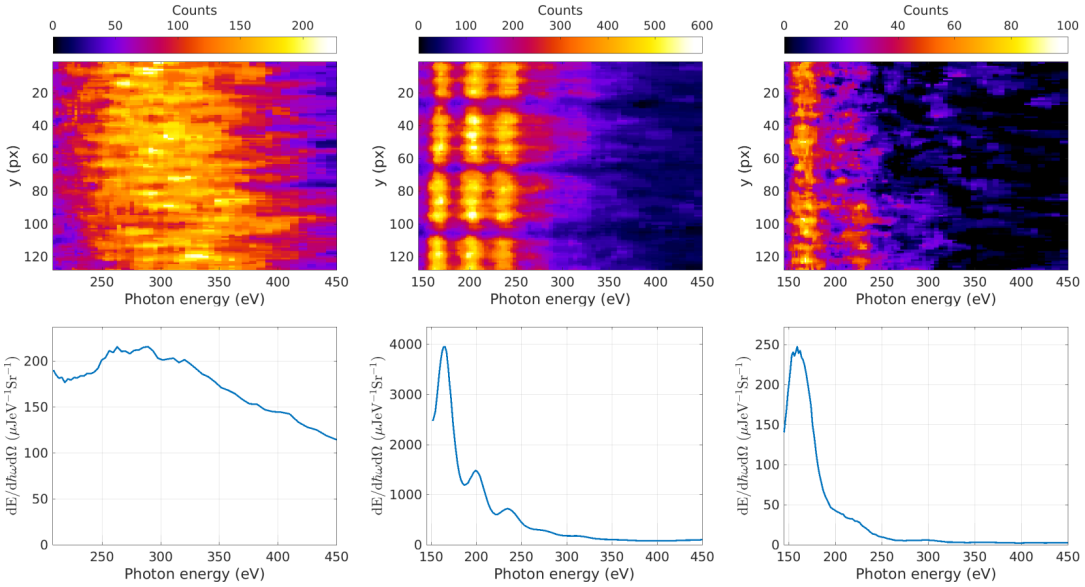

Figure 4.7: Typical spectra, > 155 eV, recorded with 150 nm Al filter and McPherson spectrometer using 600 lines mm^{-1}.

containing a small number of modulations, the spacing between them is large with an average value of (29.8 ± 2.6) eV.

In the case of a large number of modulations, 4 to 12 peaks in the spectra are observed. Their average spacing is (11.1 ± 0.5) eV and for a given shot, the peak spacing is constant. Representative examples of images of both cases of spectra are shown in figure 4.10 and figure 4.11.

4.3 Indium filter

Emission of high photon energy XUV radiation is investigated using an indium (In) filter, which has a region of high transmission between 110 and 600 eV (2 – 11 nm). The efficiency of the indium filter, camera quantum efficiency and grating are shown in figure 4.12. The indium filter is supported by a 70 lpi, 363 µm pitch nickel mesh, with 30 µm bar width and 10 – 15 µm thickness, similar to that of the aluminium filter.

The subtraction of the background signal is critical for the indium filter because of significant light leakage through pinholes in the filter. Particular care is taken in

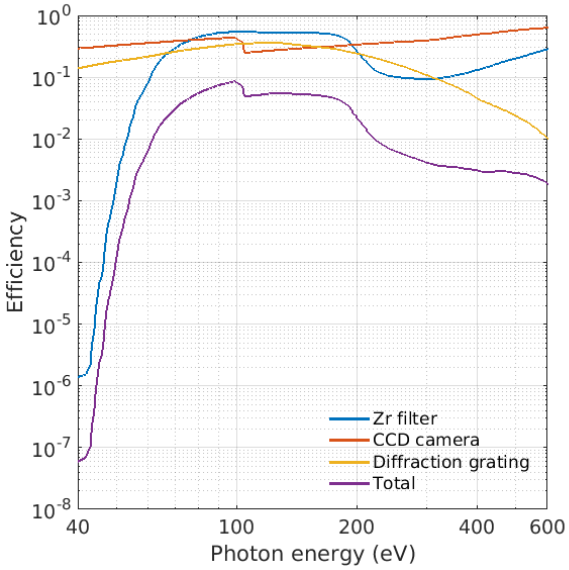

Figure 4.8: Efficiency of each of the components that attenuate the signal on the spectrometer. The total efficiency of the beamline is shown in purple.

choosing the background because the laser leakage and XUV radiation signals overlap. A typical image of an image is shown in figure 4.13 without the presence of XUV radiation. In blank shots that could be considered as candidates for the background image, the number of counts on the CCD camera varied from shot to shot with the intensity of the laser with a relative range of 65%. A background is selected, with the same method used for the Zr filter, by finding a shot that contains the average number of counts in the ROI where XUV radiation would be observed.

Laser shots where XUV radiation is observed using the indium filter are rare; only 12 shots of 1000 have a discernible XUV signal. An average of $(1.1 \pm 0.6) \times 10^{15}$ photons sr^{-1} are measured within the solid angle of the spectrometer, and maximum of 7.8×10^{15} photons sr^{-1} is measured. These measurements correspond to a mean and maximum brightness of (356 ± 176) $\mu\mathrm{J\,eV}^{-1}\,\mathrm{sr}^{-1}$ and 2.341 $\mathrm{mJ\,eV}^{-1}\,\mathrm{sr}^{-1}$, respectively. Representative shots with the indium filter are shown in figure 4.14.

However, modulations in the spectrum are sometimes observed using the indium filter, as shown in figure 4.15. The average spacing between the peaks is (11.6 ± 0.8) eV, similar to that of the Zr filter.

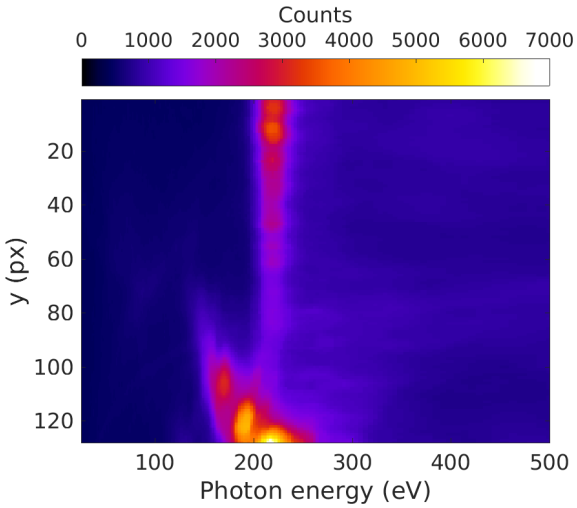

Figure 4.9: Raw image used for background subtraction, with zirconium filter and 600 lines mm^{-1} diffraction grating. Transmitted laser light from holes in the filter can be seen, which can reach several thousand counts per pixel.

4.4 Brightness distribution

Spectral measurements show that the XUV radiation from the plasma is broadband. The filters only define a limited window where the spectrum and brightness of the radiation can be investigated, for each segment. This is summarised in figure 4.16, where the maximum brightness from each shot in a segment is plotted. A betatron spectrum with a critical energy 2.7 keV, corresponding to the plasma density, measured electron energy and an estimated betatron amplitude of $r_\beta = 2.5$ µm, is superimposed on the data. This shows that the slope of the brightness distribution is not match to a simple synchrotron spectrum, which suggests that the emitted XUV radiation may not be related to betatron oscillations of electrons in the plasma bubble or other synchrotron processes. Three representative example spectra, one with each metal filter are plotted to show the distribution of the XUV radiation over the whole spectrum. The red curve shows the single shot distribution of the spectrum in the range 35 to 300 eV (4 to 35 nm), where the gap in the middle is the region where the filter poorly transmits XUV radiation so the correction is unreliable. The use of the zirconium and indium filters allow investigation of the spectral regions where aluminium does not transmit. The

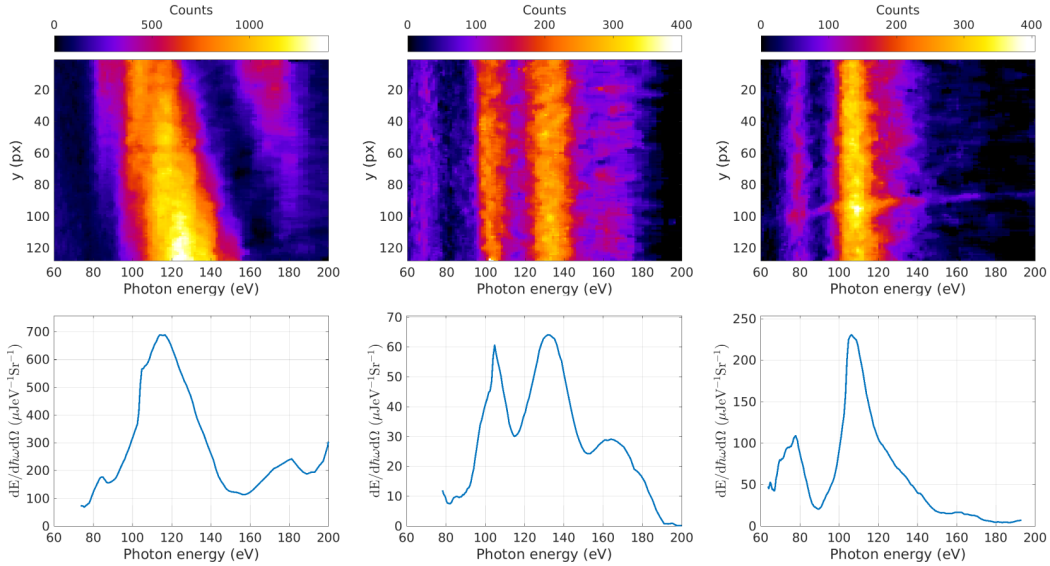

Figure 4.10: Examples of XUV spectra showing a small number of modulations with a large spacing recorded with zirconium filter and 600 lines mm^{-1}. The line-out plots have been corrected for filter transmission, CCD quantum efficiency and grating transmission.

efficiency of the detecting system is high for low energy photons to 30 eV so the tailing off of the radiation close to 50 eV is thought to be real however the efficiency of the grating at high energy > 400 eV is low, therefore, it cannot be concluded that the XUV radiation from the plasma does not extend beyond this range. Further experiments will be required with a diffraction grating optimised for high energy photons.

4.5 Discussion

Measurement of XUV radiation emitted from the plasma is challenging because of the presence of the high power laser beam propagating in the same direction as the XUV radiation. Therefore, band pass filters that transmit XUV radiation while blocking the laser beam are required. Three thin metal filters with relatively narrow transmission windows have been used for spectra measurements. These show that XUV radiation is emitted as a relatively broad continuous spectrum between 40 and 410 eV (3 to 31 nm). Furthermore, most spectra exhibit regular modulations or multi-peaked structures with

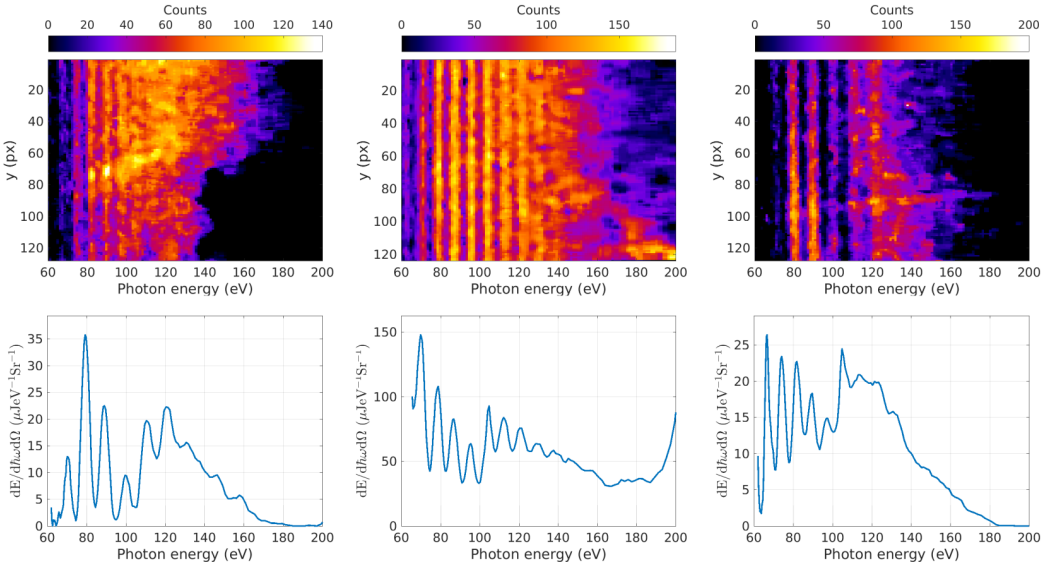

Figure 4.11: Examples of XUV spectra showing a large number of closely spaced modulations with a large spacing recorded with zirconium filter and 600 lines mm^{-1}. The line out plots have been corrected for the filter transmission, CCD quantum efficiency and grating transmission.

regular spacings. The spectra measured using the zirconium and indium filters partially overlap and exhibited similar modulations with peak separations of 11 eV, on average which can be seen in figure 4.17. However, the aluminium filter, which transmits lower energy photons, has an average modulation separation of 6.9 eV. Measurements using the zirconium filter, which has the widest transmission window, produced spectra with large shot-to-shot fluctuations in the number of modulations and peak separations from 4 eV to 60 eV, and also a second category of spectra with only 2 to 4 peaks and a larger peak separation of 29.8 eV, on average.

In the low energy transmission region of the aluminium filter, radiation is observed at both 21 and 42 nm (59 and 29 eV). Comparison of the detailed structure of the spectra showed that the spectra around 42 nm is just the second order of 21 nm from the diffraction grating. This realisation of overlapping first and second order spectra acted as a catalyst to carefully check all measured spectra to ensure that data is analysed correctly. Second order artefacts in the spectra were also identified in the spectra in high energy bandpass of the aluminium filter, which explains why high signals are

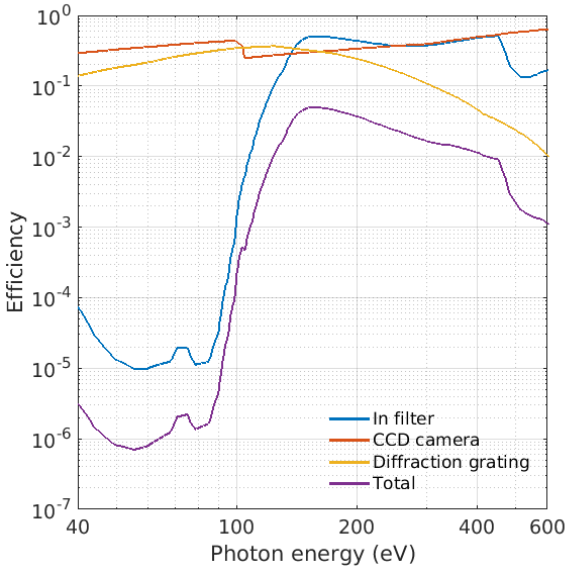

Figure 4.12: Efficiency of each of the components that attenuate the signal measured by the spectrometer when an indium filter is used. The total efficiency of the beamline is shown in purple.

occasionally observed in the spectral region where the transmission of the Al filter is low ($< 10^{-3}$), as can be seen in the full spectral example, figure 4.3.

Two key features of the XUV radiation are that the maximum number of photons measured can be very high, and also that there is a large shot-to-shot variation in measured photon number. The number of photons measured is defined by the size of the entrance slit of the spectrometer, increasing the slit width results in a larger total number of photons being measured. The total number of photons measured for example, using the Al filter is as high as 1.5×10^9 photons passing through the slit, or 1.5×10^{16} photons sr^{-1}, in the high energy transmission window between 150 and 450 eV. A summary of the average and maximum number of photons numbers and peak brightnesses is shown in tables and 4.2 and 4.3. However the measured number of photons fluctuates by three orders of magnitude. This results in large variations in the measured brightness using the Zr and Al filters. The variation with the In filter is much less than 10^3, but the high background signal due to filter damage prevents the detection of spectra with a low number of photons. This is a very general problem

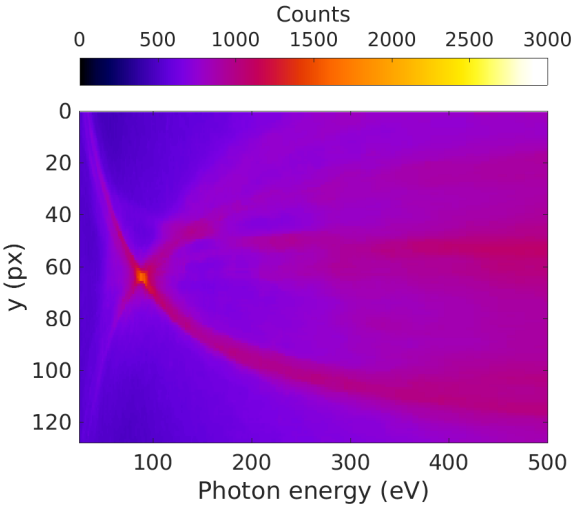

Figure 4.13: Unprocessed image recorded with indium filter and 600 lines mm^{-1} diffraction grating. Transmitted laser light from holes in the filter can be seen with a signal in excess of the signal due to XUV emission in some regions of the CCD sensor.

due the sensitivity of the detection system, which depends on a number of factors including: light leakage through the metal filters, filter transmission, grating efficient and detector quantum efficiency. The spectral bandwidth was found to be large with photons being emitted between 3 and 31 nm, assuming that the duration of the XUV pulse is limited by the spectral bandwidth, this corresponds to a 11 as XUV pulse making it an interesting source for time resolved imaging experiments.

Filter	**Number of photons** (photons sr^{-1})	**Peak brightness** ($\mu J\,eV^{-1}\,sr^{-1}$)
Al $(40-70$ eV)	7.59×10^{13}	47.9
Zr $(60-200$ eV)	1.11×10^{15}	162.7
In $(100-180$ eV)	1.09×10^{15}	356.1
Al $(155-450$ eV)	2.97×10^{15}	677.9

Table 4.2: Summary of the number of the average photons measured by the spectrometer and the associated peak brightness.

Statistics with the indium filter and high energy transmission region of the aluminium filter are poor, and therefore only around a dozen images in each case were suitable. Further experiments are required to gain a better understanding of the XUV radiation between 150 and 450 eV to extend the studies of the brightness distribution,

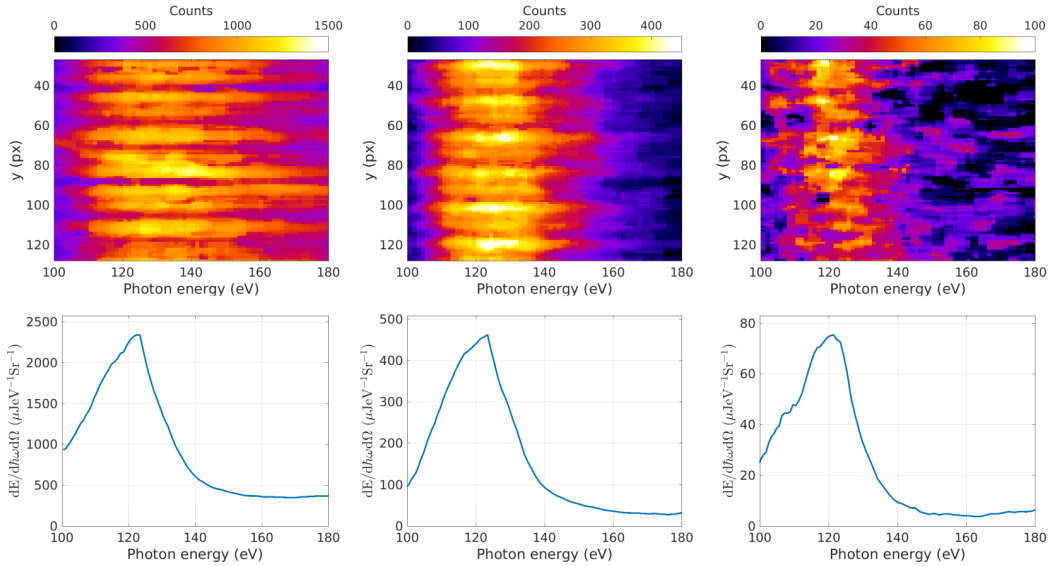

Figure 4.14: Examples of XUV spectra recorded with indium filter and 600 lines mm^{-1}. The line out plots have been corrected for the filter transmission, CCD quantum efficiency and grating transmission.

Filter	**Number of photons** (photons sr^{-1})	**Peak brightness** ($\mu J\, eV^{-1}\, sr^{-1}$)
Al ($40 - 70$ eV)	1.70×10^{15}	830
Zr ($60 - 200$ eV)	1.29×10^{16}	1251
In ($100 - 180$ eV)	7.76×10^{15}	2341
Al ($155 - 450$ eV)	1.52×10^{16}	3952

Table 4.3: Summary the maximum measured number of photons measured by the spectrometer and the associated peak brightness.

modulations and frequency of shots that produced detectable XUV radiation. For this purpose, a new grating has been obtained, which is blazed at 4 nm so is better optimised for short wavelength radiation. All damaged filters have also been replaced.

These results for the spectral brightness distribution, low shot rate (4.4% of laser shots resulted in the emission of XUV radiation) and modulation separation variation all suggest that the emission process is highly nonlinear and may help to identify the emission process in the future.

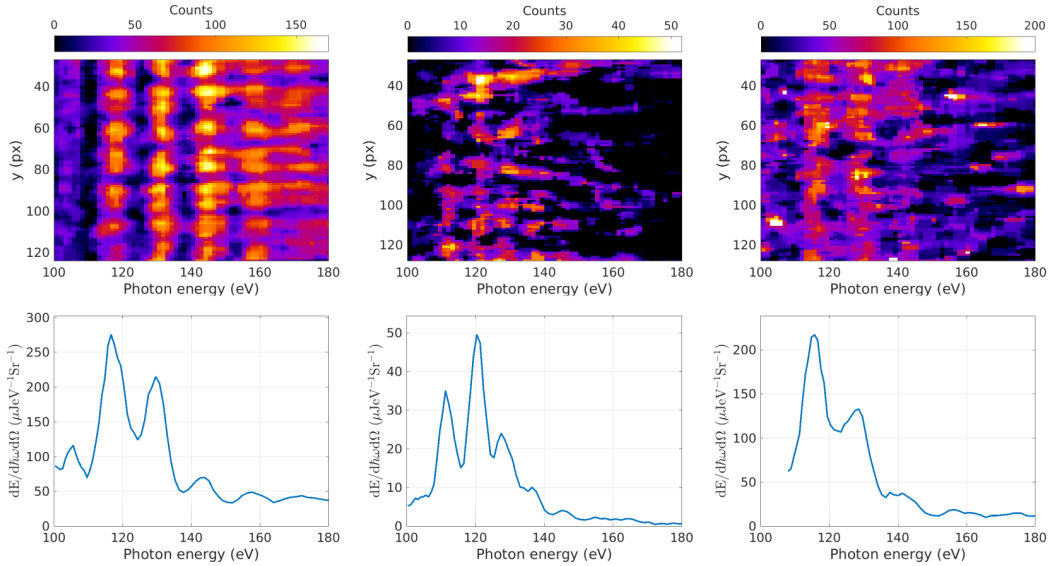

Figure 4.15: Examples of XUV spectra recorded with indium filter and 600 lines mm^{-1} showing the presence of modulations. The line-out plots have been corrected for the filter transmission, CCD quantum efficiency and grating transmission.

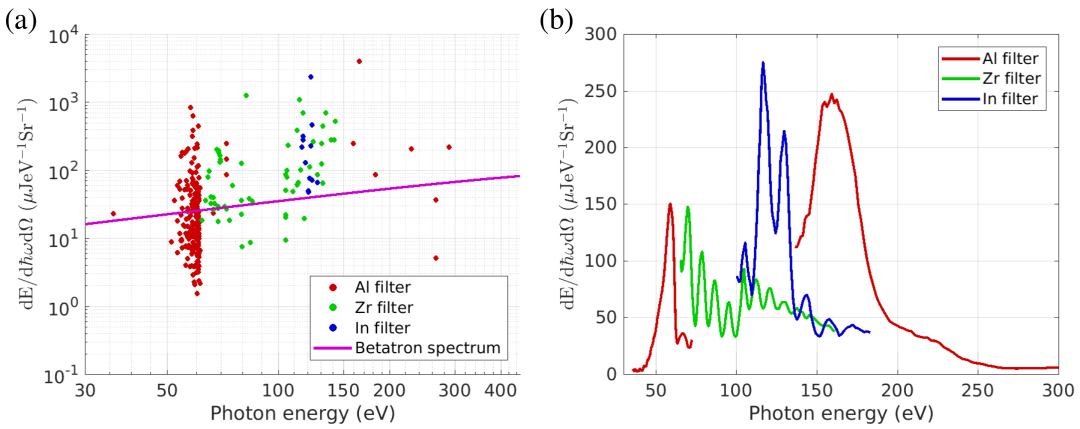

Figure 4.16: (a) Peak brightness for each shot measured by the McPherson 248/310 spectrometer in the transmission window of each of the metal filters and a betatron spectrum with critical energy of 2.7 keV, shown in purple. (b) Single shot example spectra measured with the aluminium filter (red), zirconium filter (green) and indium filter (blue).

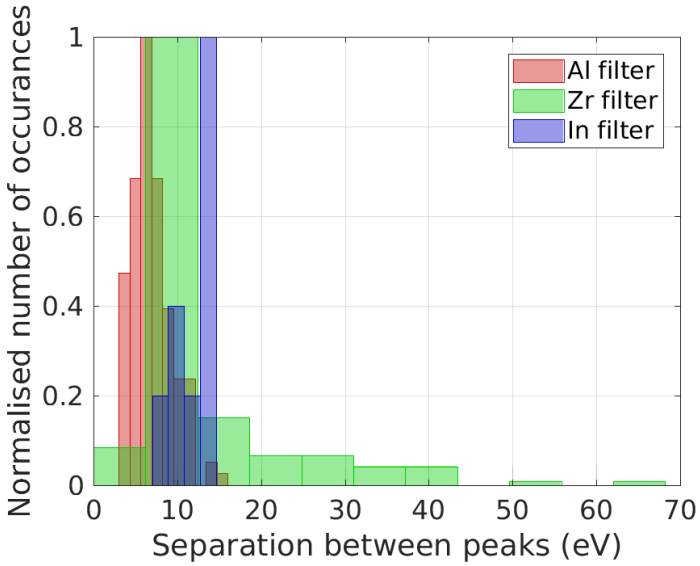

Figure 4.17: Normalised hisgrograms for the spacing between modulations in the XUV spectra for each of the three metal filters.

Chapter 5

Spatial and coherence measurements of XUV

In this chapter, measurements of the beam profile, divergence and transverse coherence of the extreme ultraviolet beam emitted from the plasma are presented where the data is used to estimate the source size and the peak brightness of the radiation. The transverse coherence of the radiation is measured across the entire spectrum where significant XUV radiation is emitted ($9 - 31$ nm) using a series of Youngs' double slits where several different slit separations are used to ensure that interference fringes can be resolved across the entire spectral range. The experimental set-up is shown in figure 5.1, with the positions of double slits used to measure the wavelength and coherence of the radiation are marked as DS1 and DS2. The camera is placed at two positions. The first is 3.88 m from the gas jet, which ensures that the interference fringes from the slits can be resolved during the coherence measurements where the Andor iKon-M camera described in chapter 3.3.3 is used. The second, closer, position of 1.56 m has been chosen to ensure a larger detection solid angle for profile measurements.

5.1 XUV beam profile

The profile of the XUV radiation is measured directly by placing the CCD camera after the beam-splitter and 1.56 m from the gas jet, which is configuration (b) in

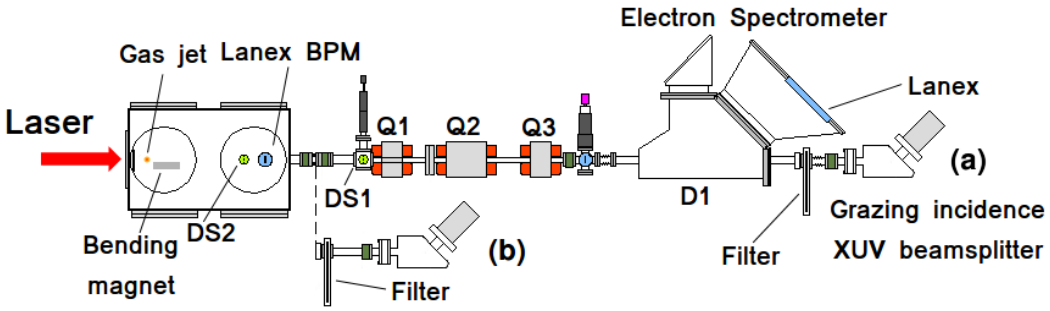

Figure 5.1: Experimental beamline as set up for the profile and coherence measurements. The grazing incidence beamsplitter is installed at two positions (a) 3.88 m from the gas jet, and (b) 1.56 m from the gas jet. The double slits are placed at DS1 and DS2, respectively for the two measurements.

figure 5.1, without any slits in position DS2. A 150 nm aluminium filter is used to block the laser beam. The combined transmission of the aluminium filter and beamsplitter efficiencies are shown in figure 5.2. The majority of signals recorded on the CCD camera are expected to be due to 21 nm (60 eV) radiation since the efficiency is two orders of magnitude lower for high energy photons between 150 and 450 eV. Unfortunately, their relatively higher transmission in the visible and infra-red spectral regions precludes measurements using the other metal filters.

Typical examples of the XUV beam profile measured with the CCD camera and aluminium filter blocking the laser are shown in figure 5.3 where the variation in beam diameter and pointing can be seen. The nickel mesh that supports the filter (described in section 4.1) is visible in each image. The size and divergence of the XUV beam is calculated using a three dimensional Gaussian least squares fitting script written in MATLAB which includes the ability of the fitted distribution to be at an angle relative to the x and y axes of the camera image which is left as a fitting parameter. The divergence is given by $\theta = tan^{-1}(d/L)$ where d is the width of the distribution from the fit multiplied by the 13 µm pixel size of the CCD camera and L is the distance from the gas jet to the CCD camera. The XUV beam is found to be elliptical, with an average full width half max (FWHM) major and minor divergences of (12.0 ± 1.0) mrad and (7.1 ± 0.4) mrad, respectively. The angle of the major axis of the beam relative

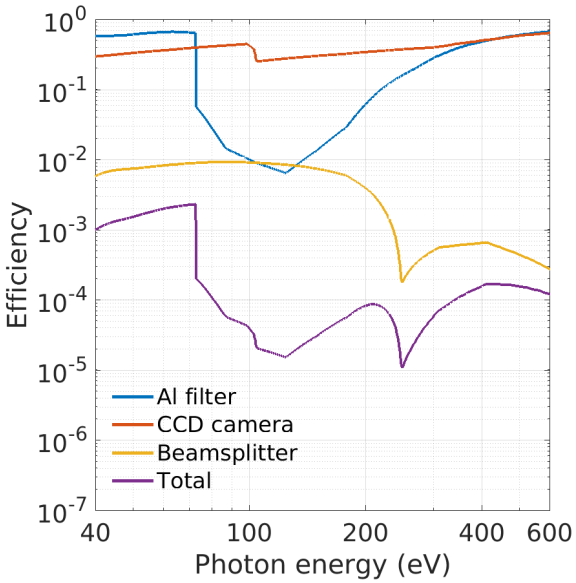

Figure 5.2: Efficiencies of aluminium filter, CCD camera and grazing incidence beamsplitter used for beam profile measurements. The total efficiency of the combination is shown in purple.

to the laser polarisation varied between 3° and 130° with an average of $(57 \pm 16)°$. However, convergence of the fitting routine failed on analysing many of the shots where the beam filled most of the area of the CCD sensor or where the centroid is far outside the CCD area, indicating that the actual divergence is larger for most of the shots. Furthermore, it is observed that the XUV beam has poor pointing stability, > 8 mrad, and the beam regularly points outside the acceptance angle of the CCD camera, and often only the tail of the beam is observed. In these cases the beam width from the fit becomes unreliable, which is why they have been omitted from the average value.

With the CCD camera placed in position (a) in figure 5.1, the integrated signal on the CCD camera can be used to estimate the brightness of the XUV radiation. The solid angle of the CCD camera at 3.88 m from the gas jet is 5.75×10^{-8} sr, which gives an average brightness over 285 laser shots containing XUV radiation of $(1.03 \pm 0.13) \times 10^{14}$ photons sr^{-1} per shot, with a maximum value observed of 2.7×10^{15} photons sr^{-1}. This compares well with the average value calculated from the McPherson spectrometer measurements using the 600 lines mm^{-1} diffraction grating and aluminium filter for

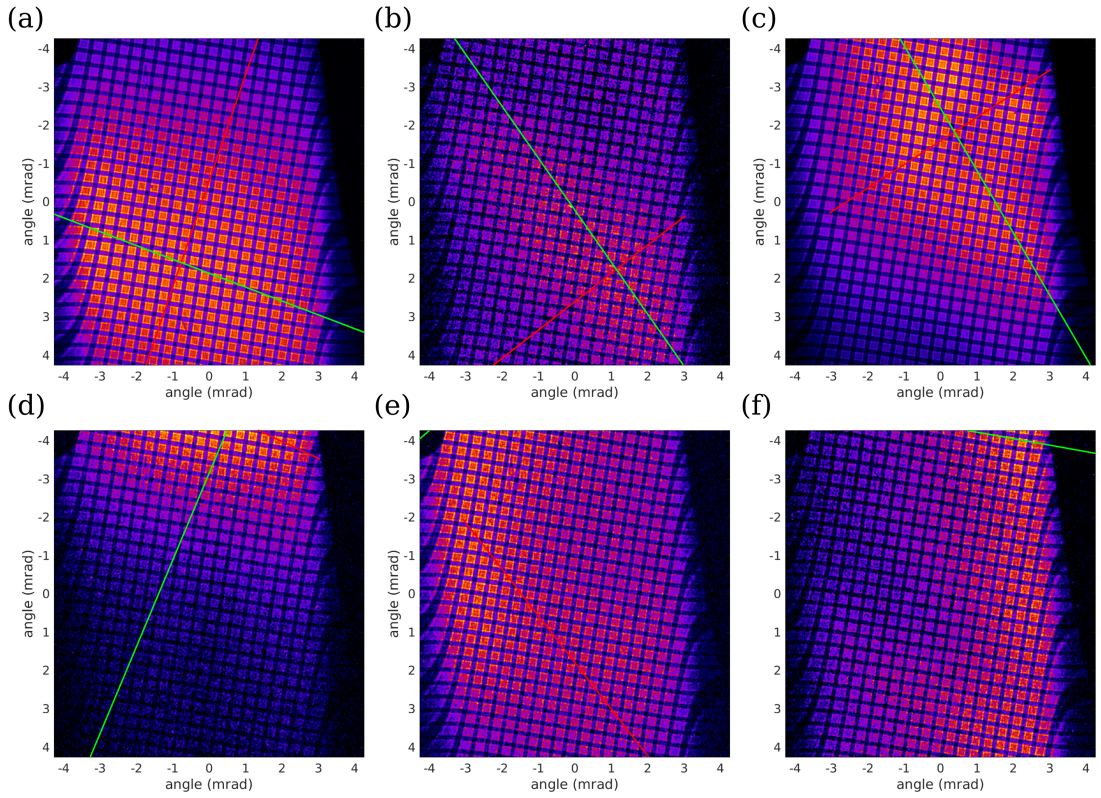

Figure 5.3: Typical images recorded with grazing angle beam-splitter of the profile of the XUV beam with the aluminium filter blocking the laser. (a) - (c) Images where three dimensional fit converged to solution. (d) - (f) Images where peak of beam fell outside the area of the CCD camera and fit did not converge to solution. The nickel mesh grid that supports the Al filter is clearly visible.

photon energies < 73 eV, which gave $(7.6 \pm 1.3) \times 10^{13}$ photons sr^{-1} with maximum measured value of 1.7×10^{15} photons sr^{-1}. At this distance from the gas jet, the XUV beam is uniform over the CCD.

5.2 XUV Coherence

5.2.1 Double slit interference

A radiation source is coherent if all the emitted photons of the same wavelength have a constant phase relationship between them. It is characterised by the correlation between wave-fronts separated by either space (transverse coherence) or time (longitu-

dinal coherence). The coherence of a beam of light can give rise to interference effects, which are important for many applications of the source, notably, the recent observation of gravitational waves using a Michelson interferometer [186], and also other interferometry measurements, for example, plasma density measurements of a gas jet in laser wakefield experiments [187]. However, it also has an important role in imaging applications such as phase contrast imaging [53, 188] and holography [189–191]. One of the first experiments to probe the coherence of light was performed by Young in 1802 [192] to demonstrate the wave nature of light, by reflecting white light off two closely spaced reflecting surfaces with the second surface depressed slightly below the plane of the first, in contrast to the two slits machined in opaque material used in this thesis. Electromagnetic waves from a monochromatic point source are directed towards a screen through two closely spaced (rectangular) apertures with width a and slit separation d. Huygens principle says that light passing through each of the two slits can be thought of as two sources of spherical waves that diverge as they propagate from the slits towards a screen placed a distance L from the slits, as shown in figure 5.4. For coherent sources, the waves from the two slits interfere with each other and sum together to give four times the intensity (constructive interference). When two waves are π radians out of phase they will sum together to give zero intensity (destructive interference). Whether there is constructive or destructive interference at a given position on the CCD camera depends upon the difference in the paths from the two slits to a point on the CCD.

Assuming that the light reaching the double slit are monochromatic plane waves, the electric field of a spherical wavelet of infinitesimal size (ds) is given by [193]

$$dE_p = \left(\frac{E_L ds}{L}\right) \exp(i(kL - \omega t)) \exp(iks\sin(\theta)). \tag{5.1}$$

The total electric field at point P on the CCD sensor can be found by integrating dE_p over both slits relative to the centre point between them. The choice of integrand limits in this case are shown in figure 5.5.

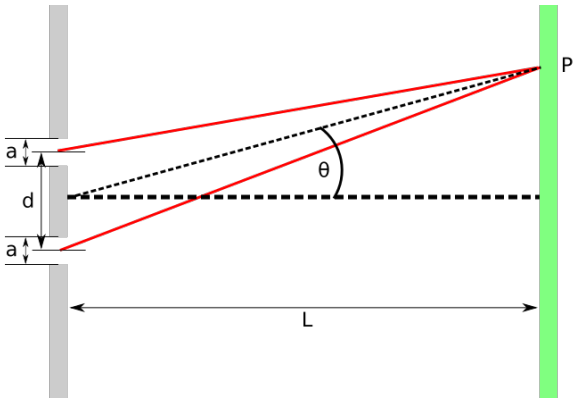

Figure 5.4: Simple sketch of double slit experiment. Double slit with slit width a and separation d is placed a distance L from a CCD camera. The line from point P on the CDD to the centre of the double slits subtends an angle of θ.

$$E_p = \left(\frac{E_L}{L}\right)\exp(i(kL-\omega t))\int_{(-1/2)(d+a)}^{(-1/2)(d-a)}\exp(iks\sin(\theta))ds + \left(\frac{E_L}{L}\right)\exp(i(kL-\omega t))\int_{(1/2)(d-a)}^{(1/2)(d+a)}\exp(iks\sin(\theta))ds. \tag{5.2}$$

By performing the integration, employing Euler's equation to remove exponential terms and introducing the identities $\alpha = kd\sin(\theta)/2$ and $\beta = ka\sin(\theta)/2$, the full electric field at point P can be expressed as

$$E_p = \left(\frac{E_L}{L}\right)\exp(i(kL-\omega t))\cos(\alpha)\frac{2a\sin(\beta)}{\beta}. \tag{5.3}$$

In the experiment, only the intensity of the light is measured by the CCD camera. The intensity is proportional to the amplitude of the electric field squared ($I = (\epsilon_0 c/2)\,E_0^2$). The maximum amplitude of the electric field occurs when the exponential term in equation 5.3 is unity ($kL = \omega t$) giving

$$E_0 = \left(\frac{E_L}{L}\right)\cos(\alpha)\frac{2a\sin(\beta)}{\beta}. \tag{5.4}$$

Therefore, the intensity distribution measured by a CCD camera is given by

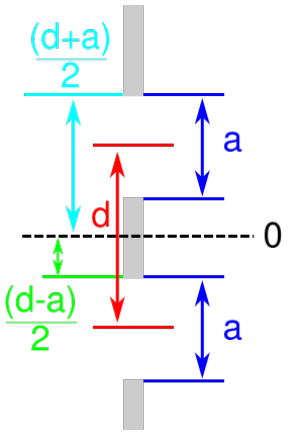

Figure 5.5: Double slit configuration with slit width, a and separation d. Coordinates of slit edges used for integrating over both slits relative to the centre point between them (marked as 0).

$$\begin{aligned} I &= I_0 \cos^2(\alpha) \left(\frac{\sin(\beta)}{\beta}\right)^2 \\ &= I_0 \cos^2(\alpha)\, \mathrm{sinc}^2(\beta)), \end{aligned} \tag{5.5}$$

where $I_0 = 2\epsilon_0 c \left(E_L a/L\right)^2$ is the peak intensity of the interference pattern and $\mathrm{sinc}(x) = \sin(x)/x$. An example of an interference pattern is shown in figure 5.6, calculated using parameters matching the experiments for 14 nm radiation (corresponding to the zirconium filter). The double slit is placed 2.84 m from the CCD camera, and has a slit width 30 µm and slit separation 150 µm. The overall angular distribution of the fringe pattern has a $\mathrm{sinc}(x)$ shape, which is the Fourier transform of a single rectangular slit, which just represents the diffraction pattern and determines the width of the envelope of the fringes. The slit separation determines the spacing of the interference fringes, also by the Fourier theorem.

The fringe visibility is found by calculating the contrast between the maximum and minimum intensity of an interference pattern and is defined as

$$V = \frac{I_{max} - I_{min}}{I_{max} + I_{min}} = g^{(1)}(\tau). \tag{5.6}$$

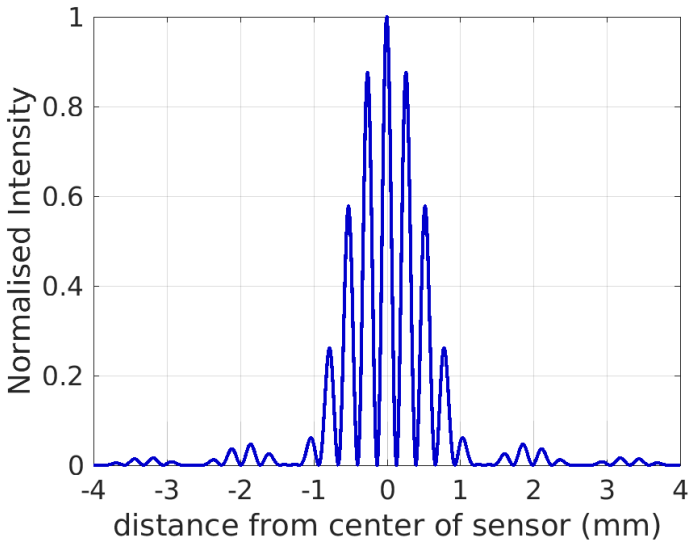

Figure 5.6: Example interference pattern obtained by solving equation 5.5 for 14 nm light, with the double slit 2.84 m from the CCD camera. The double slit has slit width of 30 µm and slit separation 150 µm. All parameters are chosen to match the experimental parameters.

The visibility of the fringes is a direct measure of the degree of coherence ($g^{(1)}(\tau)$) for a quasi-monochromatic source, that is, if the bandwidth of the power spectrum is small compared with the mean frequency ($\Delta\nu/\bar{\nu} \ll 1$). A check of this condition can be made with the measurements of the radiation from the spectrometer presented in chapter 4, where the condition of quasi-monochromaticity is met for the aluminium and indium filters, but in the case of the zirconium filter, $\Delta\nu/\bar{\nu} \approx 1$. In the case of a monochromatic plane wave, the beam is fully coherent so the fringe visibility is therefore $V = 1$, since no signal at all in the minima of the fringes, which can be seen in figure 5.6.

5.2.2 Interference from unequally illuminated sources

The expression given in equation 5.5 assumes that the intensity of the light at each of the slits is equal however for a light beam with a radial intensity profile, this may not be the case particularly if the beam size is similar to the slit separation. The effect of unequal illumination of a double slit was investigated by solving the intermediate step between between equations 5.2 and 5.3 where the integral has been preformed

but before Euler's identity was used to collect the exponential terms together, which is shown in equation 5.7. This gives the total electric field at a given point on the CCD camera that can then be used to calculate the intensity at that point, similar to the equal illumination case in chapter 5.2.1.

$$\begin{aligned} E_p = &\left(\frac{E_{L1}}{L}\right) e^{i(kL-\omega t)} \frac{a}{2i\beta} \left[e^{i\alpha}\left(e^{i\beta} - e^{-i\beta}\right)\right] \\ &+ \left(\frac{E_{L2}}{L}\right) e^{i(kL-\omega t)} \frac{a}{2i\beta} \left[e^{-i\alpha}\left(e^{i\beta} - e^{-i\beta}\right)\right] \end{aligned} \tag{5.7}$$

The ratio of the intensity between the slits can be chosen by choosing different values of E_{L1} and E_{L2}. An example of an interference pattern is shown in figure 5.7(a) using the same parameters as figure 5.6 with intensity ratio between the slits of $E_{L1}^2/E_{L2}^2 = 0.2$. In the case where $E_{L1}^2/E_{L2}^2 = 1.0$, the same interference pattern as figure 5.6 is obtained and when $E_{L1}^2/E_{L2}^2 = 0$, the single slit interference pattern is obtained. Figure 5.7(b) shows how the visibility of the fringes, where the central maxima and first minima are always used, varies as a function of the ratio of intensity between the two slits.

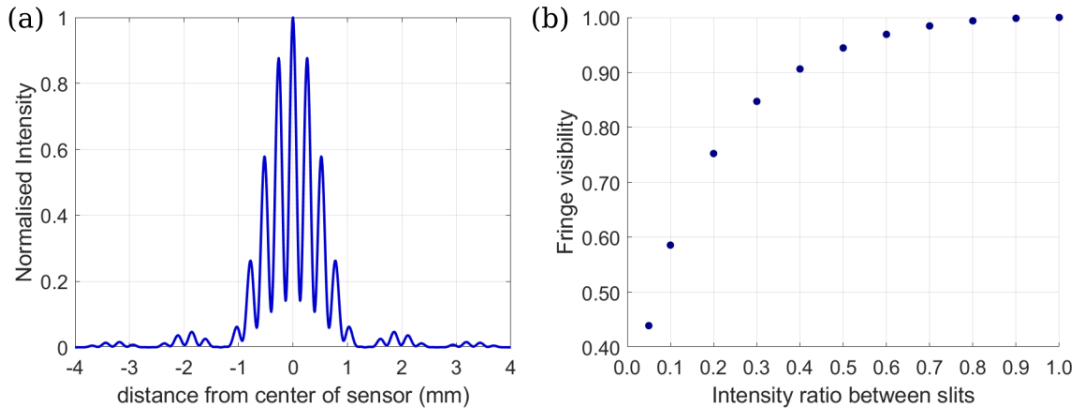

Figure 5.7: (a) Example interference pattern obtained by solving equation 5.7 for 14 nm light, with the double slit 2.84 m from the CCD camera. The double slit has slit width of 30 µm and slit separation 150 µm. The intensity ratio between the slits is $E_{L1}^2/E_{L2}^2 = 0.2$. (b) Calculated fringe visibility as a function of the intensity ratio bewtween the two slits.

From the results in chapter 5.1, it is known that the divergence of the XUV beam is high such that at the position of the double slits 1.04 m from the gas jet, the beam size is 12.5×7.4 mm^2. The comparison of the beam size using the minor axis divergence and width of the slits of largest separation (250 µm) used is shown in figure 5.8 to give a worst case scenario for the effects of unequal illumination. In the case where the the centre of the beam is positioned at one of the slits (figure 5.8(a)), the intensity ratio between them is greater than 0.99 giving a fringe visibility of one. If the pointing stability of the beam is poor such that the centre of the XUV beam is 5 mm from the centre point between the slits (figure 5.8(b)), the intensity ratio between them is 0.87, which still gives a fringe visibility greater than 99%. Since the illumination ratio between the slits is always high for the XUV beam about one meter from the source when considering any of the double slits available for the experiment, it can therefore be concluded that unequal slit illumination is not a major factor affecting the experimentally measured fringe visibility. If the divergence of the beam was smaller or the slits closer to the source then unequal illumination would have a larger impact on the visibility of the interference fringes.

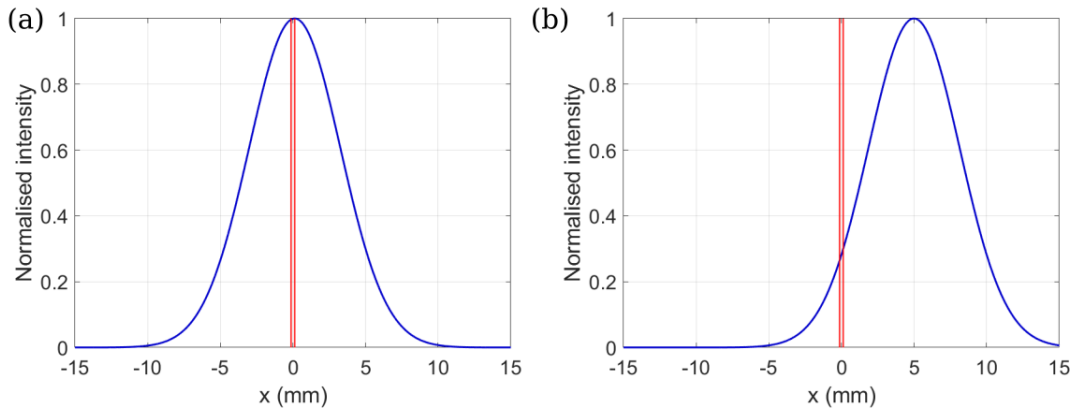

Figure 5.8: Calculated XUV beam profile in minor axis at DS1 on figure 5.1, 1.04 m from the gas jet with the position of double slits of separation of 250 µm marked in red. (a) beam centered on one slit. (b) beam centered 5 mm from centre point between slits.

5.2.3 Interference from non-monochromatic sources

In the example shown in figure 5.6, the fringe pattern has zero intensity points where destructive interference occurs, because the waves are monochromatic. However, in reality this is not the case. A simple model has been constructed to reproduce the experimentally measured interference patterns, by including the effects of broadband (polychromatic) light similar to the spectra presented in chapter 4. The polychromatic model integrates the fields over the range of wavelengths matching that of each filter, which is determined from measurements using the XUV spectrometer, where equal weighting is given to each wavelength component, as a first approximation. The electric field on the CCD camera is calculated using equation 5.4, where the complex electric field for each wavelength component is summed before calculating the intensity distribution on the CCD camera.

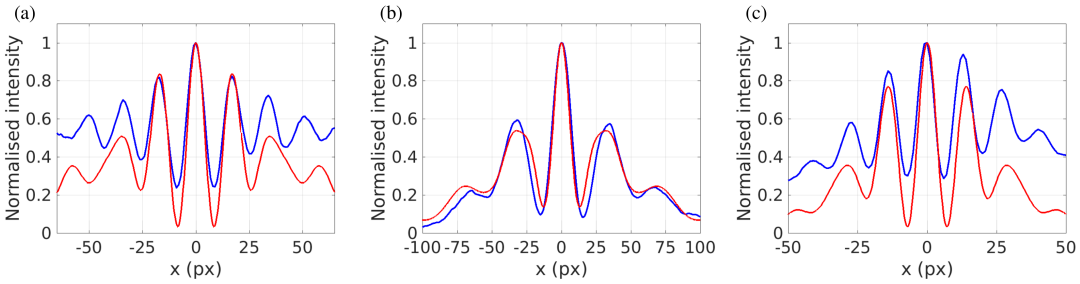

Figure 5.9: Comparison of simple model for polychromatic light passing through double slit with experimental measurement of the interference pattern for Andor CCD camera with 13 µm pixel size, 2.84 m from the double slit. Blue line is an experimentally obtained fringe pattern and red is calculated using the method described in the text for polychromatic light. (a) 250 µm slit separation with wavelengths between 16 and 24 nm, equivalent to the aluminium filter. (b) 90 µm slit separation with wavelengths between 7 and 12 nm, equivalent to the zirconium filter. (c) 150 µm slit separation with wavelengths between 8 and 12 nm, equivalent to the indium filter.

Figure 5.9 shows an example of an interference pattern calculated for each double slit used during the experiment, and for each filter material. It can be seen that the shape of the interference pattern can be reconstructed using this simple model. However, the model usually predicts a much higher fringe visibility than observed experimentally. These calculations show that the bandwidth alone is insufficient to account for the fringe

visibility therefore the source is not point like. These calculations can be improved by taking into account the wavefront distribution of the radiation at the double slits rather than assuming a plane wave and homogeneously illuminated slits.

5.2.4 Interference from non-point sources

The degree of coherence can be used to estimate the source size of the XUV radiation, according to the van Cittert-Zernike theorem [7, 194, 195], if an assumption about the geometry of the source is made. The van Cittert-Zernike theorem defines the visibility function which gives the visibility of interference fringes as a function of the source size and distance between the slits which is given by

$$\mu(\overrightarrow{B}) = \frac{\int I(\overrightarrow{\acute{\alpha}}) e^{-ik\overrightarrow{\acute{\alpha}}\cdot\overrightarrow{B}} d\overrightarrow{\acute{\alpha}}}{\int I(\acute{\alpha}) d\acute{\alpha}}, \tag{5.8}$$

where $\mu(\overrightarrow{B})$ is the fringe visibility, k the radiation wavenumber, $\acute{\alpha}$ the angular position of a point on the source, $\overrightarrow{B}$ is the vector corresponding to the distance between the slits and $\int I(\acute{\alpha}) d\acute{\alpha}$ is the integral over the source intensity. The absolute value of the visibility function is equal to the fringe visibility.

For an example of a circular source of uniform brightness across its whole area, with angular diameter $\acute{\alpha_0}$, the intensity distribution is given by a circ function (a two dimensional top hat function) which can be expressed as $I(\acute{\alpha}) = (\pi(\acute{\alpha}/2)^2)^{-1} circ(\acute{\alpha}/(\acute{\alpha}/2))$. The visibility function can then be calculated to be

$$\begin{aligned} \mu(\overrightarrow{B}) &= \frac{1}{\pi(\acute{\alpha}/2)^2} \int \left(\frac{\acute{\alpha}}{\acute{\alpha_0}/2} \right) e^{-ik_0\overrightarrow{\acute{\alpha}}\cdot\overrightarrow{B}} d\overrightarrow{\acute{\alpha}} \\ &= 2\frac{J_1(k_0 d\acute{\alpha}/2)}{(k_0 d\acute{\alpha}/2)}. \end{aligned} \tag{5.9}$$

This can be rewritten in terms of the slit separation, d, radiation wavelength, $\lambda = 2\pi/k_0$, source size diameter, s, and distance from the double slit to the screen, L, which gives

$$\left|\mu(\overrightarrow{B})\right| = V = \left| \frac{2J_1\left(\pi ds/(\lambda L)\right)}{\pi ds/(\lambda L)} \right|. \tag{5.10}$$

Here, the angle subtended by the size of the source at the distance to the double slits is rewritten as $\acute{\alpha} = \tan^{-1}(s/L) \approx s/L$, where a small angle approximation is made.

Figure 5.10 shows how the fringe visibility varies with source size diameter and slit separation for four possible source shapes found by solving equation 5.8 for their respective geometries. A circular source, a Gaussian distribution defined to $1/e^2$ diameter, two point sources and a ring with thickness 1 µm.

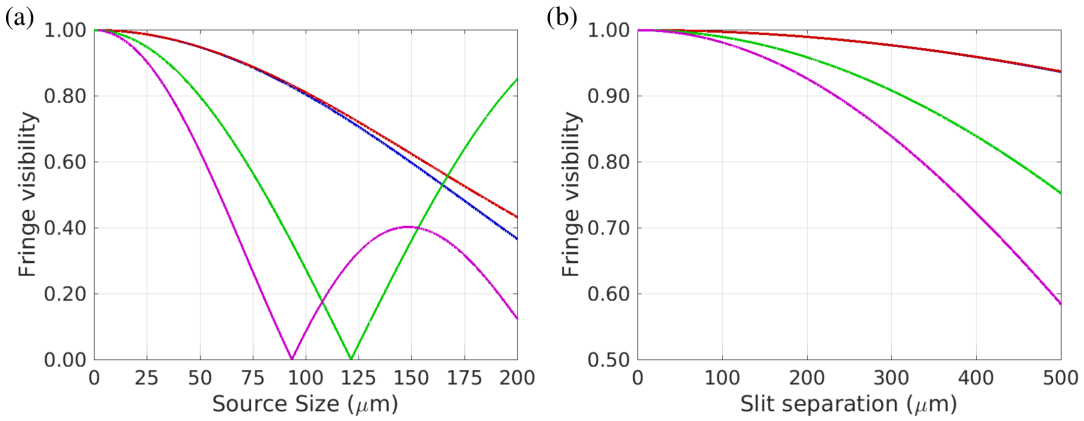

Figure 5.10: Solution to equation 5.8 for XUV radiation passing through a double slit with source geometeries of circular (blue), Gaussian (red), two point sources (green) and a ring of thickness 1 µm (magenta). (a) Fringe visibility for varying source size diameter with slit separation 90 µm. (b) Fringe visibility for constant source size diameter of 10 µm. In each case, the radiation wavelength is 21 nm and the double slit placed $L = 1.04$ m from the gas jet.

The parameters were chosen match the experiment when using the aluminium filter with, 21 nm XUV radiation with a double slit separation of 90 µm where the slits positioned 1.04 m from the gas jet (double slit 1 in table 5.1 and the CCD camera placed position (a) in figure 5.1). The ring thickness of 1 µm was chosen to be thin as an example, as the thickness (defined as the difference between outer and inner radius) of the ring increases the visibility gets closer to that of the circular source until the inner radius is zero which is the same as a circular source. For the ranges of radiation wavelength and slit separations in the experiment, the circular and Gaussian source give identical values for the fringe visibility and therefore the source size. All calculations have been made assuming that the source is circular however future experiments to

image the source, for instance with the Kirkpatrick-Baez microscope (see chapter 6), may require this assumption to be updated in the future. The source geometry could also be determined by making measurements of the fringe visibility for a series of slits with varying slit separation and comparing the results to each of the models.

5.3 XUV coherence measurements

The double slits used in the experiemnt are machined in 250 µm thick tungsten sheets, using an in-house laser micro-machining technique [51, 87]. Three double slits are used, each with different slit separations and widths optimised for a different wavelengths and are summarised in table 5.1. The slit separation is taken as the distance from the centre of one slit to the centre of the neighbouring slit, while the slit width is defined by the edge-to-edge distance of a single slit.

Double slit	**Slit separation** (µm)	**Slit width** (µm)	**Slit length** (cm)
1	90	18	1.5
2	150	30	1.0
3	250	30	1.0

Table 5.1: Summary of the sizes of the three double slits used to measure the coherence of the XUV radiation.

Microscope images of each of the double slits shown in figure 5.11 correspond to the parameters in table 5.1. The slits are micro-machined from one side only, and are wider on the machined side than the non-machined side. As XUV light in the range $3-31$ nm is strongly absorbed by tungsten, even by a few microns of material, the slit width is taken as the width of the narrower (non-machined) side facing away from the laser. For example, the transmission of 1 µm thick tungsten is 10^{-16} at 10 nm. The microscope images also show the imperfections in the manufacturing process, the edges of the slits are not straight and their widths are unequal and not constant along their length.

In configuration (a) of figure 5.1, the gas jet is 3.88 m from the CCD camera and 1.04 m from the double slit (DS1), which is 2.84 m from the CCD camera. The aluminium, zirconium or indium filter is placed just in front of the grazing angle beam-

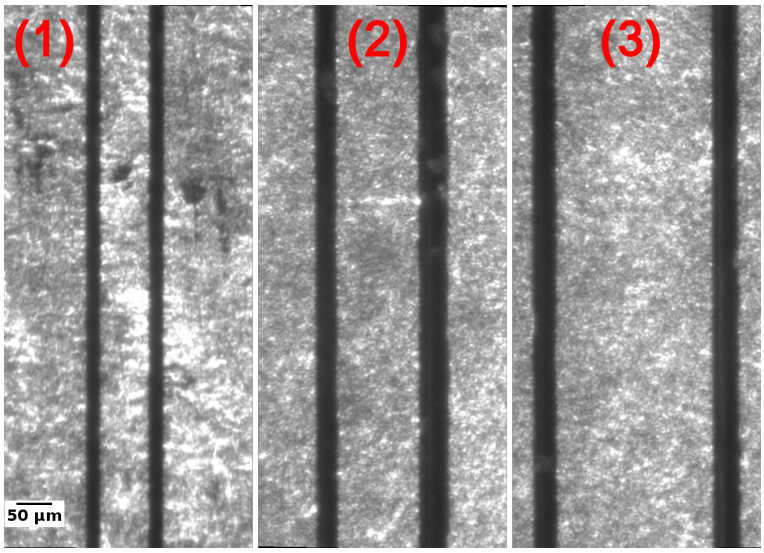

Figure 5.11: Microscope images showing the narrower side of each double slit used in the experiment. The double slit number (red) corresponds to the parameters in table 5.1. The scale bar on double slit 1 applies to all three images.

splitter to prevent 800 nm laser light from reaching the camera. Because the double slits lie in between the gas jet and the electromagnet for the spectrometer (D1), it is not possible to measure the electron charge concurrently with the interference patterns. However, the electromagnet of the spectrometer remained switched on to ensure that no high energy electrons reach the CCD camera during these experiments.

During data collection with the double slits, the same laser and plasma parameters as the spectral measurements are used, these are summarised in table 4.1. The 40 TW laser is focused 4 mm above the helium gas jet that operates at 50 bar backing pressure. The measurements are carried using the Andor iKon-M camera and grazing incidence beamsplitter combination, described in 3.3. The beamsplitter is used to reflect XUV light into the camera while partially transmitting both the laser and hard x-ray betatron radiation. The experimental set-up is shown in figure 5.1. When the CCD camera is close to the gas jet (configuration (b) in figure 5.1), the quadrupole magnets and electron spectrometer are removed from the beamline and the electron energy is measured by the smaller 0.7 T bending magnet, described in 3.3. The bending magnet prevents electrons from the wakefield accelerator from reaching the CCD camera.

Images are analysed by first rotating them to ensure that the interference patterns line up with one of the axes so that line out plots could easily be generated, a region of interest is then selected to cover the interference pattern but cropping out the regions where the signal due to laser light is high. Similar to the measurements with the XUV spectrometer, care had to be taken when choosing a background image due to laser light leaking through pinholes in the filter material which is visible in figures 5.12(b) and (c). The position of the filter inside the carousel could be adjusted to move the damage away from the signal but this was not sufficient to totally avoid it. For each run, the shot used for the background contained the average number of counts for a blank shot inside the region of interest (ROI). Example images used for the background with each filter are shown in figure 5.12 including the ROI, delineated with a blue rectangle, where the interference pattern is expected, which also defines the analysis window.

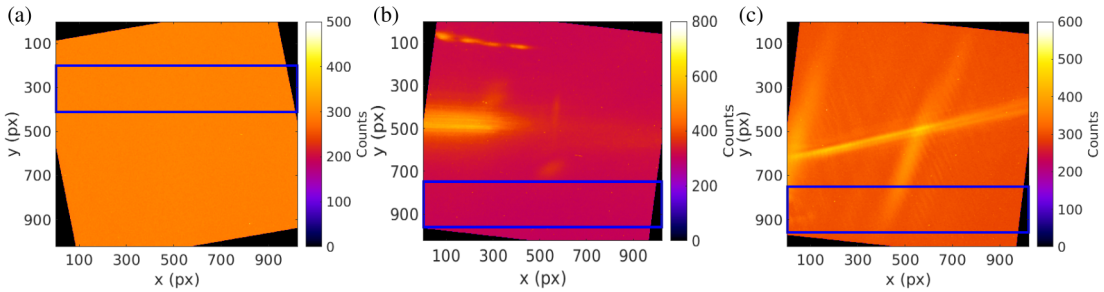

Figure 5.12: Typical image used as a background for the (a) aluminium, (b) zirconium and (c) indium filters. The ROI chosen for the analysis is shown in blue.

Once a background image is subtracted from each image, the two dimensional interference pattern used for calculating the wavelength and coherence of the radiation is created by summing the signal in each column of the ROI. The wavelength of the radiation is estimated from the interference pattern by taking a Fourier transform, which has a resolution limited by the number of pixels in the ROI and the camera pixel size. The result of this is that the most significant wavelength component can easily be found but there insufficient signal and resolution to fully resolve any minor wavelength components, which may evident in the spectra presented in chapter 4. The visibility of the fringes is then calculated always using the central maximum and the

first minimum of the interference pattern which is then used to calculate the equivalent source diameter using equation 5.10.

5.3.1 Aluminium filter

The combination of the aluminium filter and the beamsplitter limits the bandwidth of the radiation where significant radiation is detected between 17 and 30 nm. Each of the three double slits are used to measure the transverse coherence of the XUV radiation. Typical interference patterns for each of the three double slits are shown in figure 5.13.

The wavelength of the radiation determined using the double slit measurements, with an average measured wavelength of all shots of (20.0 ± 0.2) nm, compares well with the values from the XUV spectrometer. The corresponding Fourier transform for each of the example images in figure 5.13 shows evidence of the modulations in the spectrum where there is a main peak at ≈ 20 nm and a second at ≈ 25 nm similar to the spectral measurement in chapter 4.1. Although the small (~ 100) number of pixels used for the Fourier transform limits the resolution of the wavelength measurement. Further experiments with a narrower slit width would spread the radiation over a larger proportion of the CCD sensor of the camera allowing more pixels to contribute to the Fourier transform. The fringe visibility varied considerably from shot-to-shot between 58% and 99%, which is most likely due to a combination of shot-to-shot fluctuations in the background level and variations in the source due to random variations in the laser parameters and the plasma density. The fringe visibility for each shot with each double slit is shown in figure 5.14(a), plotted as a function of the number of photons measured inside the analysis region of interest normalised against the open area of the double slits, which is estimated from the number of counts recorded by the CCD camera, and the wavelength measured by the interference fringes.

Assuming a circular source, equation 5.10 is solved for each interference pattern using the measured wavelength and fringe visibility to calculate the source size diameter for that shot. Figure 5.14(b) shows that the source size varied between 11 and 103 µm with an average value of (58.2 ± 2.0) µm, when considering data with all three double slits. A summary of the results, measured wavelength and fringe visibility, using the

aluminium filter to block the laser and each of the double slits is presented in table 5.2. The calculated average source size diameter from the measured fringe visibilities shows that it is approximately equal to the laser waist diameter in vacuum of 53×57 µm (see figure 3.9).

Slit separation (µm)	**Wavelength** (nm)	**Average visibility** (%)
90	21.0 ± 0.3	91 ± 1
150	19.8 ± 0.3	79 ± 1
250	19.3 ± 0.7	61 ± 1

Table 5.2: Summary experimental results of XUV coherence with the aluminium filter and each of the double slits.

5.3.2 Zirconium filter

The zirconium filter and beamsplitter limit the XUV radiation to between 7 and 17 nm. The efficiency of the filter, beamsplitter and CCD camera combined efficiency is shown in figure 5.15. The fringe visibility and radiation wavelength is measured using the three filters listed in table 5.1. The average wavelength measured matches the spectrometer measurements in with average values of (14.5 ± 0.11) nm for both the double slits and the spectrometer (section 4.2). A representative shot with each of the three double slits is given in figure 5.16.

Radiation in the range transmitted by the zirconium filter displays a high degree of coherence with the best shots having a fringe visibility from 40% up to 99%, equivalent to a source size of 10 to 114 µm assuming a circular or Gaussian source. The measured visibility and wavelength from each shot was used to estimate the equivalent source size diameter as shown in figure 5.17(b). The average source size is smaller than that of the aluminium filter with a value of 47.4 µm when averaging over the data with each of the slit separations. The average source size diameter for the double slits with 90, 150 and 250 µm slit separations are 62.8, 46.5 and 26.6 µm, respectively. A summary with the wavelength and fringe visibility of the full data set is given in table 5.3.

Slit separation (µm)	**Wavelength** (nm)	**Average visibility** (%)
90	14.5 ± 0.3	82 ± 2
150	14.5 ± 0.1	75 ± 1
250	14.5 ± 0.4	77 ± 3

Table 5.3: Summary of XUV coherence measurements with the zirconium filter and the double slits.

5.3.3 Indium filter

The combination of the XUV beamsplitter and the indium filter gives a narrow transmission window between 5 and 11 nm (see figure 5.18). In this case, only data using the double slit with a slit separation of 150 µm is collected. Laser shots showing fringes are uncommon and only 17 of the 1500 shots exhibited fringes. A representative shot with the double slit is shown in figure 5.19.

The average wavelength of the XUV radiation transmitted through the indium filter is (9.3 ± 0.2) nm, which is similar to the wavelength of 10.3 nm for spectral peaks measured using the spectrometer. The low number of shots reduces the statistical significance of averages of the measurements. XUV radiation in this region again displays a high degree of coherence between 58% and 98% and where the average fringe visibility with the indium filter is (71 ± 3)%. This corresponds to a source size diameter of 7 to 41 µm with an average of (32.0 ± 2.4) µm assuming a circular or Gaussian source geometry. The source size for each shot is shown in figure 5.20(b). Although the degree of coherence is lowest for the indium filter, according to equation 5.10, it corresponds to a small source size because the wavelength of the XUV radiation is very short. Measurements using the three metal filters show that the source size of the XUV radiation decreases with wavelength suggesting that shorter wavelengths are emitted closer to the centre of the laser axis.

5.3.4 Measurements close to the gas jet

The measurements with the double slits have been repeated using the Andor iKon-M CCD camera placed at position (b) in figure 5.1, with the double slits inside the

Slit separation (µm)	**Wavelength** (nm)	**Average visibility** (%)
150	9.3 ± 0.2	71 ± 3

Table 5.4: Summary of experimental results of XUV coherence measurements with the indium filter and a double slit with a separation of 150 µm. No interference patterns were observable using the other two double slits.

interaction chamber at position DS2. In this case, the double slit is 0.567 m from the gas jet and 0.994 m from the CCD camera. The permanent (0.7 T) bending magnet is used to measure the electron spectra, which allows simultaneous measurement of interference fringes from the double slits and the accelerated electron bunch from the laser wakefield accelerator. Due to the short distance and resolution limit imposed by the camera pixel size, interference fringes are only resolvable for the 90 µm double slit. However, measurements of the radiation wavelength agreed with the values obtained at the larger distance between the camera and double slit, with averages of (21.6 ± 0.2) nm and (15.0 ± 0.2) nm for the aluminium and zirconium filters respectively. The source size is again calculated from the fringe visibilities measured on each shot, which gives an average value of (46.7 ± 1.8) µm and (44.0 ± 3.1) µm for the aluminium and zirconium filters, respectively which compares well with the measurements presented in chapters 5.3.1 and 5.3.2.

Electrons are only observed on the low-energy screen of the electron spectrometer, which has a limited the range between 35 and 99 MeV. In total, $\sim 61\%$ of all laser shots result in the observation of electrons on the spectrometer screen. In contrast, 78% of shots containing an interference pattern with the aluminium filter also produce a signal on the electron spectrometer, while with the zirconium filter, 76% exhibit the same behaviour. The higher proportion of shots with a signal on the electron spectrometer screen shows that the emission process of XUV radiation could be linked to the injection and acceleration of high energy electrons in a laser wakefield accelerator, but measurements of the brightness distribution of the XUV spectrum (chapter 4.4) indicate that the emission process is not connected synchrotron radiation from high energy electrons inside the plasma bubble. Even through there appears to be a connection between the presence of a high energy accelerated electron bunch and an

interference pattern, there is no correlation between the number of photons measured or the visibility of the fringes with the integrated charge on the spectrometer camera or electron energy.

5.4 Discussion

A x-ray CCD camera coupled to a grazing incidence beamsplitter has been used to make direct measurements of the profile of the extreme ultraviolet (XUV) beam emitted from the plasma. Due to rapid damage of the aluminium filter, only a small number of data points could be collected. The beam was found to be elliptical in shape with a large variation in the angle between the major axis of the ellipse and the laser polarisation direction, with an average value suggesting that the angle is randomly distributed however this is an average of only 9 shots. For shots where a three dimensional Gaussian fitting script converged to a solution, the average FWHM divergence of the radiation beam is (12.0 ± 1.0) mrad in the major and (7.1 ± 0.4) mrad in the minor axis of the ellipse. The angle between the major axis of the XUV beam and the laser polarisation varied between 3° and 130° with average value of $(57 \pm 16)°$. A large number of images containing an XUV signal did not converge on a solution in the fitting process while others have their centroid outside of the area of the CCD chip, therefore it is likely to underestimate the real divergence. To make this measurement, the camera is placed close to the source to capture the largest possible proportion of the images of the whole radiation beam to improve on this result, and improve on the measurement of the beam divergence. However, these measurements should be repeated with a thicker metal filter that will not suffer damage by the laser. Any differences in divergence with photon energy should also be checked by repeating the experiment with the Zr and In filters, in addition to the Al filter.

With the CCD camera and filter wheel placed further from the gas jet (and therefore the laser focus position), measurements of the brightness of the XUV beam could be made. In this case, the signal approximately uniformly covered the area of the sensor and detected on average $(1.03 \pm 0.13) \times 10^{14}$ photons sr^{-1} and peak of 2.7×10^{15} photons sr^{-1}, which is in excellent agreement with the value obtained using the

spectrometer and the same Al filter.

Three Young's double slits have been used to produce interference fringes to measure the coherence and wavelength of the XUV radiation to estimate the source size, and to act as an independent check of the radiation wavelength. The same aluminium, indium and zirconium filters are used to block the laser as for the spectral measurements which allow the coherence and source size to be measured in three narrow radiation bandwidths while protecting the experimental apparatus. Fourier transforms of the fringes recorded by an x-ray CCD camera gave average wavelengths of 20.3 nm, 14.5 nm and 9.3 nm for the Al, Zr and In filters, respectively, which is in good agreement with the measurements made with the spectrometer. The distribution in the measured wavelength is shown in figure 5.22. The radiation spectra are broad, showing that the interference fringes are comprised of a number of different frequencies with some evidence of the modulations however the resolution is poor due to the small number of pixels which comprise the Fourier transform. Higher resolution measurements can be obtained by choosing double slits that spread the signal over a larger proportion of the CCD sensor or using a camera with a smaller pixel size. Measurements with the slits were performed at different angles relative to the laser polarisation and it was found not to have an impact on the measured fringe visibility.

The number of photons incident on the CCD camera, estimated by integrating the signal over the whole interference pattern, was used to estimate the brightness of the radiation with the wavelength measurement from the Fourier transform of the interference pattern and solid angle of the detector. Figure 5.23 shows good agreement to the values obtained with the spectrometer with a similar distribution with photon energy.

The visibility of the interference pattern is used to estimate the source size of the radiation, using the van Cittert-Zernike theorem and assuming a circular disk shaped source distribution based on the profile measurements and the observation that it gives the same result to a Gaussian intensity distribution. Calculations for two other source geometries were performed, two point sources similar to the observations by Pirozhkov et al., [156] and a narrow ring, which both give smaller source sizes for a given fringe

visibility and wavelength. The source geometry has not yet been determined but it could be imaged with the Kirkpatrick-Baez microscope discussed in chapter 6 or measuring how the visibility changes as a function of slit separation with a series of double slits, after which the assumption of the source shape can be updated.

The fringe visibility is found to vary between 40% and 99%, for all filter materials, giving an average source diameter for the Al, Zr and In filters of 58.2 µm, 47.4 µm and 32.0 µm, respectively with the data for all three slit separations combined. The average value is similar to that of the asymptotic value of the source size when plotted A histogram of the distribution of the source size is shown in figure 5.24 for each filter which peaks close to 50 µm. The measured source size does not correspond directly to a size in the laser plasma interaction (such as the bubble diameter or injected electron size), apart from the laser spot size which was measured in vacuum to be 53×57 µm at high power. One limitation of the van Cittert-Zernike model is that it assumes that the radiation is quasi-monochromatic, which is a condition not met by the relatively broad transmission bands of the metal filters. A simple calculation of the interference pattern in the case of polychromatic light shows that the bandwidth of the radiation has an impact on the measured fringe visibility and prevents a estimate of the temporal coherence to be made. The calculated source size could be smaller if a polychromatic model is used. The next step in estimating the source size would be to place a pinhole with known diameter at a known distance in front of the double slits to act as an artificial source of XUV radiation, and then measure the interference pattern to find out how close the source size as calculated from the van Cittert-Zernike model is, to compare its prediction with the pinhole diameter.

The effect of unequal illumination of the slits was also investigated through calculation. Since the beam size is large compared to the separation of the slits, the ratio of intensity between them has little impact on the expected fringe visibility. This effect should be considered more carefully if the coherence was to be measured with the slits very close to the gas jet.

The insertion of the double slits into the beam path with the CCD camera placed close to the gas jet protects the filters from damage, allowing a check of the measure-

ments to be made with the camera in the same position as for the divergence measurement. The measured radiation wavelength of (19.8 ± 0.3) nm and (15.1 ± 0.2) nm as well as the source size diameter of (57.8 ± 1.8) µm and (42.8 ± 3.2) µm for the Al and Zr filters, respectively, agree with the measurements made with the camera placed further from the gas jet. The inclusion of the bending magnet enables the correlation of the presence of an electron beam with that of the XUV beam to be made. For the majority of images containing an interference pattern (78% for Al and 76% for Zr), a corresponding electron beam is observed, suggesting that there may be a link of the XUV emission processes with high energy electron beams in the LWFA. However, there is no correlation between the electron beam charge or energy, with the number of photons or fringe visibility measured.

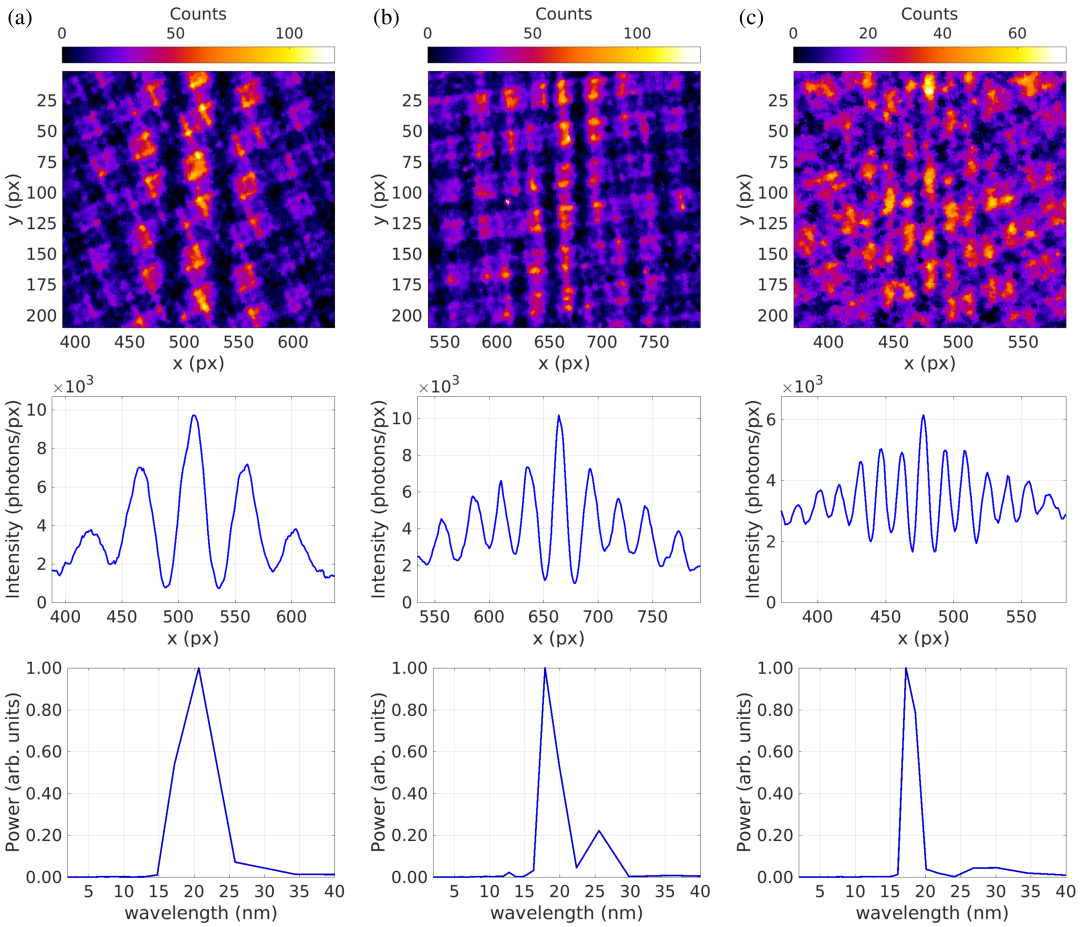

Figure 5.13: Typical interference pattern measured using each of the double slits with the Al filter blocking the laser and the corresponding Fourier transforms. In each case, the double slit is 1.04 m from the gas jet and 2.84 m from the CCD camera. (a) 90 µm slit separation, image corresponds to a wavelength of 20.7 nm and fringe visibility of 86%. (b) 150 µm slit separation, image corresponds to a wavelength of 17.9 nm and fringe visibility of 82%. (c) 250 µm slit separation, image corresponds to a wavelength of 17.3 nm and fringe visibility of 58%.

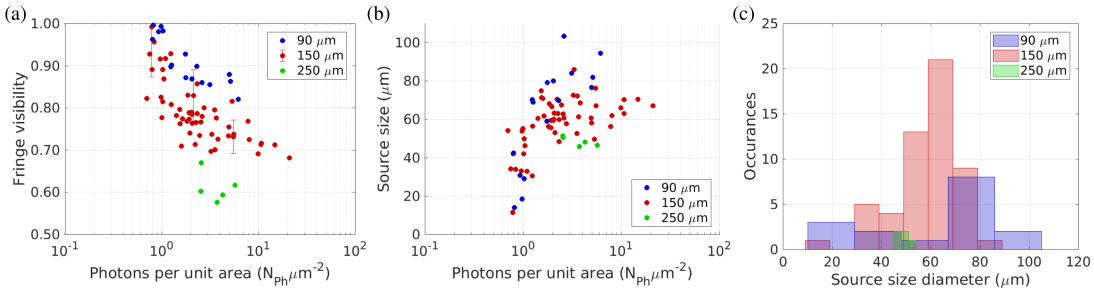

Figure 5.14: (a) Distribution of number of photons per unit area of the double slit in interference pattern with fringe visibility for aluminium filter and double slit with slit separation of 90 µm (blue), 150 µm (red) and 250 µm (green). Error bars are shown for three shots which are representative for the whole data set. (b) Calculated source size diameter for each shot using equation 5.10. (c) Histogram of calculated source size.

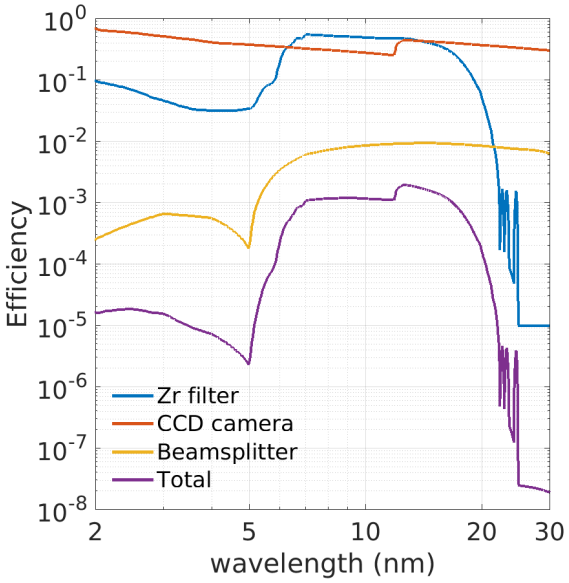

Figure 5.15: Efficiency of the zirconium filter, CCD camera and XUV beamsplitter with the total efficiency of the combination shown in purple.

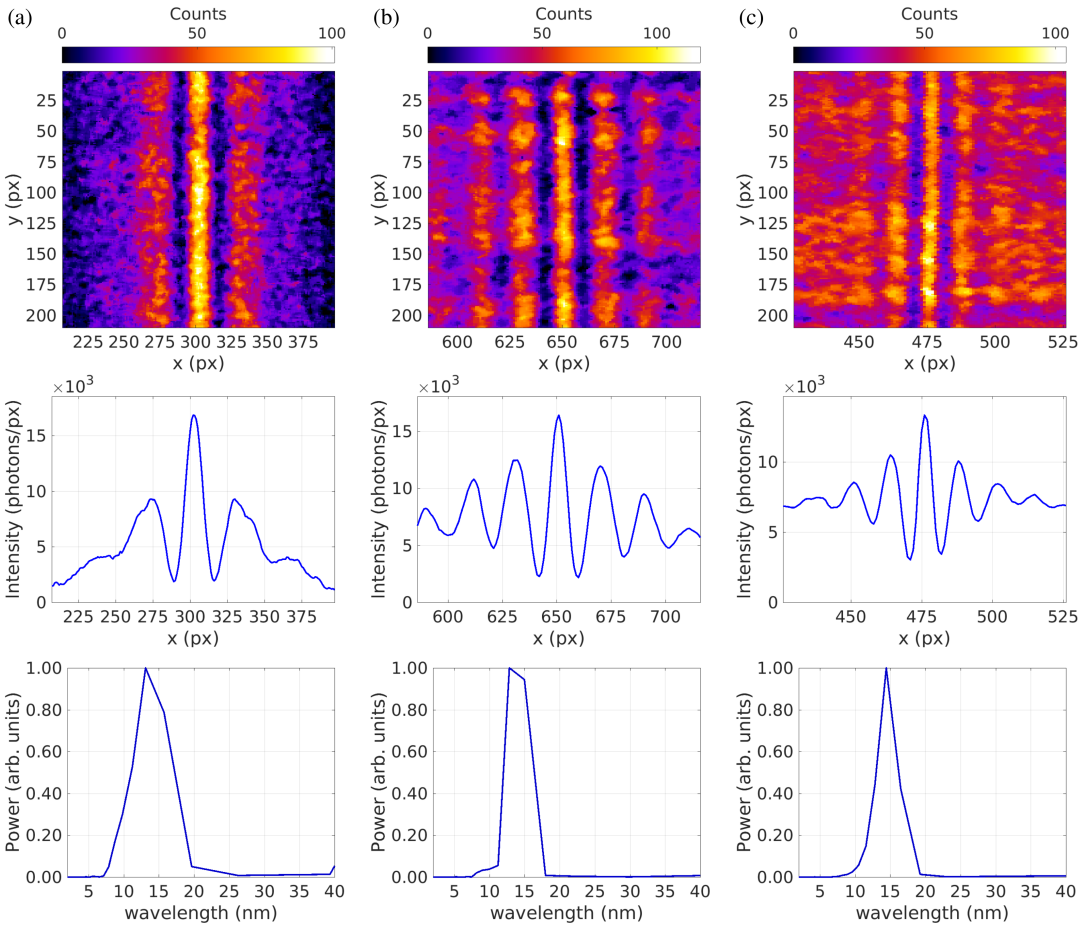

Figure 5.16: Typical interference fringes measured with double slits with 90, 150 and 250 µm slit separations and the Zr filter blocking the laser. In each case, the double slit is 1.04 m from the gas jet and 2.84 m from the CCD camera. (a) 90 µm slit separation: image corresponds to a wavelength of 13.1 nm and fringe visibility of 88%. (b) 150 µm slit separation: image corresponds to a wavelength of 12.9 nm and fringe visibility of 77%. (c) 250 µm slit separation: image corresponds to a wavelength of 14.5 nm and fringe visibility of 63%.

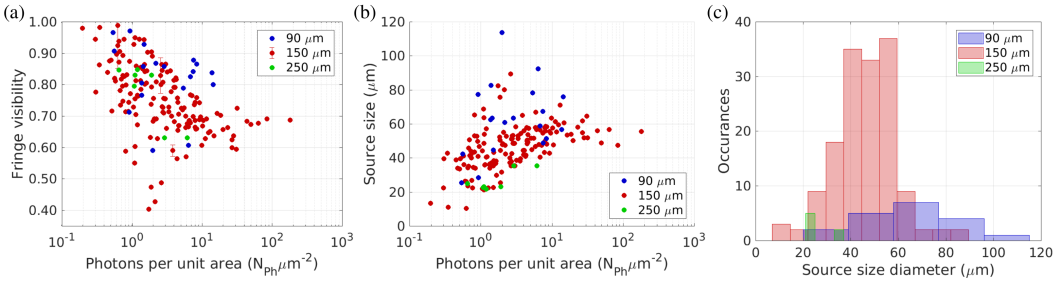

Figure 5.17: (a) Distribution of number of photons in interference pattern with fringe visibility for zirconium filter and double slit with slit separation of 90 µm (blue), 150 µm (red) and 250 µm (green). Error bars are shown for three shots which are representative for the whole data set. (b) Source size diameter calculated for each measured fringe visibility and wavelength from equation 5.10. (c) Histogram of calculated source size.

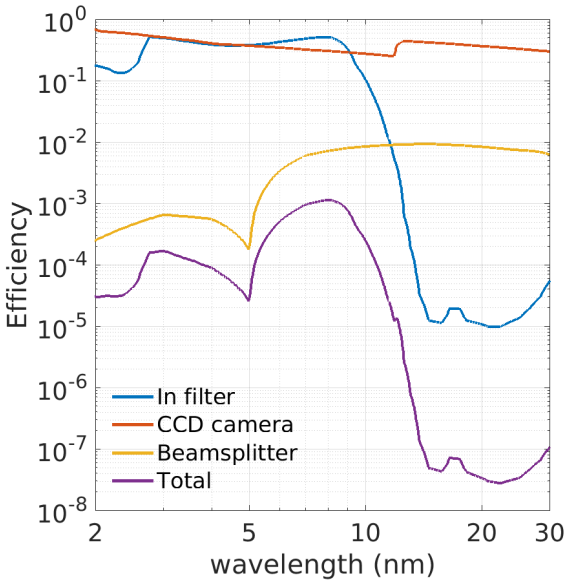

Figure 5.18: Efficiency of the indium filter, CCD camera and XUV beamsplitter with the total efficiency of the combination shown in purple.

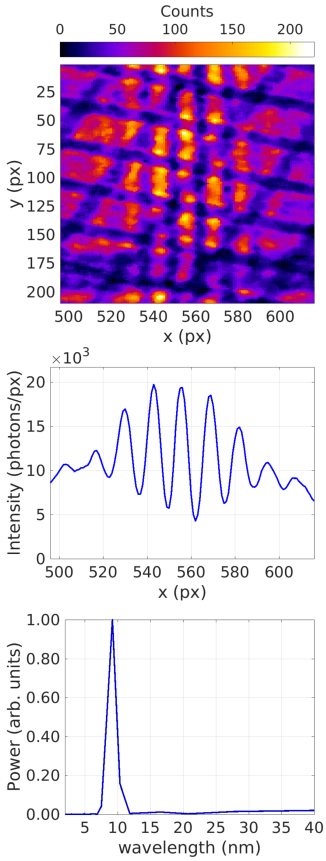

Figure 5.19: A typical interference pattern measured with the indium filter and the double slit with 150 µm slit separation. The double slit was 1.04 m from the gas jet and 2.84 m from the CCD camera. The nickel mesh that supports the indium filter can be seen clearly. The fringes correspond to a wavelength of 9.2 nm and fringe visibility of 64%.

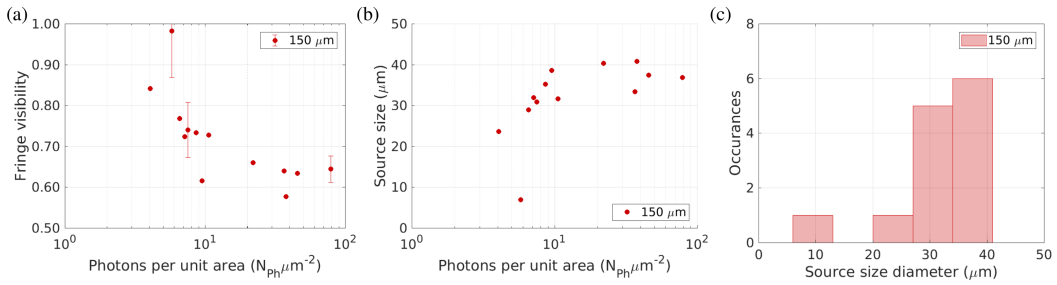

Figure 5.20: (a) Distribution of number of photons in interference pattern with fringe visibility for indium filter and double slit with slit separation of 150 µm, error bars are shown for three shots which are representative for the whole data set. (b) Source size diameter calculated for each measured fringe visibility and wavelength from equation 5.10. (c) Histogram of calculated source size.

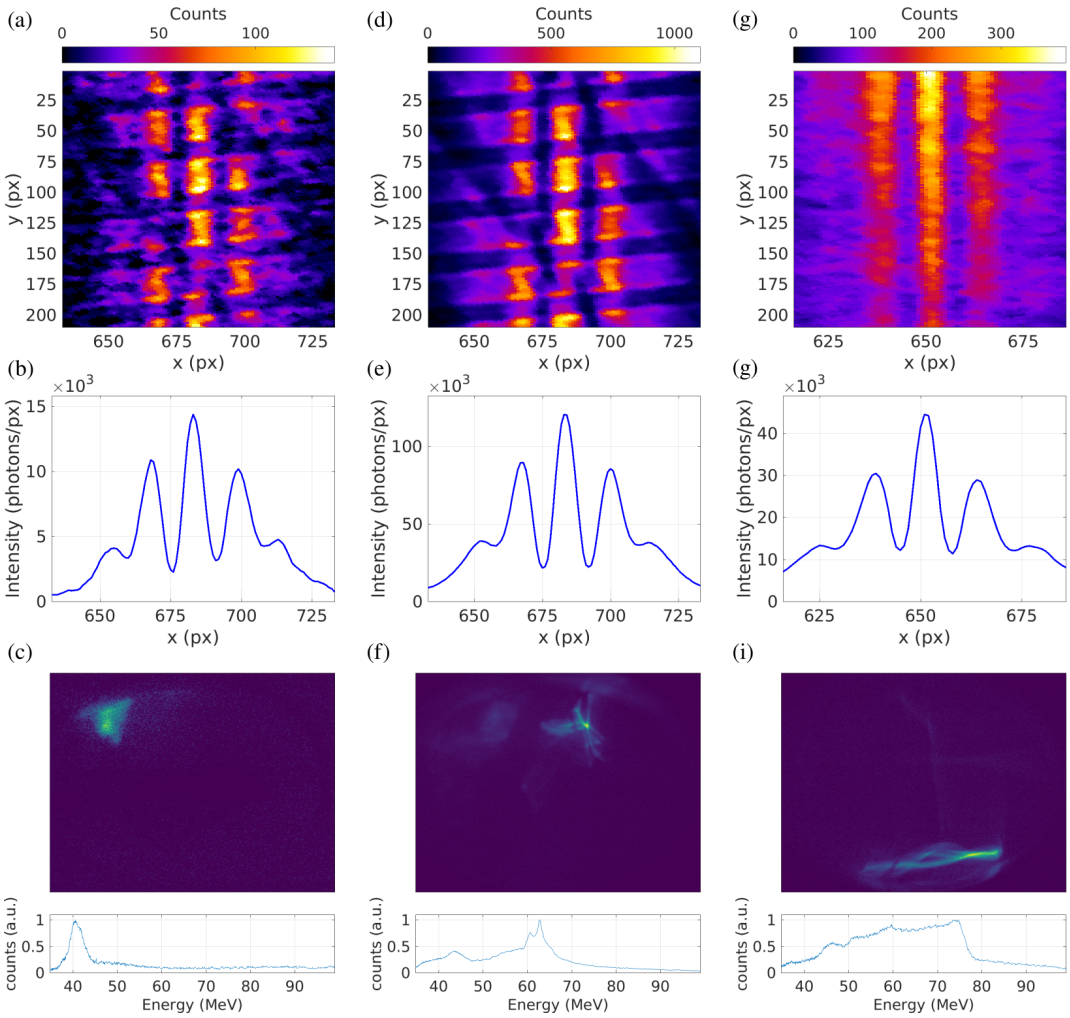

Figure 5.21: Simultaneous measurements of electron spectra with the fringe patterns from XUV radiation with a double slit with a separation of 90 µm and positioned 0.994 m from a CCD camera. (a) – (c) and (d) – (f) are shots where an aluminium filter blocks the laser and, and (g) – (i) correspond to a shot where the zirconium filter blocks the laser.

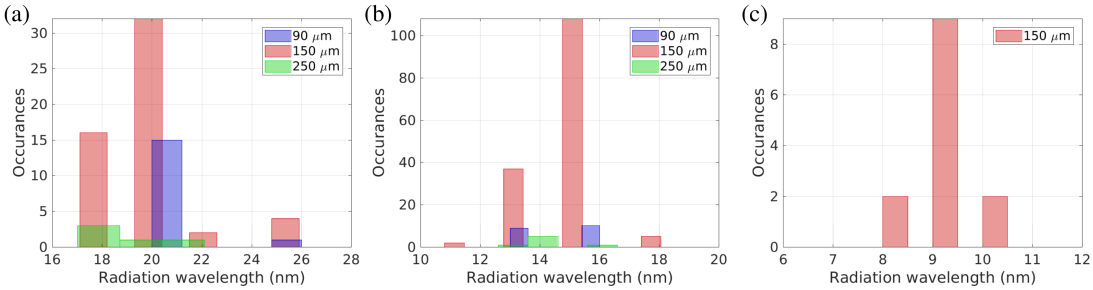

Figure 5.22: Histograms with distribution of measured wavelengths from the double slits for the (a) aluminium, (b) indium and (c) zirconium filters

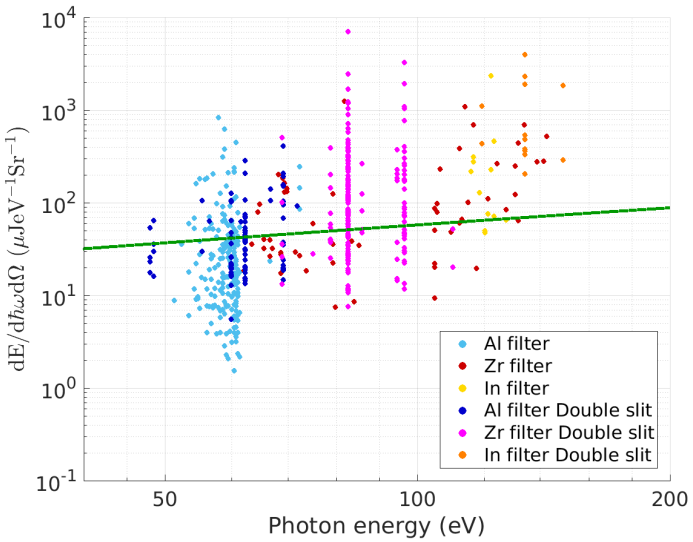

Figure 5.23: Spectral brightness as measured by the McPherson spectrometer and the double slits after correcting for the open area of the double slits. An example betatron spectrum is shown in green corresponding to a critical energy of 2.78 keV.

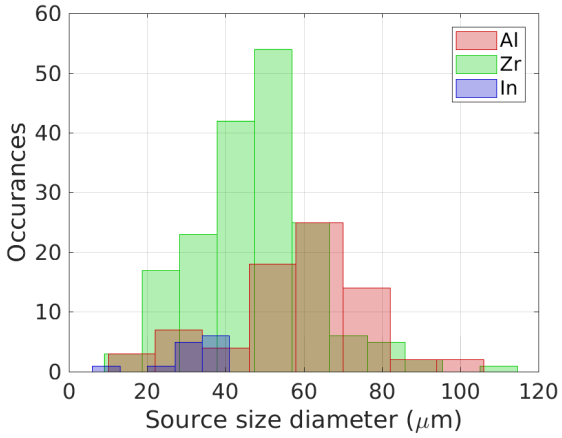

Figure 5.24: Histogram with distribution of calculated source size diameter from equation 5.10, where a circular soruce is assumed, for data with all three slits combined for the Al filter ($18 - 26$ nm), Zr filter ($11 - 18$ nm) and In filter ($8 - 10$ nm).

Chapter 6

XUV and x-ray focusing with a Kirkpatrick-Baez microscope

As seen in chapter 2.5, betatron radiation from a laser wakefield accelerator can be highly divergent, especially for low energy electrons, with a calculated value of 50.6 mrad for the measured electron and plasma parameters presented in chapter 7.3 ($E = 60$ MeV, $n_e = 1.7 \times 10^{19}$ cm^{-3} and $r_\beta = 1.0$ µm). In order for betatron radiation to be a useful source for applications, the area of the beam at the target needs to be controlled so a focusing optic is required. Proposed applications of betatron radiation, such as an upcoming feasibility study to measure the grain orientation of metal alloys, requires an x-ray beam with a millimetre scale beam diameter and high brightness, to enable observation of diffracted photons while targeting single grains of a sample. The focusing optic is required to target a single grain of the alloy which is 0.5 to 2 mm for the β phase Ti-5Al-5Mo-5V-3Cr sample of interest. The results from this experiment will be benchmarked against a backscattered diffraction measurement. A laser-plasma laboratory equipped with an effective focusing system could act as an alternative high brightness x-ray source to allow scientists unable to obtain time on synchrotron or free electron laser facilities to preform experiments with the advantage of femtosecond duration x-ray pulses, allowing resolution in time on the scale of atomic motion. If initial proof of principle experiments are successful, other applications of a focused betatron x-ray beam could be investigated including time-resolved x-ray absorption

spectroscopy [196–198]. In collaboration with Centro de Láseres Pulsados (CLPU) in Salamanca Spain and the University of Alberta in Canada, the ALPHA-X team has designed, manufactured and tested a Kirkpatrick-Baez (KB) microscope that is capable of focussing hard and soft x-ray radiation to make it suitable for a range of applications since the optimum photon energy for focusing and the focal length of the KB lens can be chosen. The KB microscope manufactured for use in the SCAPA laboratory has mirrors that are adjustable for grazing angle and radii of curvature to optimise the focussing strength and efficiency for photon energies between 1 and 20 keV. A CAD drawing of the KB microscope is shown in figure 6.1.

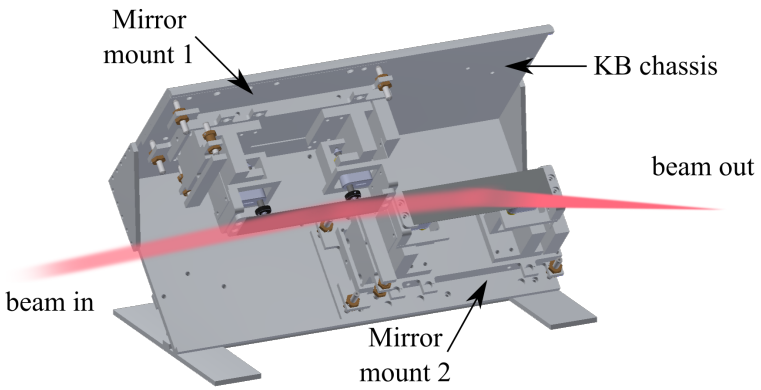

Figure 6.1: Full 3D CAD drawing of the KB microscope with each of the major components labeled.

6.1 The Kirkpatrick-Baez concept

The Kirkpatrick-Baez configuration for focusing x-rays was first proposed in 1948 [199] by Paul Kirkpatrick and Albert Baez, who showed that x-rays can be efficiently reflected and focused to create an image, using either a pair or triplet of concave spherical mirrors set at shallow grazing angles. In a two mirror configuration, x-rays are focused first vertically, by reflection from a mirror nearer the source, and then horizontally by a second mirror placed a short distance down-stream. With high quality optics (extremely flat and smooth, and with accurate control over their shape when under stress) and careful alignment, an x-ray focal spot sizes of less than 50 nm have been

achieved with efficiencies approaching 100% at undulator and FEL facilities [200, 201]. The SCAPA laboratory KB microscope consists of two rectangular mirrors made from high grade silicon wafers, which are 1.5"× 6" (152.4 × 38.1 mm), placed perpendicular to each other. The wafers are sputter coated with a 40 nm thick layer of platinum.

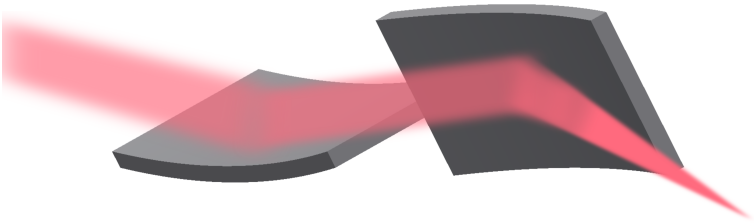

Figure 6.2: Schematic of the two rectangular curved mirrors that make up a Kirkpatrick-Baez microscope, which focus an incoming radiation beam (from left to right). Mirrors are Si wafers coated with 40 nm Pt and oriented at 90° relative to each other.

The two mirrors act as an effective thin lens, such that

$$\frac{1}{f} = \frac{1}{p} + \frac{1}{q}, \tag{6.1}$$

where f is the focal length of the KB system, p is the distance from the source to the centre point between the two mirrors, and q is the distance from the centre of the two mirrors to the image plane. Similar to a thin lens, the magnification of the image is given by $M = q/p$. For a curved mirror, the focal length is a function of the grazing angle of the mirror (ϕ) and the mirror radius of curvature (ROC),

$$f = \left(\frac{\mathrm{ROC}}{2}\right)\sin(\phi). \tag{6.2}$$

Due to the geometry of the system, the beam at the output of the KB microscope deviates by an angle relative to the incoming beam of twice the quadrature sum of the two grazing angles of the mirrors,

$$\theta = 2\sqrt{\phi_1^2 + \phi_2^2}. \tag{6.3}$$

The KB microscope comprises three main components: two mirror mounts and the main chassis of the KB, where the chassis supports the two mirror mounts at positions shown in figure 6.1. The mirror mounts contain all components required to control the orientation and position of the mirrors - adjustment of the mirror grazing angle, bending of the mirrors to the adjust the radii of curvature and correction any twist in the mirrors. A CAD drawing of the mirror mounts is shown in figure 6.3, where all the major components are labelled.

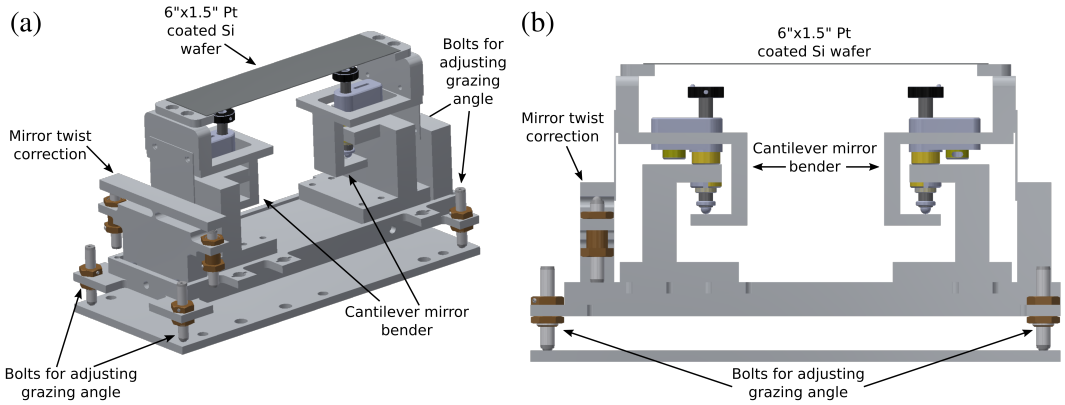

Figure 6.3: Labelled CAD drawing showing two views of the mirror mount used to support the platinum coated wafer in place, and adjust the grazing angle and the required bending moment to the mirror for focusing.

For each mirror, the grazing angle is adjusted using four fine pitched bolts placed at each corner of the plate attaching the mirror mount to the chassis. These are adjusted in pairs to keep the angle between the two mirrors at 90°. The procedure for correctly setting the grazing angle is discussed in section 6.1.1. With the rear two bolts screwed all the way in and the front two all the way out, the maximum grazing angle that can be selected is $\sim 2.5°$. The bolts adjusting the grazing angle push against four springs (not shown in diagram), which presses the mirror mount against the chassis.

Four cantilever benders, one at each side of a mirror, are used to add a bending moment to the mirrors to adjust their radii of curvature (ROC), which allows the beam to be focused. These employ a cantilever design to turn the linear motion of a piezo motor to a rotational motion that bends the mirrors into an approximately spherical shape. Each bender is equipped with two motors, one at either side of the mirror,

that can be controlled independently, allowing for fine adjustment of the shape of the mirrors, which enables the focal spot to be optimised.

Two bolts on one side of each mirror push on the edges of the mirror to remove any twists that may be present. Adjustments are carried out while observing the changes in the spot of an alignment laser focused onto a CCD camera, to optimise it's uniformity and minimise it's waist, which is only adjustable by hand in air. Each KB mirror is glued, using a vacuum-grade epoxy resin, to two holders that are screwed onto the bender section of the mirror mount. A small amount of glue is applied to the holders and the mirror is gently dropped on top of the glue, which is then allowed to cure. It is at this stage that uneven thickness or differential curing of the glue may introduce a twist into a wafer or stress that effects the flatness. The correction bolts help to restore the surface profile of the mirror to its original flatness.

The surface profile of the mirrors for the KB microscope have been measured with a Zygo interferometer [202] using a laser with wavelength 632 nm. The mirror flatness is measured while no stress is applied prior to gluing to the holders and attaching to the bender. The beam size of the Zygo is not large enough to measure the profile of the whole mirror and therefore is measured in two halves, numbered arbitrarily. The mirrors in figure 6.4 have a flatness (peak to trough) across their full length of 5.2 µm, for the entrance mirror, and 6.6 µm, for the exit mirror. The best two mirrors have a flatness of 3.5 µm and 4.0 µm, respectively, and were kept for experiments at high power so were not used for testing. The effect of hanging the mirrors from the chassis on the mirror mount, and gluing of the mirrors onto the holders has not been determined.

If the two mirrors of a KB microscope have the same grazing angle and radius of curvature, then an elliptical beam is expected because the values of p and q are modified in each case by half the mirror length plus half the gap between the mirrors. The magnification is therefore independently defined for each mirror. The values for p and q become

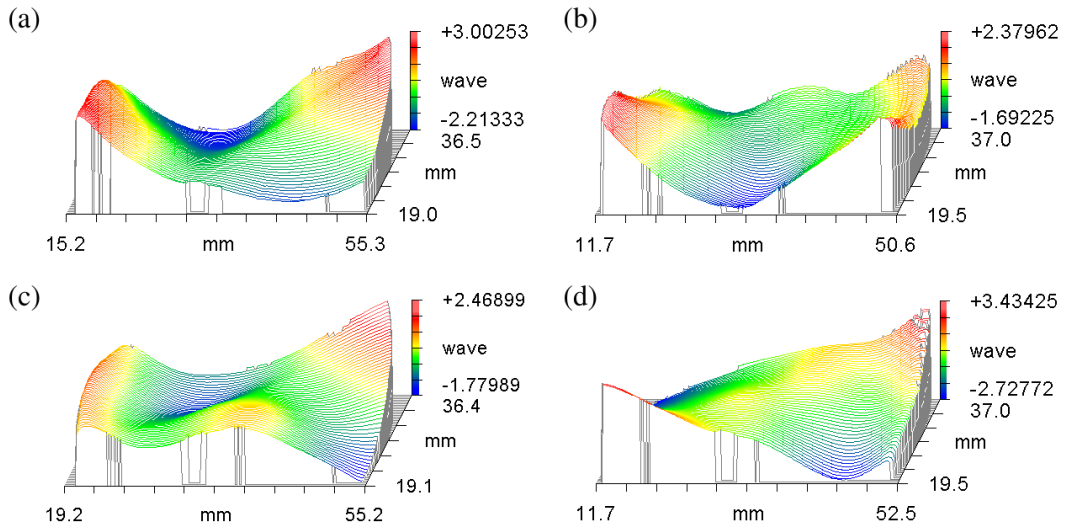

Figure 6.4: Zygo interferometer measuement of the flatness of the two mirrors used to test the Kirkpatrick-Baez microscope. (a) Entrance mirror side 1, (b) Entrance mirror side 2, (c) Exit mirror side 1, (d) Exit mirror side 2. In each case, side 1 and 2 are chosen arbitrarily.

$$\begin{aligned} p_{A,B} &= p \mp \left(\frac{l+d}{2}\right) \\ q_{A,B} &= q \pm \left(\frac{l+d}{2}\right), \end{aligned} \tag{6.4}$$

where the subscripts for p and q denote the mirror number (mirror A refers to the first reflection and B to the second), l is the mirror length and $d = 2.5$ cm is the distance between the two mirrors.

6.1.1 Optimising grazing angle

The reflectivity of the mirrors is calculated using the x-ray Oriented Programs (XOP) [183] with the IMD extension [184] which uses the database for X-ray applications (BABAX). The reflectivity of a material depends on the grazing angle of incidence and the energy of the incident photons, as shown in figure 6.5. To optimise the grazing angle of the platinum coated mirrors used in the KB microscope and maximise the number of photons in the focal spot, a balance must be found between the mirror reflectivity

and the aperture size, which is proportional to grazing angle.

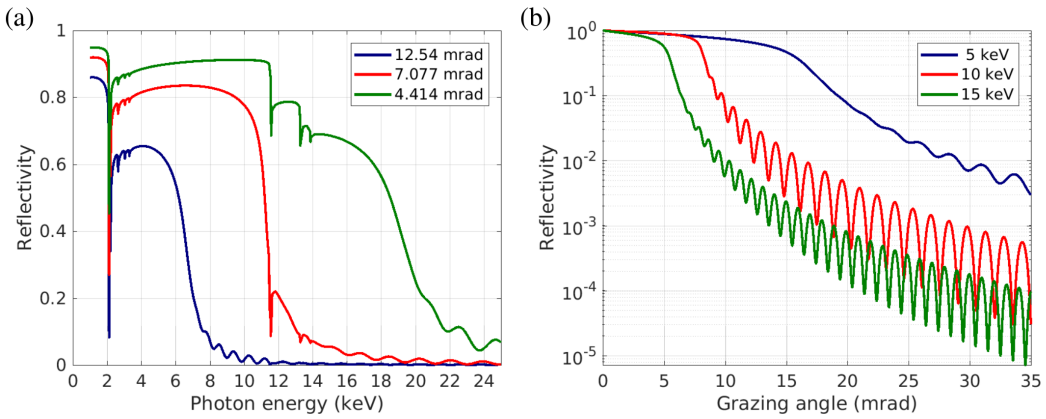

Figure 6.5: Mirror reflectivities as a function of (a) photon energy and (b) grazing angle, calculated using XOP for 5 keV (blue), 10 keV (red) and 15 keV (green) photons. Mirrors have a silicon substrate coated with 40 nm of platinum.

To find the optimum grazing angle, the relative reflectivity (R_R) is defined as the product of the mirror reflectivity with the size of the KB aperture. The aperture of a single mirror is given by

$$A = lw\sin(\phi), \tag{6.5}$$

where l and w are the length and width of the mirror, and ϕ is the grazing angle of the mirror, respectively. For a mirror reflectivity, R, the relative reflectivity is given by

$$\begin{aligned} R_R &= RA \\ R_R &= Rlw\sin(\phi). \end{aligned} \tag{6.6}$$

The relative reflectivity curves for three example photon energies in the region where betatron radiation is emitted are shown in figure 6.6, where the optimum grazing angle for a given photon energy is taken to be at the peak of the curve. For 5, 10 and 15 keV, the optimum grazing angle is 12.54, 7.077 and 4.414 mrad. When the photon energy is low, such as 5 keV, the reflectivity changes more slowly with grazing angle than for high energy photons, therefore it is an advantage to have a large grazing angle (and

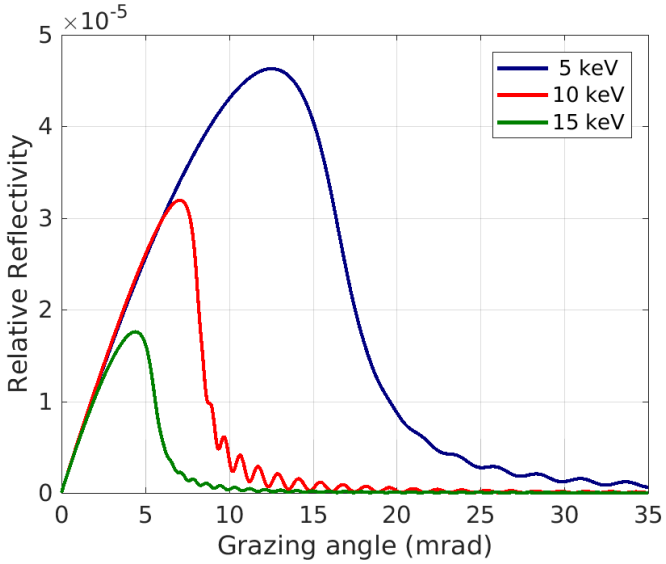

Figure 6.6: Relative reflectivities calculated using those obtained from XOP for 5 keV (blue), 10 keV (red) and 15 keV (green). The bulk of the mirrors are silicon, which is coated with 40 nm layer of platinum. The optimum grazing angle for each photon energy is 12.54, 7.077 and 4.414 mrad for 5, 10 and 15 keV respectively.

therefore large aperture), which transmits a larger proportion of the beam through the KB. For high photon energies, such as 15 keV, the reflectivity falls quickly with grazing angle, therefore to maximise the number of photons in the focal spot a smaller aperture should be chosen. The variation in optimum grazing angle with photon energy is shown in figure 6.7, where the red line is a fit to the calculated points shown in blue. For the XUV radiation presented in chapters 4 and 5, the optimum grazing angle for these photon energies (< 300 eV) is outside the optimum range of the KB microscope. For example, the optimum mirror grazing angle for 120 eV (10 nm) photons with the Strathclyde KB microscope mirror size is $\phi = 222.1$ mrad ($\phi = 12.73°$). In this case the angle of incidence is too large to be considered a grazing angle and the simple relationships in chapter 6.1 no longer apply. Focusing of XUV radiation is planned at 2°, to get as close to the optimum angle as possible within the constraints of the KB chassis, while remaining within the grazing angle range.

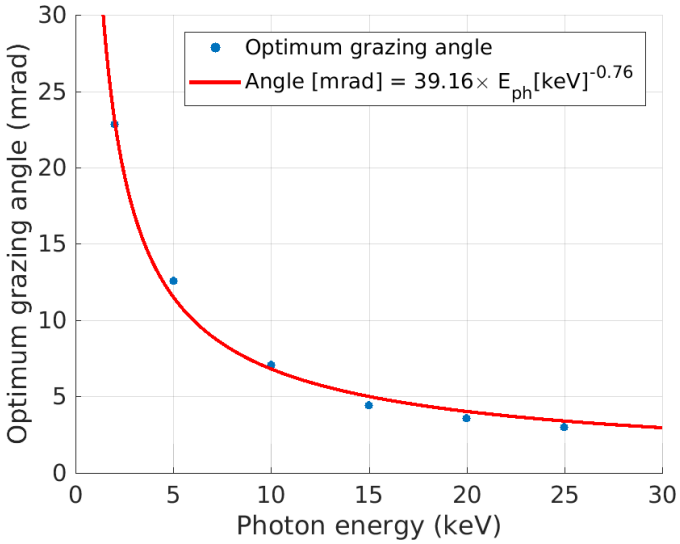

Figure 6.7: Calculated optimum grazing angles for x-ray photons between 2 and 25 keV using XOP software and equation 6.6.

6.1.2 Alignment of Kirkpatrick-Baez mirrors

The beam transmitted through the KB microscope produces four spots: the focal spot, an undeviated beam, which does not intercept either mirror, and two spots that have reflected off just one mirror. These four spots make up the corners of a square, as illustrated in figure 6.8, which provides a convenient way of aligning the KB microscope, based on geometric arguments due to the reflection of each mirror.

The length of the diagonal of the square, d, grows with distance from the KB mirrors as

$$d = q\tan(\theta), \tag{6.7}$$

where q is the distance from the KB mirrors to the focal plane and θ is the angle that the beam deviates from the incoming beam, which is calculated using equation 6.3. Assuming that the grazing angle of each mirror is the same, $\phi = \phi_1 = \phi_2$. The four points form a square, and by Pythagoras theorem, its diagonal is given by $d = \sqrt{2}l$. These two terms for the square diagonal can be equated to calculate the length of the sides of the square,

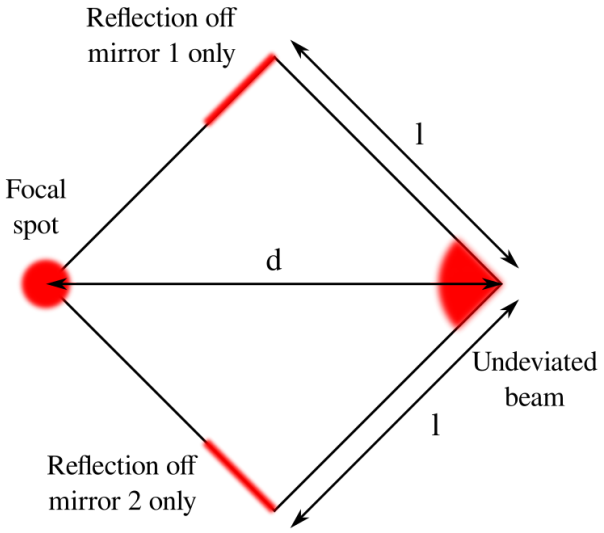

Figure 6.8: Sketch showing the four spots created by a KB microscope, assuming that the grazing angle of the two mirrors is the same. The four points form a square with diagonal, d and side length, l. The relative distance between the points and the distance from the KB mirrors to the focal plane are used to check the alignment of the two grazing incidence mirrors.

$$l = \frac{q \tan(\theta)}{\sqrt{2}}. \tag{6.8}$$

The length and diagonal of the square are both easy parameters to measure in the laboratory (compared with measuring the mirror grazing angles $< 1°$) directly, thus allows to check that the sides of the square are the correct length for a chosen grazing angle and distance to image plane, and therefore allows corrections to be made by adjusting the grazing angle of the mirror. Equation 6.8 can be rearranged to check the deviation angle (θ), and in turn the mirror grazing angle (ϕ) by

$$\theta = \tan^{-1}\left(\frac{\sqrt{2}l}{q}\right), \tag{6.9}$$

and

$$\phi = \left(\frac{1}{2\sqrt{2}}\right)\tan^{-1}\left(\frac{\sqrt{2}l}{q}\right), \tag{6.10}$$

where it is assumed that the two grazing angles of the mirrors are equal. If the two grazing angles are not equal, then a rectangle is formed, and the method must be modified to ensure it is still valid, by calculating the two side lengths of the rectangle independently using their corresponding value of ϕ. The KB is aligned using this method for all the results presented in the remainder of the chapter because the condition $\phi_1 = \phi_2$ is always met.

6.2 Kirkpatric-Baez tests with an alignment HeNe laser

Initial tests of the Kirkpatrick-Baez microscope have been performed with a helium neon (HeNe) laser. Sets of parameters (p, q, ϕ) are chosen to match the expected parameters on the ALPHA-X beamline. A low power (0.5 mW) HeNe laser with central wavelength 633 nm and $1/e^2 = 0.57$ mm diameter at the laser exit and a divergence of 1.41 mrad (full angle), is used for testing the KB. The KB microscope is tested for three cases: grazing angle for XUV radiation, with an $\sim 1:1$ image, grazing angle for XUV radiation with high magnification and a grazing angle chosen for betatron radiation. Each of these tests, including the betatron focus, are performed with the set of mirrors from figure 6.4.

6.2.1 Grazing angle for XUV radiation at low magnification

The first test with the Kirkpatrick-Baez microscope is its ability to focus a HeNe laser with low magnification (approximately $1:1$). The HeNe laser is installed $p = 1.3$ m from the centre point between the two mirrors and a Flea3 CCD camera (FL3-FW-14S3M), with pixel size 4.65 µm, is positioned $q = 1.24$ m from the centre point between the mirrors ($M = 0.95$). The grazing angle of the mirrors is set to $\phi = 2°$, the value chosen for focusing XUV radiation. Using the method described in 6.1.2 and equation 6.3 gives a deviation angle of $\theta = 5.66°$. The corresponding mirror radii of curvature, in this case, is 36.37 m. A camera shutter duration of 50 ms is chosen, the gain is set to 0 dB and sufficient neutral density (ND) filters are inserted in front of the CCD to avoid saturation of the sensor when the laser is focused. The focus is found by first totally

relaxing each of the four piezo motors to ensure that none of them touch the mirror benders. Pressure is then applied by driving each of the motors in turn, by a small amounts at a time, keeping the curvature of both mirrors approximately equal, until a small spot is observed on the camera. Finally, fine tuning of the motors establishes the optimum focal spot. The expected laser spot size is calculated using equation 6.4 for the laser spot size at the exit of the HeNe cavity.

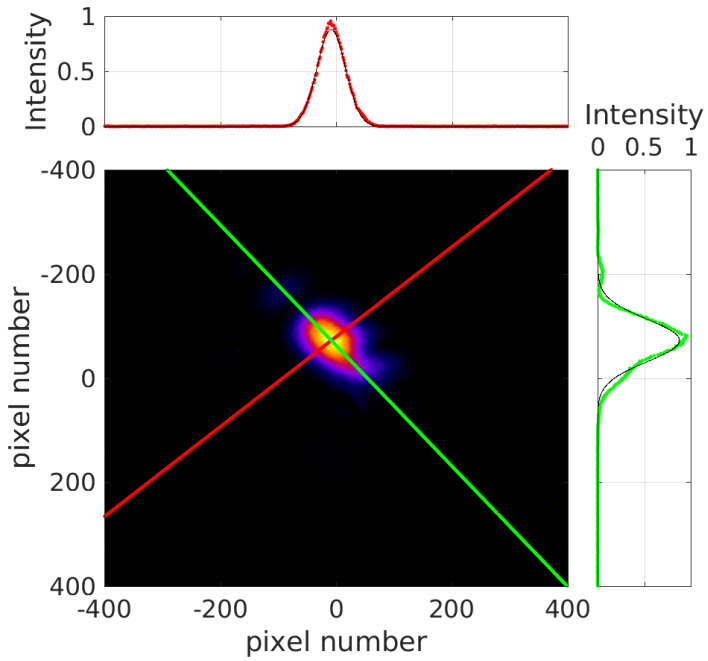

Figure 6.9: Focused HeNe laser spot with KB microscope with $p = 1.3$ m, $q = 1.24$ m and $\phi = 2°$. Measured focus spot size in this image is 458 µm in the minor axis and 759 µm in the major axis to the $1/e^2$ diameter.

The minimum spot size achieved with the KB to the $1/e^2$ diameter is 458 µm along the minor axis and 759 µm along the major axis, as shown in figure 6.9, which compares well with the calculated values 473 µm and 625 µm, respectively, corresponding to a beam quality factor of $M^2 = 1.21$. To confirm that the CCD camera is at the focus, the mirrors are adjusted to find the smallest spot size possible and then the camera moved towards and away from the KB, along the path of the laser. Figure 6.10 to confirms that the KB microscope is focused at the position of the camera.

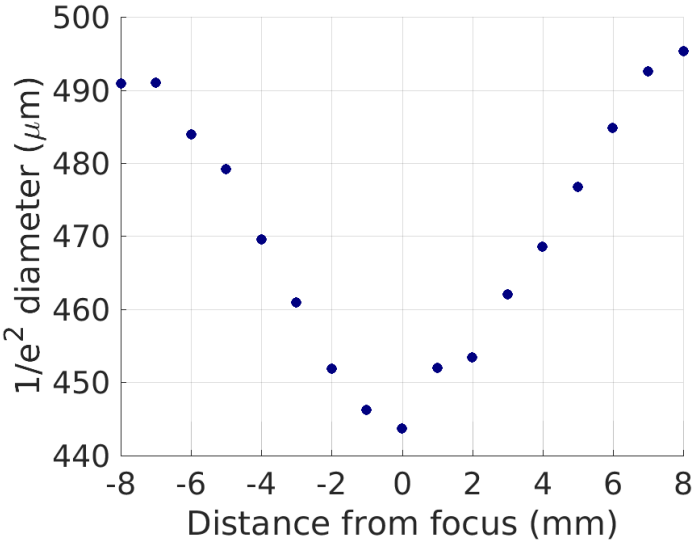

Figure 6.10: Plot showing the variation of the minor of the laser spot with camera position where 0 is the initial position of the camera at $q = 1.24$ m and positive values are moving away from the KB microscope.

The effect of adjusting the curvature of a single mirror on the spot size of the laser has been investigated. The curvature of both mirrors are adjusted to find the best position for the smallest spot size. The two motors that adjust the curvature of a single mirror are moved by an equal amount, where negative values denote the mirror being relaxed. Figure 6.11 shows that adjusting the position of a single mirror has a significant effect on the axis of the beam corresponding to that mirror, and a small effect on the other axis. The KB entrance mirror determines the size of the laser minor axis and the exit mirror defines the size of the major axis. Close to the zero position in figures 6.10 and 6.11, a jump in the diameter of the beam can be seen. This is due to the fact that measurements always start from the zero position, moving in one direction to the maximum value and then the motors are moved back towards the zero before moving in the other direction. The jump in spot size is an indication that the reproducibility of the mirror radius of curvatures is poor. When focusing the laser, the best position of the focus must be found iteratively rather than counting the number of steps of the piezo motor. The position of the beam on the CCD camera is also moved when returning to the initial position of the motors. There is clearly some hysteresis.

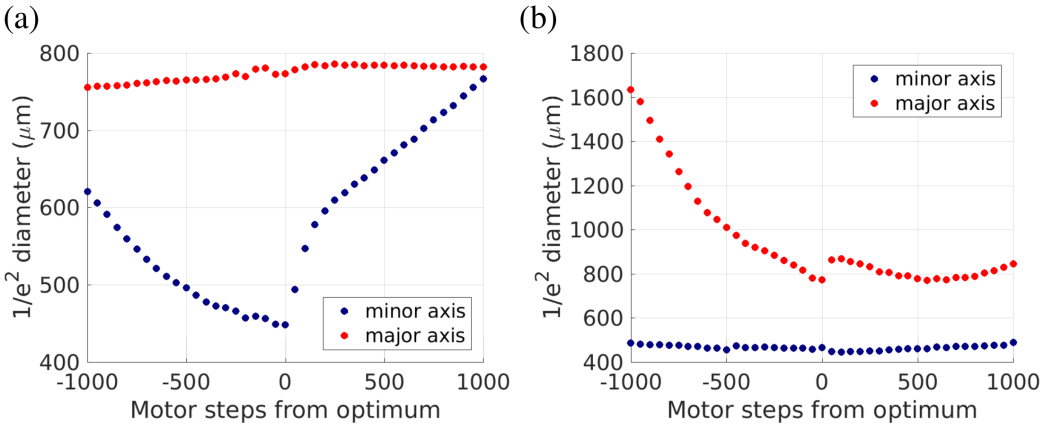

Figure 6.11: Variation of laser spot size when adjusting the motors for a single mirror only. (a) Radius of curvature of entrance mirror adjusted. (b) Radius of curvature of exit mirror adjusted.

6.2.2 Grazing angle for XUV radiation at high magnification

The fringe visibilities from chapter 5 suggest that the source size of the XUV radiation from the plasma can be as large as $\sim$ 50 µm, therefore focusing the radiation with a magnification close to 1 would result in a focused spot covering only about 4 pixels on the XUV CCD camera, which has a pixel size of 13 µm, as described in chapter 3.3.3. It is therefore necessary to test the operate of the Kirkpatrick-Baez microscope for high magnification, to image the source of the XUV radiation from the plasma and to identify its shape. Due to limitations in the size of the experimental area a value of $q = 5.00$ m is chosen to give the largest possible magnification and in turn the largest spot size. In this case, the magnification is $M = 3.85$, mirror radius of curvature is 59.13 m and the mirror grazing angle is kept at $\phi = 2.0°$. The laser spot diameter to $1/e^2$ achieved in the high magnification mode is 2.32 mm and 2.62 mm, for the minor and major axes, respectively, whereas the expected values from solving equation 6.4 is 2.02 mm and 2.39 mm. Similar to the low magnification case, the entrance mirror of the KB focuses the beam better than the exit mirror and produces a focal spot close to the calculated value. For both axes the value measured is further from the expected value than for the low magnification case, which is due to the larger ROC (flatter mirror) required to focus the beam, where errors in the shape of the mirror become significant,

compared with the low magnification case where more stress is applied to the surface of the mirror.

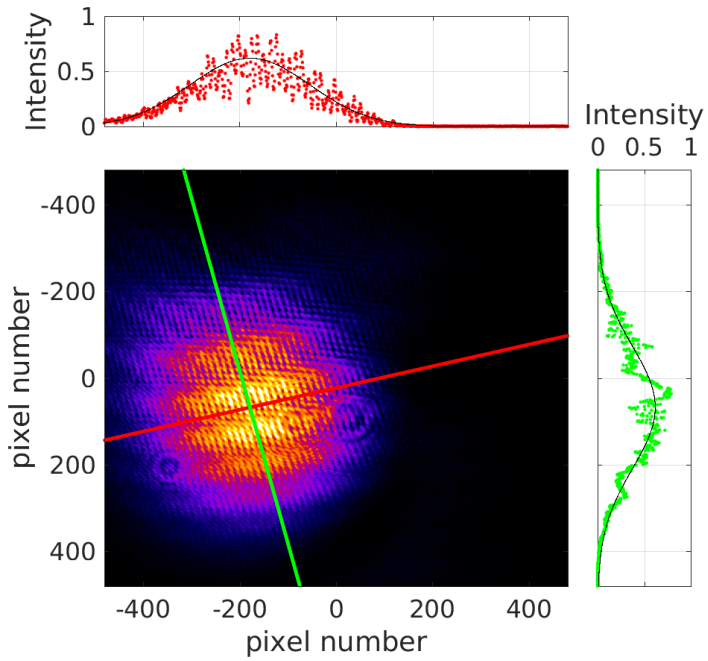

Figure 6.12: Focused HeNe laser spot with KB microscope with $p = 1.3$ m, $q = 5.00$ m and $\phi = 2°$. Measured focus spot size in this image is 2.32 mm in the minor axis and 2.62 mm in the major axis to the $1/e^2$ diameter.

6.2.3 Grazing angle for betatron radiation

The KB has been tested as part of preparation for an experiment to measure the grain orientation of metal alloys using betatron radiation. The grazing angle of the mirrors is set to $\phi = 7.077$ mrad, which is the optimum value for 10 keV photons (see chapter 6.1.1), which was the expected value based on previous experiments in the ALPHA-X laboratory. The position of the HeNe laser and CCD camera are set up such that $p = 1.27$ m, $q = 1.65$ m ($M = 1.30$), $ROC = 203$ m and deviation angle $\theta = 1.15°$.

From equation 6.4, the spot size for these settings is 0.64 mm for the minor axis and 0.85 mm in major axis. From figure 6.13 it can be seen that, after spot optimisation, the best achievable spot size is about a factor of 2 larger than expected in both the

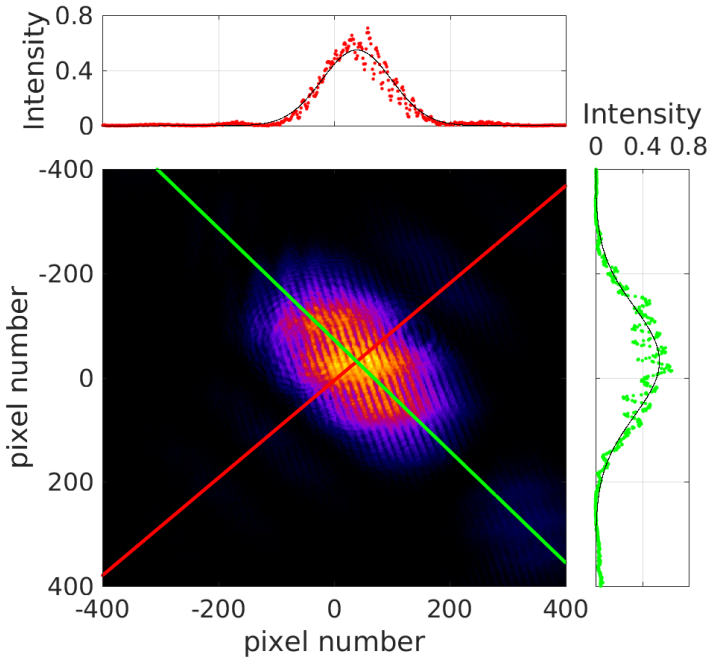

Figure 6.13: Focused HeNe laser spot with KB microscope set with $p = 1.27$ m, $q = 1.65$ m and $\phi = 7.077$ mrad. Measured focus spot size in this image is 1.12 mm, along the minor axis and 1.95 mm along the major axis to the $1/e^2$ diameter.

minor and major axis of the laser, where the measured spot diameters are 1.12 mm in the minor axis and 1.95 mm in the major axis. For shallow grazing angles, the radius of curvature becomes large according to equation 6.2, which is over 200 m, in this case. This is similar to the high magnification case where imperfections in the shape of mirrors become very important. The shape of the mirrors fully relaxed and connected to the benders has not been measured.

6.3 First x-ray focus tests with the Kirkpatrick-Baez microscope

The Kirkpatrick-Baez microscope was moved and installed on the ALPHA-X beamline in bunker C of SCAPA, a schematic of which can be seen in figure 6.14. Laser pulses with energy ≈ 1.0 J and pulse duration 35 fs is focused to a spot diameter of ≈ 50 µm.

The focal position of the laser is set to ≈ 4 mm above the 2 mm gas jet, with a gas backing pressure of 50 bar, giving a plasma density of 1.8×10^{19} cm^{-3} as shown in figure 3.11. The accelerated electron bunch from self injection into the plasma wake is deflected away from the laser axis by the 0.7 T bending magnet inside the main acceleration chamber. The direction of the deflection of the electrons is opposite to the direction where the betatron radiation is deflected after passing through the KB, to reduce noise on the Andor Newton camera. During data collection runs, the laser is blocked by 2.4 µm of aluminium directly before the KB, which protects the mirrors, and a further 1.6 µm of aluminium in the filter carousel that blocks any stray light from reaching the CCD camera. Both filters could be removed away from the beamline while under vacuum, so that alignment with the HeNe and 800 nm lasers could be performed.

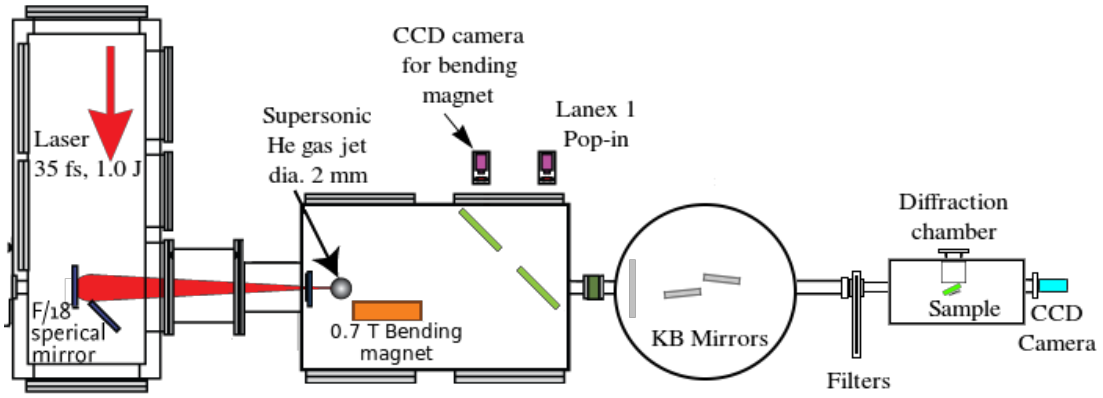

Figure 6.14: Schematic of ALPHA-X beam line configured for x-ray diffraction experiments with Kirkpatrick-Baez microscope 1.25 m from the gas jet and 1.70 m from the CCD camera beyond the sample for monitoring the focal spot of the betatron radiation.

The mirror grazing angle is set to 12.54 mrad, which is optimised for 5 keV photons, chosen after measuring the spectrum of the betatron radiation (see chapter 7). The beamline is set up for a Laue diffraction experiment which requires the focal spot of the betatron radiation to be at least as small as the grain size of the alloy samples. Therefore, the low magnification configuration of the KB is chosen to keep the focal spot close to the betatron source size. The centre point between the mirrors is $p = 1.25$ m

from the gas jet and $q = 1.70$ m from the CCD camera, which is placed beyond the sample and used to monitor the focal spot of the betatron beam ($M = 1.36$). The calculated spot diameter to $1/e^2$ is 15.4 µm and 12.0 µm in the major and minor axes, assuming a 10 µm source size for the betatron radiation. Alignment of the grazing angle of the mirrors is performed using the HeNe laser, which co-propagates with the 40 TW laser, using the method described in 6.1.2. The CCD camera is positioned to overlap with the focal spot from the KB using the 800 nm laser in low power alignment mode because placing the CCD at the HeNe focus resulted in the x-ray beam missing it. The focus of the KB is then optimised using only the 800 nm laser because it focuses above the gas jet, which defines a source to image that is consistent with the origin of the x-rays.

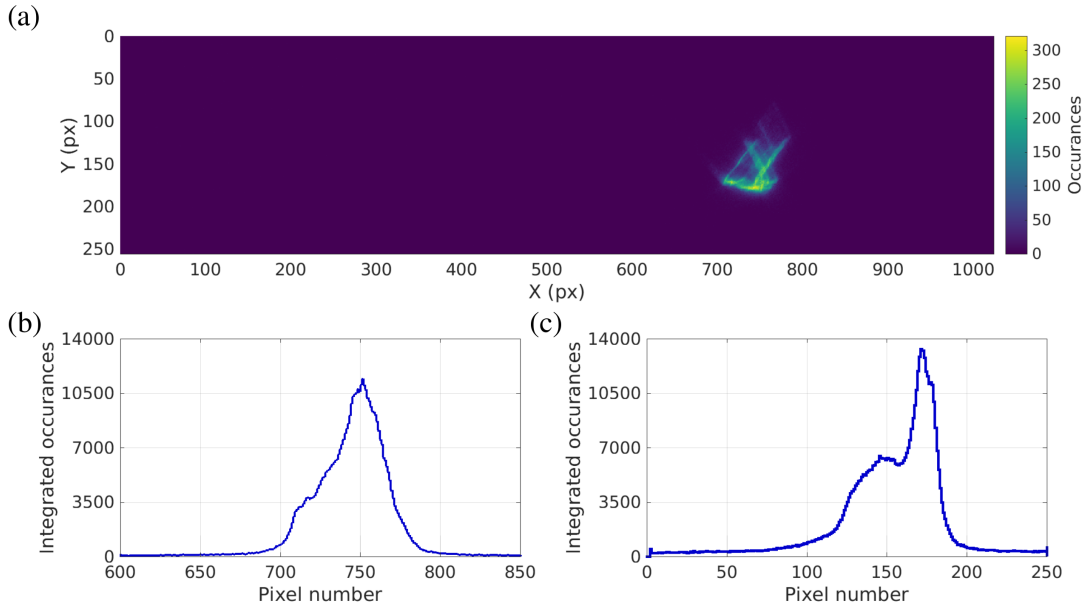

Figure 6.15: (a) Unoptimised betatron x-ray focus spot from KB microscope using single photon counting analysis with summation of 500 laser shots. The grazing angles of KB mirrors are set for 5 keV photons, with $p = 1.25$ m, $q = 1.70$ m and $\phi = 7.077$ mrad. Laser is blocked with total of 4 µm of aluminium. (b) Integrated number of occurrences in the x axis. (c) Integrated number of occurrences in the y axis.

Figure 6.15 shows the focused betatron radiation beam from the Kirkpatrick-Baez microscope. Because the number of photons detected per shot is low the image is a

result of the accumulations of 500 laser shots analysed with a single photon counting script described in chapter 7. The spot size of the x-rays here is large, $\sim 2600 \times 2600$ µm (100×100 pixels), but this image has been recorded without any optimisation of the mirror curvatures after rough alignment with the 800 nm beam. The intensity distribution at the focus shows wings in addition to the main spot, which is evident in a single shot as demonstrated in figure 6.16. This demonstrates that the wings are not artefacts from the summation of individual laser shots. The shape of the spot remained the same over all data collection runs over the course of an afternoon for a range of different thicknesss of aluminium filters, suggesting that the mirrors are the source of the astigmatism and not the source itself. This non-uniformity in the betatron focus may be due to a twist in one or both of the mirrors. Further testing and optimisation of the KB with betatron radiation were not possible because of laser problems that prevented further experiments.

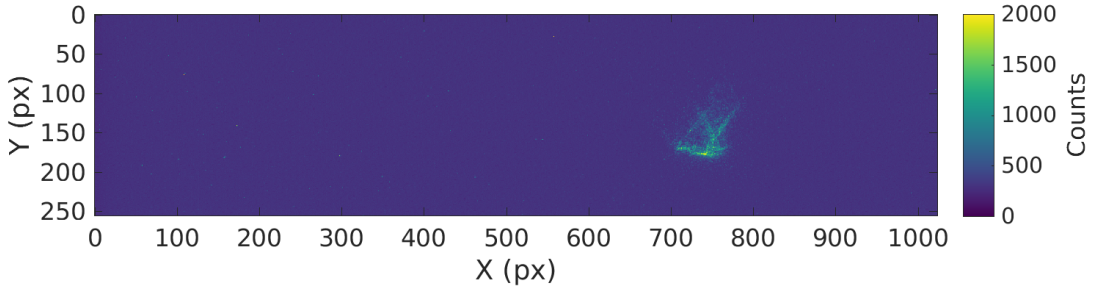

Figure 6.16: Single shot image of x-ray focus corresponding to figure 6.15 showing presence of wings.

6.4 Discussion

The design and testing of a Kirkpatrick-Baez microscope acquired by the SCAPA laboratory is presented. This is a fully adjustable system where the mirror grazing angle and radii of curvature allows both low and high energy photons to be focused over a range of focal lengths, so that the focal spot size of the radiation beam can be selected for a particular application. A simple alignment method is presented, based on basic geometric arguments that allow the small ($< 2.5°$) mirror grazing angles to be accu-

rately set by measuring the separation between the four spots that the Kirkpatrick-Baez microscope produces. The method, as presented, is limited by the assumption that the two mirrors have equal grazing angles, which results in an elliptical focal spot. However this could be extended for two different grazing angles that allows the system to be solved for a circular focal spot shape.

A method of determining the optimum mirror grazing angle is evaluated by finding a balance between the aperture and reflectivity for a target photon energy. Several examples are given for photons in the range of the expected betatron radiation for the available laser systems in the SCAPA facility, and an approximate scaling equation is calculated. Because reflectivity of most materials changes with grazing angle, and the photon energy spectra contain edges and oscillations as seen in figure 6.5, specific target energies required for a particular experiment should be checked individually, rather than relying entirely upon the scaling identified.

The KB microscope has been tested with a HeNe laser for three cases: large grazing angle for XUV photons in a low and high magnification configuration in addition to a shallow grazing angle, optimised for hard x-rays in a low magnification mode. When the mirrors are set for XUV radiation it is found that the KB performed better (closer to expected value) in the low magnification case, requiring a smaller radius of curvature and therefore more force applied to the mirror. It has also been found that the measured focal spot is further from the calculated value when the mirrors are set for photons with energy 10 keV, compared with the large grazing angle case. The difference between the measured and calculated values increases with increasing radius of curvature, suggesting that this is the limiting factor in the KB's ability to focus light.

From the solutions to equation 6.2 in figure 6.17, it can be seen that for a given focal length (example of 2 metre used), a larger radius of curvature is required for x-ray photons than for XUV photons, therefore a flatter mirror is required to focus higher energy photons. It can be concluded that the focusing of the radiation is limited by the flatness of the mirrors. For large radii of curvature, errors in the shape of the mirror when not under stress are more significant than when applying a large stress to produce small radii of curvature. Further testing is required to measure the mirror flatness after

gluing to the holders and to test the shape of the mirrors when under stress. The effect of errors in the mirror flatness should also be investigated both theoretically and experimentally.

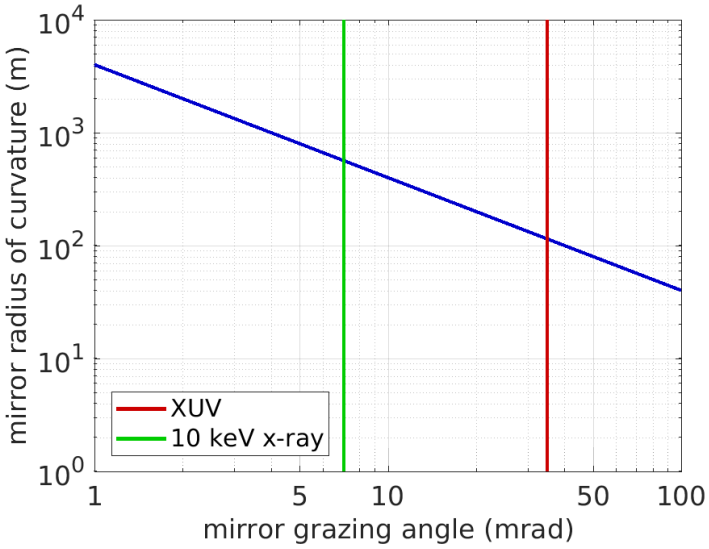

Figure 6.17: Calculated mirror radius of curvature (ROC) using equation 6.2 for 2 m focal length between grazing angles of 1 to 100 mrad. The ROC required for XUV radiation with a grazing angle $\phi = 35$ mrad is 114.3 m (red line) and a ROC of 565.0 m is required for 10 keV x-ray photons, where the optimum grazing angle is 7.077 mrad (green line).

Adjusting the two motors, as a pair, to change the ROC of a single mirror is performed to study the change in spot size with stress applied and investigate the reproducibility of the mirror curvature. It is found that the spot size of the HeNe laser does not change systematically and the two mirrors behave differently. The reproducibility and hysteresis of the motor position is also poor, as returning to the initial position does not return the spot back to its initial size, and it changes the position of the focal spot on the CCD camera. The cantilever arm of the KB bender requires further characterisation and a change in the design should be considered because it was discovered during testing that the motor pops out of the indent drilled into the bender, which is shown in figure 6.18. Therefore, the motor doesn't apply the same change in force for a given number of motor steps moved. A possible improvement is to machine a trench

rather than a circle in the cantilever bender to help the motors push on the mirror consistently.

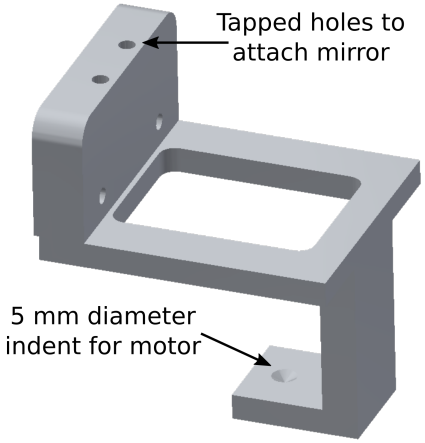

Figure 6.18: CAD drawing of cantilever bender isolated from mirror mount (figure 6.3), showing 5 mm circular indent for motor to push upon. When applying stress to the mirror, the motor slips out of this indent causing loss of control of the focus spot size.

A test of the ability of the KB to focus betatron radiation in preparation for a x-ray diffraction experiment has been performed. However, without an opportunity to optimise the Kirkpatrick-Baez microscope, a focal spot of around $\sim 2.6 \times 2.6$ mm is obtained, which is very far from the 12.0×15.4 µm expected from the close to 1:1 imaging system. However, it is sufficient for targeting a single grain of the course metal alloy sample used in the experiment.

Chapter 7

Measurement of the Betatron spectrum

In this chapter, measurement of betatron x-ray spectra emitted from a laser wake-field accelerator, using a photon counting method is presented. These measurements have been recorded as part of the commissioning run of the ALPHA-X beam line at SCAPA. A second method is also presented, the Ross pairs technique, which is based on measuring the transmission difference of a series of filters.

7.1 Single photon counting

One method for measuring the spectrum of an x-ray source is single photon counting using a pixelated CCD camera [203, 204]. The charge deposited by a photon incident on a pixel of a CCD detector is proportional to the energy of that photon. Therefore, by measuring the charge in a pixel, the energy of the incident photon can be recovered. For the photon counting method to be accurate, the flux onto the CCD sensor needs to be low, such that only a single photon is detected in a given pixel, and only a small fraction of the total number of pixels detect photons so that effects due to charge leaking between pixels for high photon energy does not effect the measurement of the photon energy. To account for the electron cloud from a high energy photon spreading between a number of pixels, the total charge of a photon is found by summing over the central

pixel plus a number of the surrounding pixels [205, 206]. Since only a small number of pixels can be used in a given laser shot, the spectrum must be built up over a number of laser shots however this method has the advantage of not making any assumption about the shape of the spectrum in the analysis.

7.2 Calibration of the CCD camera

The Andor iKon-M camera described in chapter 3.3.3 has been calibrated for single photon counting using americium-241 (^{241}Am), chosen because it has x-ray emission peaks in the range where betatron radiation is expected. The ^{241}Am sealed source, with activity 37 kBq, is placed 15 mm from the CCD sensor of the camera and a 75 µm thick layer of Mylar ($C_{10}H_8O_4$) is used to block alpha particles from reaching the detector. Mylar is chosen due to its low absorption of x-ray photons with energies greater than 1.5 keV. The CCD camera and sealed source are placed inside a vacuum chamber at a pressure of 8×10^{-5} mbar, to replicate experimental conditions and allow the camera to be cooled to -70°C to reduce noise from dark current. A camera shutter duration of 3 s gave on average 33.8 photons per shot on the CCD sensor, comfortably in the single photon counting regime for a detector containing 1024×1024 pixels. $12,000$ images are recorded, containing in total $405,290$ photons.

A photon counting script has been developed to analyse the images and reconstruct the spectrum of the x-rays incident on the CCD sensor. It is first used to calibrate the photon energy response of the CCD camera and then used to measure the critical energy of the betatron radiation presented in chapter 7.3. When cooled to -70°C with no source irradiating the sensor, each pixel on the camera records around 300 counts with a normal distribution, which is subtracted as a background in the first stage of the analysis. A unique value for the background is chosen for each image by creating a histogram of the values of every pixel in the image, and the background is taken to be the peak of that histogram. A histogram of the signal in a typical image recorded during the camera calibration, in the range of camera background, is shown in figure 7.1, which peaks at 292 counts. Over all calibration images, the distribution of the

background signal peaked at an average value of 292 counts and varied between 288 and 295 counts.

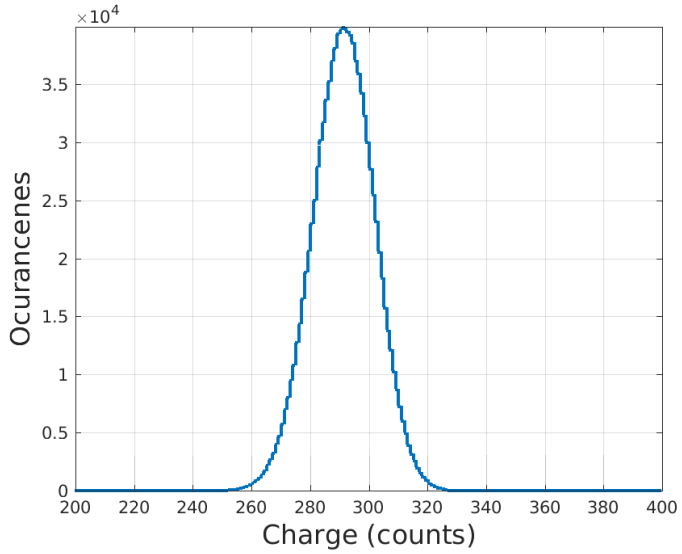

Figure 7.1: Normalised histogram of background signal of image recorded in the Andor camera calibration run. The histogram peaks at 292 counts per pixel.

After background subtraction, the script decides if the charge deposited in a pixel should be considered as a photon or whether it is empty. The script starts by identifying the pixel containing the highest number of counts in the image. To account for charge leaking from one pixel into another, the 24 surrounding pixels are summed together with the central pixel and the total number of counts is taken to be the charge created by the photon. All pixels used then have their value set to zero so that the same pixel is never counted twice. The process is repeated until the brightest pixel left in the image has a value that falls inside the background level of the camera. The spectrum of the ^{241}Am sealed source is then reconstructed by creating a histogram of the number of times a pixel contains a given charge. The ^{241}Am spectrum used to calibrate the Andor iKon-M CCD camera is shown in figure 7.2(a) where the peaks are marked and the corresponding calibration curve is shown in 7.2(b).

The decay of the ^{241}Am results in the emission of photons with energies 13.9, 17.7, 20.7, 26.3 and 59.5 keV. A further peak is visible at 48.3 keV from the Compton edge

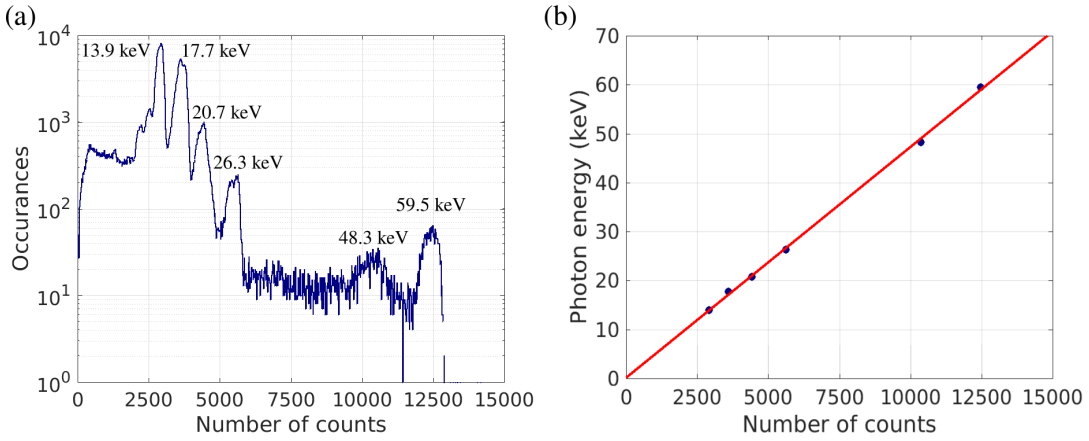

Figure 7.2: (a) Reconstructed spectrum of ^{241}Am sealed source using single photon counting with Andor iKon-M CCD camera. (b) Linear fit of peaks of ^{241}Am spectrum for energy axis calibration of camera, where the fit is described by the expression given in equation 7.1.

of photons with energy 59.5 keV. The number of counts where each of these peaks are found are used to create a calibration curve for the CCD sensor. The energy axis calibration for the Andor iKon-M camera is shown in figure 7.2(b) and given by

$$E_{\text{ph}}[\text{keV}] = 0.005 \times \text{counts} + 0.091. \tag{7.1}$$

7.3 Measurement of the betatron spectrum

7.3.1 Betatron critical energy

After moving from the old ALPHA-X laboratory to the SCAPA facility, the accelerator and x-ray source have both been re-characterised as part of a commissioning campaign with the aim of preparing and optimising the beamline and laser for an imminent Laue diffraction experiment. The camera is mounted directly on the axis of the laser with the laser, 3.18 m from the gas jet. The laser is blocked by 1.6 µm of aluminium and 55 µm of Mylar which prevents a sufficient proportion of the total betatron radiation from reaching the CCD camera to be in single photon counting regime.

A run of 200 laser shots is repeated several times over the course of a day to

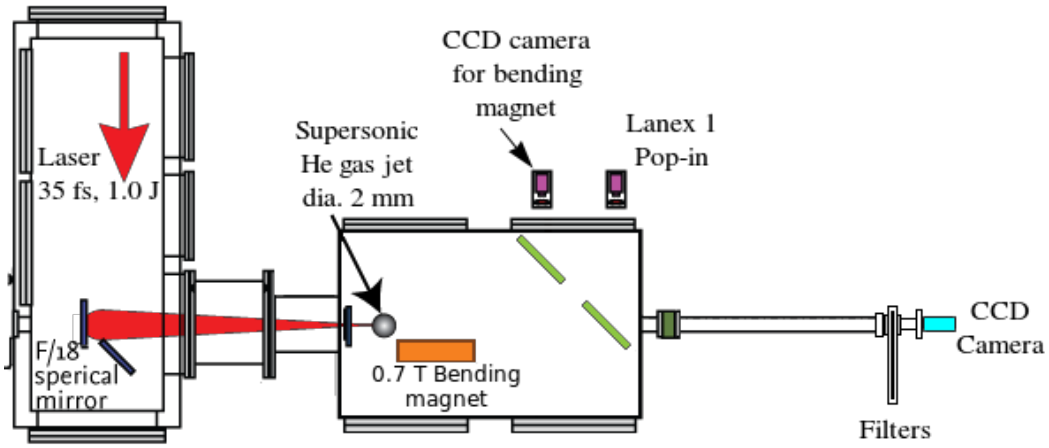

Figure 7.3: ALPHA-X beamline configured for measuring the spectrum and critical energy of betatron radiation from the laser wakefield accelerator.

determine the critical energy of the betatron radiation and to check how stable the source is in terms of the spectral shape, critical energy and the number of photons emitted. In each case, the laser energy is ≈ 1 J, pulse duration 35 fs and spot diameter ≈ 50 µm. The laser is focused 4 mm above the helium gas jet with backing pressure 45 bar. Electrons accelerated by the plasma are deflected away from the direction of laser propagation axis by the 0.7 T permanent magnet and directed towards a Lanex screen to estimate their energy. An optical fibre with 5 mm diameter collimating lens of focal length 10 mm is placed behind the gas jet to collect backscattered laser light and directed it towards a Ocean Optics USB spectrometer, so that the plasma density can be measured from the frequency separation between the laser, Stokes and anti-Stokes peaks that are observed. The same photon counting script as for the camera calibration is used to analyse the betatron spectrum data, where an average of 315 photons are detected by the CCD in a single laser shot. A histogram of the number of occurrences for each charge collected within a pixel is calculated, then the calibration curve from equation 7.1 is applied prior to a least squares fit of a synchrotron spectrum to find the critical energy of the betatron radiation using the function

$$\frac{d^2I}{dEd\Omega} = A\left(\frac{E_{\mathrm{ph}}}{E_c}\right)^2 K_{2/3}^2\left(\frac{E_{\mathrm{ph}}}{E_c}\right), \tag{7.2}$$

where $A = 3N_\beta e^2\gamma^2/(2\pi^3\hbar c\epsilon_0)$ is the amplitude of the fit, E_{ph} is the energy of the photon and E_c is the critical energy of the betatron spectrum. The results from three runs of 200 laser shots is presented in figure 7.4 suggests that the spectrum has critical energy ~ 3 keV.

Due to the low transmission of the filter materials, all photons less than 2 keV should be considered as noise and have been excluded from the fitting to the betatron spectrum. Similarly, photons with energy greater than 50 keV have also been excluded, since the quantum efficiency of the camera becomes poor at high photon energies (see figure 3.14). Due to the filter transmission being so poor at less than 2 keV, the spectrum cannot be conclusively attributed to betatron radiation, although the shape of the spectrum is characteristic of what would be expected from betatron radiation. One possibility for observing photons with an energy of a few keV could be bremsstrahlung generated by electron beam that has travelled through the walls of the vacuum chambers, producing photons which reach the sensor of the CCD camera. The choice of filters were designed for higher photon energies so measurements will have to be repeated when the electron energy is higher. Previously in the ALPHA-X laboratory with the 40 TW laser, betatron radiation with critical energy up to 20 keV has been detected from electrons over 150 MeV [207, 208].

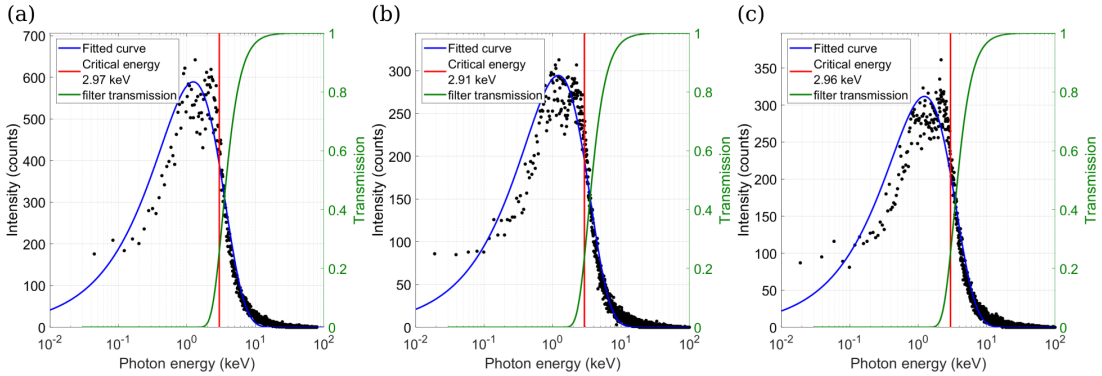

Figure 7.4: Three runs of 200 laser shots measuring radiation spectrum with the single photon counting method. The spectra correspond to an average of (a) 318, (b) 304 and (c) 320 photons per shot. The critical energy in each case is marked in red with the value given in the plot legend and the green trace shows the transmission of the 1.6 µm of Al plus the 55 µm of Mylar used to block the laser.

7.3.2 Plasma density

To confirm that the measured value of the betatron radiation is reasonable, the expected critical energy was calculated. To do this the plasma density and electron energy must be known. The plasma density is measured from the backscattered light from the laser plasma interaction. Light is scatted in the backwards direction at the laser frequency in addition to the laser frequency, shifted by an amount equal to the plasma frequency due to Raman scattering. This scattering creates two satellites around the laser frequency, which appear at the Stokes and anti-Stokes Raman frequencies given by

$$\Delta\omega = \omega_{S/aS} = \omega_0 \mp \omega_p, \tag{7.3}$$

where ω_S is the Raman Stokes frequency, ω_{aS} is the Raman anti-Stokes frequency, ω_0 is the laser central frequency and ω_p is the plasma frequency. The plasma density can then by found using $n_e = \Delta\omega^2 m_e \epsilon_0 / e^2$. A Stokes shift is a loss in photon energy as it scatters off plasma electrons, resulting in a lowering of the photon frequency, while the anti-Stokes shift is due to a gain of photon energy. An optical fibre placed ≈ 4 cm behind the gas jet at an angle of 5° collects light backscattered from the plasma and transports it to an Ocean Optics Flame-T spectrometer through an optical fibre to measure the spectrum. Since the spectrometer has no trigger cable, a 2 s acquisition time is used to match the laser repetition rate to collect a signal over the entire duration of the shot. The time averaged plasma density is therefore measured. A typical backscattered spectrum is shown in figure 7.5, for a gas backing pressure 45 bar, where the Stokes and anti-Stokes peaks can clearly be seen. The plasma density is calculated for the Stokes and anti-Stokes peaks for all shots and the average plasma density, combining the data from the Stokes and anti-Stokes peaks, at 45 bar helium gas backing pressure is $(1.71 \pm 0.01) \times 10^{19}$ cm^{-3}. There is a slight difference in calculated plasma density between the two cases, where the average Stokes density is 1.75×10^{19} cm^{-3} and the average anti-Stokes density is 1.67×10^{19} cm^{-3}.

Computational fluid dynamics simulations using ANSYS Fluent, courtesy of Dr Enrico Brunetti, for the 511 nozzle show that the plasma density is 1.74×10^{19} cm^{-3}

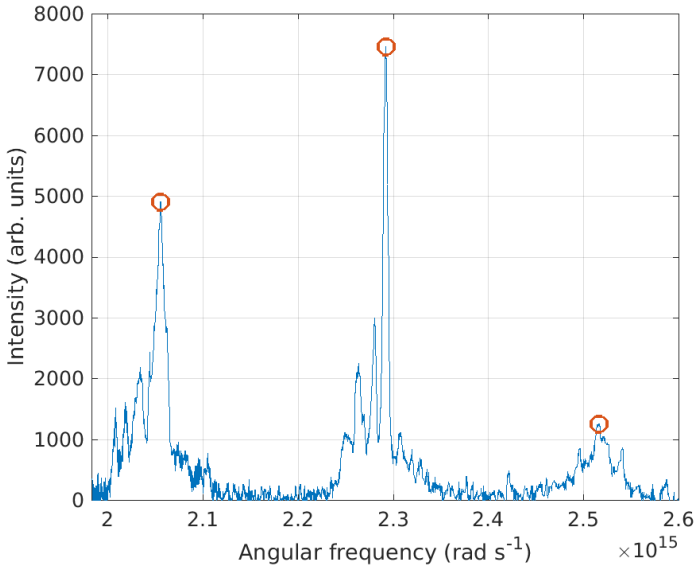

Figure 7.5: Example of a backscattered spectrum showing the Stokes and anti-Stokes satellites around the central laser frequency. In this image, the Stokes shift gives a plasma frequency of 1.76×10^{19} cm^{-3} and the anti-Stokes shift gives a plasma frequency of 1.58×10^{19} cm^{-3}.

half a millimetre from the centre of the nozzle when the laser is 4 mm from the top of the nozzle. The measurement of the plasma density is consistent with the simulated value. The simulated plasma density profile for the 45 bar helium backing pressure used in the experiment is shown in figure 3.11(b).

7.3.3 Electron energy

The electron energy is measured using a permanent magnet spectrometer placed inside the main chamber, as described in chapter 3.3. During the commissioning run of ALPHA-X in the SCAPA laboratory, electrons are only observed on the low energy window of the spectrometer. The average electron energy is (52.8 ± 0.7) MeV with a peak value of 70.5 MeV. The electron spectra typically have a high energy spread with electrons between 38 and 70 MeV and a high divergence with electrons spread over the majority of the vertical axis of the screen. Representative electron spectra recorded simultaneously with the CCD camera to measure the betatron spectra are presented in

figure 7.6.

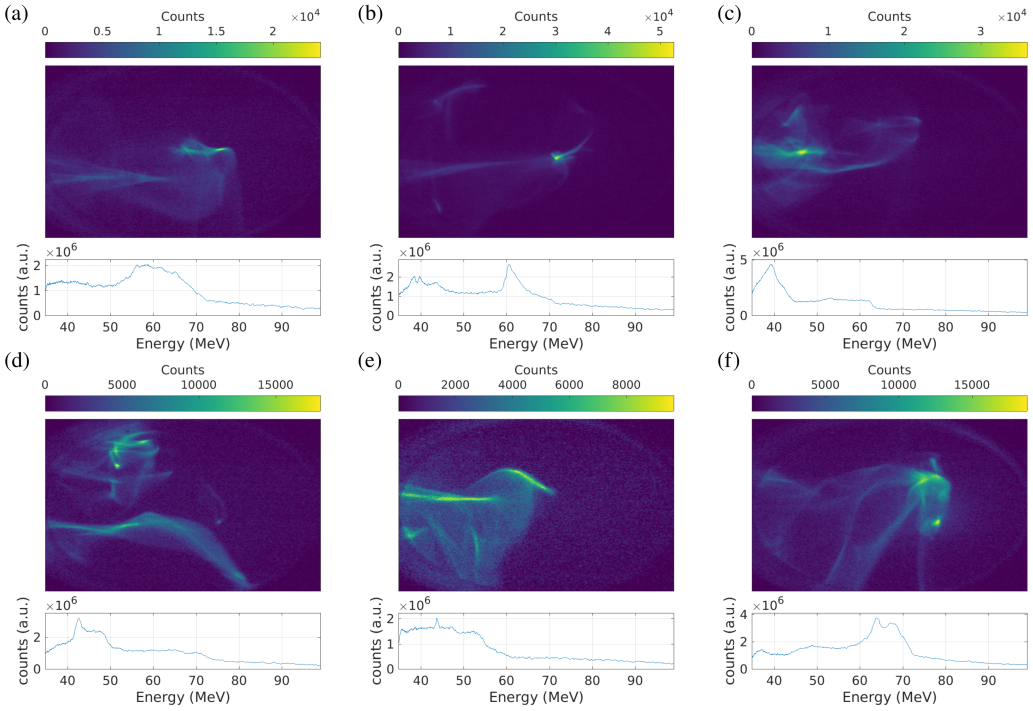

Figure 7.6: Typical example electron spectra recorded with 0.7 T bending magnet recorded simultaneously with betatron spectrum data with helium gas backing pressure of 45 bar. The spectrum in each image peaks at (a) 58, (b) 61, (c) 39, (d) 43, (e) 44, (f) 64 MeV.

The measured plasma density from chapter 7.3.2 of 1.71×10^{19} cm^{-3} and electron energy 52.8 MeV give the measured betatron critical energy of 2.97 keV, using equation 2.46, for a betatron radius of 3.05 µm showing that photon counting correctly measures the critical spectrum.

7.4 Design of Ross pair filter wheel

Another simple diagnostic for measuring the betatron critical energy is the Ross pair technique [209–212], which enables spectral measurements using single photon counting to be checked. The Ross pair technique is based on a differential measurement of the x-ray photon density transmitted through similar bandpass filters composed of pairs of thin metal filters that have K edges close to each other. A bandpass transmission is

simply calculated from the difference between signals measured through each filter. The full radiation spectrum can be reconstructed using a number of filter pairs that have K edges spread over the expected bandwidth of the radiation spectrum. This method does not require being in the single photon regime so very thin filters can be chosen with high transmission such that the spectrum can be measured in a single shot which cannot be achieved using photon counting. To illustrate this technique, a single filter pair of cobalt (Co) and iron (Fe) is considered for clarity, prior to discussing the whole filter set. Iron and cobalt have similar response to x-rays to each other because of they are adjacent to each other in the periodic table. They have x-ray transmission functions that very similar apart from close to their the K edges. Iron has its K edge at 7.11 keV and cobalt at 7.71 keV. The x-ray transmission spectra are calculated using XOP [183], and optimised so that the x-ray transmission away from the K edges are well matched considering the commercially available filter thicknesses. Figure 7.7(a) shows the filter transmissions for the two chosen filter thicknesses of 10 µm and 12.5 µm for cobalt and iron, respectively. The difference between the two filter transmissions is calculated to giving the net transmission within a small spectral range from a CCD camera image. The bandpass feature between 7.11 and 7.71 keV shows that the majority of the signal difference occurs in this region with, a few percent error due to a small mismatch in the regions where the transmission is not matched away from the K edges.

To find the critical energy of the betatron spectrum, 10 filters are chosen to create 5 pairs, which are summarised in table 7.1, with the corresponding transmission plots shown in figure 7.8. The chosen filter material covers the range from 1.5 to 19 keV, optimised for the 7 to 20 keV region, where the betatron spectrum is expected for the 40 TW laser. The filter pairs have a total range from 3 keV to around 25 keV, beyond which the measurement becomes less reliable due to the need to extrapolate from the distribution of the tail of the spectra. The thickness of each filter is chosen to ensure that the peak transmission of the differences between the filters have similar values so that only a small correction value is required to adjust for the intensity differences between measured points. Other filter pairs were considered including a Pd/Ag pair [212] which tests the spectrum at 24.9 keV which was rejected because the spectral

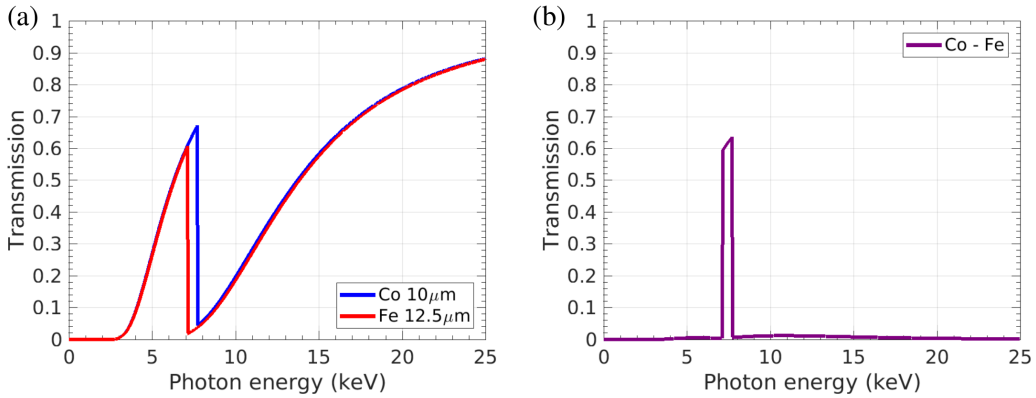

Figure 7.7: (a) Transmission curves for iron (red) and cobalt (blue) for the chosen thicknesses using the Ross pair technique to measure the intensity of the spectrum between 7.11 and 7.71 keV. (b) Difference between x-ray transmissions for Co and Fe where 72% of the signal is contained within the two k edges.

intensity was expected to be low in this region. A Ti/Pd pair [211] tests the spectrum at $\approx$ 4.5 keV but the palladium has a second edge at 24 keV without a corresponding close edge from the titanium so it would not be clear in an experiment if the difference in intensity arises from photons at 4.5 or 24 keV.

	Filter material	K edge (keV)	Thickness (µm)	Signal between edges
Pair 1	Mylar Al	- 1.56	75.0 6.0	62%
Pair 2	Ti V	4.97 5.47	15.0 10.0	84%
Pair 3	Fe Co	7.11 7.71	12.5 10.0	72%
Pair 4	Cu Zn	8.99 9.66	9.0 10.0	84%
Pair 5	Nb Mo	18.99 20.00	25.0 20.0	91%

Table 7.1: K edge and thickness of each of the filters used to make up the 5 filter pairs for measuring the betatron spectrum.

If the intensity of the radiation is evenly distributed across the sensor then background subtraction is not required because the contribution from scattered light through the two filters is automatically subtracted. Experimentally, a spectrum measurement

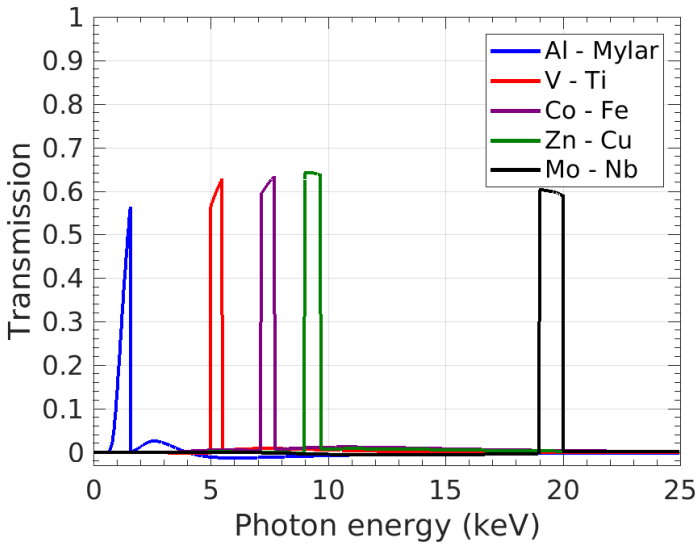

Figure 7.8: Differences in filter transmissions for each of the filters in table 7.1.

made with Ross pair filters can be made with the beamline configured as shown in figure 7.3 with the Ross pair filters in the position marked "Filters" on the figure. The 5 filter pairs are arranged adjacent to one another, and are illuminated in a single shot so that the spectrum critical energy can be found for individual laser shots. The image analysis script finds the total signal inside each filter, within the same area, and then calculates the difference in the intensity between each filter pair. These intensity values are paired with their corresponding photon energies where the mean value of the high transmission region between the k edges is used. The 5 points are then used to find fit the synchrotron spectrum to establish the betatron critical energy using the same least squares method previously described for the single photon counting analysis. To test the fitting routine used in the analysis script and to demonstrate that the Ross pairs method will work for the chosen pairs, 5 points corresponding to the expected intensities for each filter are calculated from equation 2.45. Results for the three critical energies are presented in figure 7.9, where in each case the fit returns the same critical energy as the calculated value.

During the commissioning run of ALPHA-X, a Ross pair measurement of the betatron spectrum has been attempted. An image from the Andor iKon-M CCD camera,

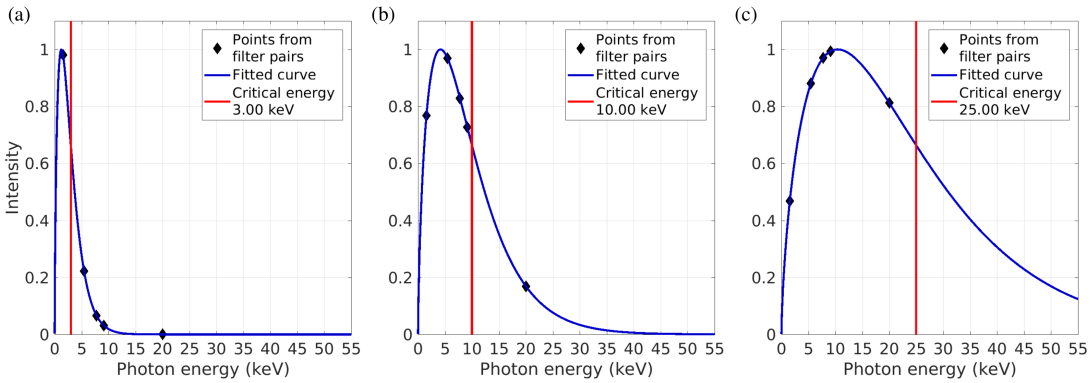

Figure 7.9: Test of Ross pair analysis script using calculated values for the intensity of each point corresponding to a filter pair. Points are calculated from the betatron spectrum for (a) 3 keV, (b) 10 keV and (c) 25 keV.

positioned 1.52 m from the gas jet, is shown in figure 7.10(a) for the same laser and plasma parameters as described in chapter 7.3.1. The two layers of Zn used to reach the correct thickness can be seen. To help correctly identify each of the filters during analysis, the molybdenum (Mo) is cut into a triangular shape. The order that the filters are arranged in is recorded so that the Mo and Zn could be used as reference points to identify the others. The filters are sandwiched in between a layer of Mylar (75 µm) and aluminium (1.6 µm) to support them and to fully block the laser which protects the CCD camera from damage. Calculations of the x-ray transmission using XOP for the stack of three filters show that this only has a small impact on the transmission functions used to calculate the differences between filters, which make up a pair for photon energy > 1 keV. However, the difference between the filters transmission becomes significant at low photon energies. As a consequence of supporting the filters in this way the aluminium/Mylar pair at ~ 1.5 keV is lost. Images are analysed using the method described above considering a 60×60 pixel (0.78×0.78 mm) region of interest at the centre of each chosen filter. However, it is not possible to determine the critical energies, as some differential spectra produced negative values, in part, because the photon energy is low. This is confirmed by the measurements from single photon counting that show that the betatron critical energy is < 3 keV. A non-uniform profile can be seen across the area of the CCD image which may also contribute to some filter

pairs giving the negative result. It is expected that this method will work well for measuring the betatron spectra when the laser and accelerator are properly optimised and the electron energies have been increased or when experiments with the 350 TW.

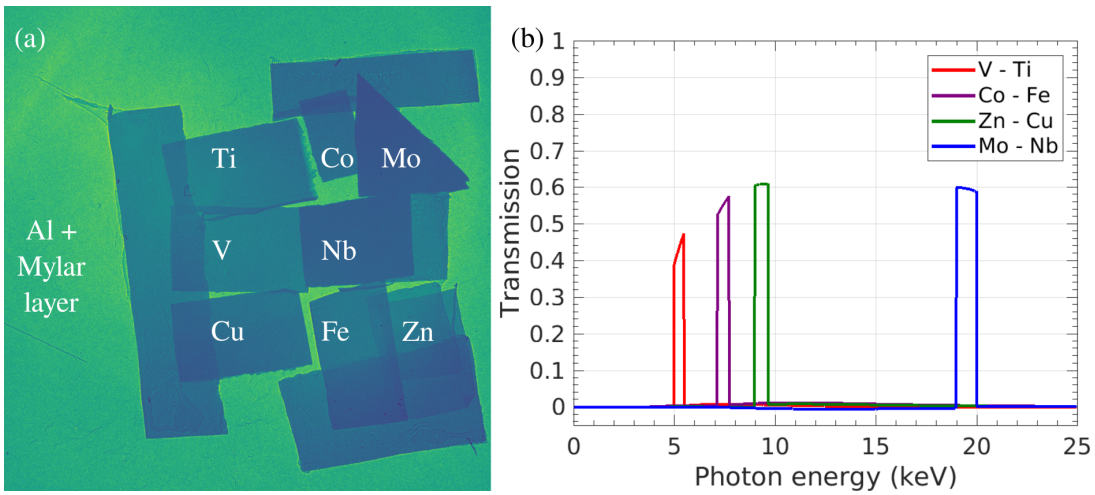

Figure 7.10: (a) Image from CCD camera of illuminated Ross pair filter illuminated by betatron radiation (b) Transmission differences for filter pairs taking into account the aluminium and Mylar layer that supports the filters.

7.5 Discussion

A single photon counting technique with an x-ray CCD camera, where the flux on the detector is sufficiently low for the charge deposited in a pixel to be measured and directly associated with the energy of the incident photon, was used with the aim to measure the x-ray spectrum arising from betatron oscillations of the high energy trapped electrons in the plasma wake. The camera was calibrated using an ^{241}Am radioactive source that has x-ray peaks in the spectral region coinciding with that of the betatron radiation, as shown in figure 7.11, so that an accurate calibration is obtained. However, the commissioning run of the new ALPHA-X beamline at SCAPA gave electron energies that are much lower than expected, 35 to 70 MeV, resulting in a lower betatron critical energy. The calibration therefore had to be extrapolated back to a much lower photon energy than that covered by the calibration source, therefore the energy calibration of the camera is uncertain at lower photon energies. To improve the camera calibration

additional calibration sources with emission peaks from a few hundred electronvolts up to ≈ 15 keV, would reduce the uncertainty in this part of the spectrum. The need for an additional calibration source is shown in figure 7.11 where the position of the spectral peaks in ^{241}Am is compared to the calculated betatron spectrum for the measured electron energy and plasma density. Despite this, a critical energy of 3 keV has been measured, which is consistent with the measured plasma density (1.7×10^{19} cm^{-3}) and electron energy of (≈ 60 MeV). However, the transmission of the aluminium and Mylar stack used to block the laser has poor transmission for energies less than 2 keV so it is not possible to conclusively attribute the observed photons to betatron oscillations of the electrons trapped in the plasma wave. In the previous ALPHA-X laboratory, electrons have been accelerated to between 130 and 180 MeV using the same laser system. This produced emission with a betatron critical energy of around 15 keV [207, 208].

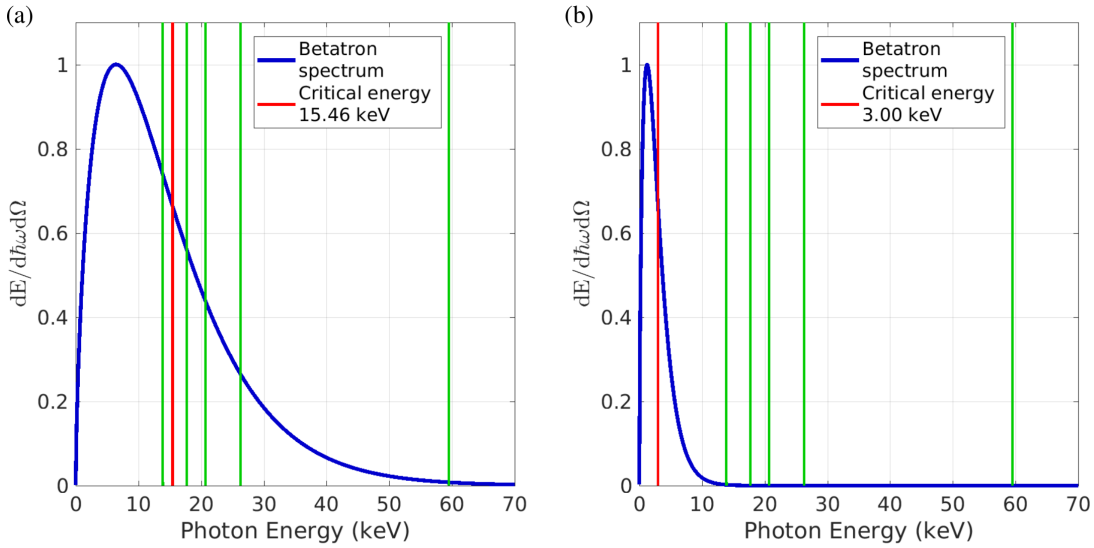

Figure 7.11: (a) Calculated betatron spectrum with expected energy of $E = 150$ MeV electrons, $r_\beta = 2.0$ µm and $n_e = 1.70 \times 10^{19}$ cm^{-3} gives a critical energy marked in red. (b) Calculated spectrum with critical energy 3 keV matches the experimentally obtained value. The x-ray peaks of the ^{241}Am spectrum are marked in green.

The plasma density is determined by measuring the spectrum of Raman backscattered laser light. The interaction between the plasma wave oscillating at the plasma

frequency and the laser electromagnetic wave results in backscattered radiation with a spectrum at the laser frequency (Thomson scattering) and two satellites that have frequencies up-shifted and down-shifted by the plasma frequency (Raman scattering). The backscattered light is collected by a mirror and focused into the entrance face of an optic fibre that is connected to a spectrometer. This gives a measured plasma density varied between 1×10^{19} and 2×10^{19} cm^{-3} with average value 1.71×10^{19} cm^{-3}.

The design and initial testing of a set of 10 filters to make a Ross pair measurement of the radiation spectrum has been presented and testing of the analysis script has shown that the spectrum can be measured for critical energies between 5 and 25 keV. This technique can be easily expanded to higher photon energies with a careful choice of other material pairs with close x-ray edges > 25 keV, for example those used by Powers et al., for points between 40 and 90 keV [213]. The Ross pair filter measurements were unsuccessful due to the lower electron energy, than anticipated, which resulted in the choice of materials not being optimised for low photon energies. When the laser is re-optimised and experiments begin in Bunker A with the 350 TW laser this method will give reliable measurements of the radiation spectrum. Working Ross pair measurements would allow the spectrum to be measured in a single shot and the image can be analysed immediately, in a time shorter than the laser inter-pulse repetition period, which will provide feedback on the spectrum critical energy and intensity that can be used to optimising the set up (gas jet position, compressor grating separation etc.) before a data collection run.

Chapter 8

Conclusion

This thesis presents experimental studies on the emission of hard and soft x-ray radiation from the laser wakefield accelerator. A spectrometer based on a Rowland circle design has been used to measure the spectrum of the extreme ultraviolet (XUV) radiation emitted directly from the plasma. Three metal filters are used to block the laser, while ensuring transmission in selected regions of the spectrum. Broadband XUV radiation is measured between 3 and 31 nm (40 and 400 eV) with the spectrometer, which is verified by measurements using interference patterns from double slits. The brightness of the radiation is significant, with peak values of 3.952 $\mathrm{mJ\,eV^{-1}\,sr^{-1}}$ or 1.5×10^{16} photons $\mathrm{sr^{-1}}$ at 166 eV (7.5 nm) in a single laser shot.

The emission process results in a three order of magnitude shot-to-shot variations in the number of photons detected, which may be connected to the emission process or beam pointing but random fluctuations in experimental conditions (laser parameters and plasma density) also have an impact, although were not investigated. Modulations and multi-peaked features are observed in the majority of recorded spectra. These fall into two categories. The first category of spectra have a small number of modulations (2 to 4 peaks) with a spacing of 30 eV. The second category have a larger number of modulations that have an average separation between peaks of 11 eV. The emission of XUV radiation from the plasma seems to be rare and only $\sim 4.4\%$ of laser shots giving radiation in the solid angle of the spectrometer for photons with energy greater than the aluminium L edge > 17 nm (< 73 eV). However, to date, measurements have not

been made to investigate whether XUV radiation is being emitted at an angle relative to the path of the high power laser similar to the measurements made by Pirozhkov et al., [154–156], which may account for the missing shots.

Single shot direct measurements of the XUV radiation have been made by reflecting the XUV radiation into the CCD camera using a beamsplitter that transmits the hard x-ray betatron radiation and most of the infrared laser light. Measurements of the number of photons on the CCD camera compare well with the measurements using the spectrometer, where on average 1.0×10^{14} photons sr^{-1} was measured with the best shot containing 2.7×10^{15} photons sr^{-1}. The XUV radiation divergence has been estimated using the CCD camera placed at its closest possible position to the gas jet. The XUV beam is elliptical with a FWHM divergence of (12.0 ± 1.0) mrad along the major axis and (7.1 ± 0.40) mrad along the minor axis. However, this is likely an underestimate due to the large number of images that were much larger than the detector and resulting in the fitting process not converging. Furthermore, the centroid of the beam is often outside the detection area of the CCD chip.

Using the same set up, three Young's double slits with different slit separations have been used to measure the transverse coherence of XUV beam, from the interference pattern, which allows the source size of the radiation to be calculated. For the Al, Zr and In filters and with a double slit of separation 150 µm, the average source size diameter is estimated to be 57.8 µm, 46.5 µm and 32.0 µm, respectively assuming the source is circular or Gaussian. The obtained value compares well to the measured laser focus spot size in vacuum of 53×57 µm. This is likely to be an upper limit of the source size due to the large bandwidth of the radiation passing through the filters as well as background signal on the CCD camera. Furthermore, the source size appears to shrink for smaller number of XUV photons.

The measurements of the spectrum, profile and source size allow the peak brilliance of the source to be estimated, the maximum number of photons measured in a single laser shot within the solid angle of the spectrometer and the Al filter was 1.38×10^{7} photons/0.1% BW occurring at 7.5 nm. The peak brilliance has been calculated using three possible values of the pulse duration, since a measurement has not been

made, 11 as for a Fourier limited pulse, 1 fs corresponding to the electron bunch duration [70] and 35 fs corresponding to the laser pulse duration. The results are summarised in table 8.1. A pulse duration of 1 fs gives a peak brilliance equivalent to third generation light sources such as SPRING-8, and BESSY-II [214].

Pulse duration	**Peak brilliance** (photons/s/mm^2/mrad^2/0.1% BW)
11 as	6.4×10^{27}
1 fs	7.1×10^{25}
35 fs	2.0×10^{24}

Table 8.1: Calculated peak brightness for possible XUV pulse durations of Fourier limited, electron duration and laser pulse duration, assuming a source diameter of 50 µm and divergence defined by the entrance slit of the spectrometer of 0.026×3.87 mrad^2.

The properties of the measured XUV radiation presented in the thesis share some features of those observed by Pirozhkov et al., [154–156]. However, there are also a number of important differences, which suggests that the source of the XUV radiation emitted in the experiments presented in the thesis is not the same as observed in the Pirozhkov et al. measurements.

In the first two experiments [154, 155], the Japanese team demonstrated the emission of XUV radiation in for forward direction (parallel to the laser direction) using both a 9 and 120 TW laser and plasma densities between 1.5 and 9.6×10^{19} cm^{-3} which is in the same range as the Strathclyde measurements. For the 120 TW, a brightness of ≈ 100 µJ eV^{-1} sr^{-1} at 120 eV is measured and the spectrum brightness was shown to decrease exponentially with photon energy. The ALPHA-X measurements are far more peaked and the analysis of the spectral peak in each shot shows an upward trend in spectral brightness with photon energy, in contrast to the Pirozhkov et al. measurements. In the same window as the Japanese measurements, with a zirconium filter, the average peak brightness is (163 ± 32) µJ eV^{-1} sr^{-1}, which around $> 50\%$ larger with a third of the laser power. The similarities between these sets of measurements are the photon energy ranges, 40 to 400 eV at Strathclyde, and 60 to 350 eV by Pirozhkov et al. The Strathclyde results also exhibit similar modulations in the spectrum. Although the measurements in this thesis show no evidence of the 1 eV modulations observed by Pirozhkov corresponding to harmonics of the high power laser frequency, both sets of

results exhibit modulations with a larger spacing, 5 to 10 eV observed in Japan, and an average of 11 eV at ALPHA-X, but the larger modulations, up to 70 eV, have not been observed by Pirozhkov et al.

The more recent experiments from the Japanese groups [156] discovered that the XUV radiation is most intense at 13° from the laser axis where measurements were made between 8 and 18°. By imaging the source with a spherical mirror, they showed that the radiation arises from two radiators separated by the bubble diameter. In contrast the source size measurements presented in this thesis show that the XUV radiation observed at ALPHA-X has a much larger source size than the bubble size, and is approximately equal to the vacuum laser spot size measured at high power however this is based on the assumption that the source shape is circular or Gaussian. If this assumption is shown to be incorrect, then a ring or double point source gives a source diameter closer to but still larger than the bubble size. For example, assuming the source is a two point sources gives an average size of 28.5 µm for the Aluminium filter. The next set of experiments to probe the XUV emission process will investigate emission at non-zero angles relative to the laser propagation direction as well as imaging the source to obtain the size and geometry with the KB. It should therefore be concluded that XUV radiation presented in this thesis is likely to originate from a different mechanism to the one proposed by Pirozhkov et al., due to the significantly higher spectral brightness, peaked spectra which contrasts with the photon number dependence on photon energy that Pirozhkov et al. observe and the source size much larger than the bubble diameter.

A Kirkpatrick-Baez microscope based on a pair of curved mirrors has been installed and tested in preparation for future experiments that require high brightness radiation or to focus the radiation onto a target. A convenient method of optimising the grazing angle by balancing the reflectivity of the platinum mirrors and aperture of the KB, is described. A simple alignment procedure is given for optimising the mirror grazing angle based on geometric arguments based on reflections off the mirrors and beams that by-pass the mirrors. The ability of the KB to focus light is tested using a HeNe laser for two test grazing angles, optimised for XUV and betatron radiation. Focusing of the HeNe was achieved and it is found that the KB focuses the light to a spot size closer to

the calculated value when the mirror radius of curvature is small, suggesting that the mirror flatness and errors in the mirror shape when under stress limits the fidelity of the KB focussing system and blurs the focal spots. Further testing is required to quantify the errors in the mirror shape and deviations from the expected values. Measurement of the mirror flatness with a Zygo interferometer before they are glued to the holder or attached to the mounts or benders show that the peak-to-trough flatness is 5.5 µm and 6.6 µm over their 152.4 mm (6 inch) length for the entrance and exit mirrors respectively.

As part of a commissioning experiment for the ALPHA-X beamline at the SCAPA laboratory, the spectrum of x-ray radiation arising from betatron oscillations of electrons in a plasma wake have been measured. A pixelated CCD camera is calibrated to measure the energy of photons emitted from a ^{241}Am sealed source using a single photon counting technique. Relatively thick aluminium filters are used to block the laser beam and attenuate the betatron radiation to a flux suitable for the single photon counting method, which has been used to reconstruct the radiation spectrum. A critical energy of 2.9 keV is measured, which is consistent with the measured plasma density from the Raman peaks of the backscattered laser radiation and electron energy measured with the bending magnet spectrometer, when the betatron amplitude is assumed to be around half of the bubble radius. However, due to the poor transmission through the filters used to block the high power laser pulse of photons less than 2 keV, it is not clear that the detected radiation is purely betatron radiation. A second method, a Ross pair filter method, which as an independent check of the betatron critical energy is presented. This is based on pairs of filters with different materials that have closely spaced x-ray K edges. A set of 10 filter materials combined into 5 pairs is chosen to measure spectra between 1.5 keV and 19.5 keV. The range of filter materials is chosen to be suitable for a range of critical energies of previous measurements using another detector and higher electron energy. However, it was not possible to successfully test the Ross pair method because of the unusually low electron energy, and thus the betatron critical energies, for laser operation in the new SCAPA lab. Work is currently in progress to optimise the laser and thus the betatron critical energy.

8.1 Outlook and future work

This thesis investigates the properties of the extreme ultraviolet radiation produced by the plasma which can be used to help identify the physical process that underlies the emission and develop a theoretical model, which is currently lacking. The observations should help in the development of the model by providing information about the source including the bandwidth, brightness of the source and the presence and separation between the modulations. While work is continuing on theoretical models there is a lot of scope for continuing experimental work to further probe the emission process. For instance, the scaling of the XUV brilliance and photon energy with plasma and laser parameters (pulse energy, duration, spectrum etc.) could be investigated using the new 350 TW laser in the SCAPA facility. During any future experiments, the properties of the laser should be closely monitored to determine why only a small number of laser shots contain measurable XUV radiation. For instance, the laser pointing, energy and spectrum could all be monitored on a shot-to-shot basis from leakage through a mirror close to the focusing optic. The pointing of the XUV beam should also be closely monitored as this would have a large impact on the number of photons entering the slit of the spectrometer which may partially explain the shot to shot instability of the beam brightness. Scaling with the plasma density should also be investigated, which could be achieved using the newly designed spectrometer to measure Raman backscattered radiation, installed for the betatron spectrum measurements in chapter 7 or via interferometry with a probe pulse.

A bright XUV source, such as the one presented in this thesis, has a number of possible applications in science and industry including ultrafast spectroscopy [215], femtochemistry [216], femto-biology [217], condensed matter physics [218], atomic physics [56] and high resolution imaging using either Fourier transform holography [190, 219–222] or coded aperture imaging [191, 223]. All of these potential applications require a coherent x-ray beam and high brightness which have both been demonstrated within this thesis. Although some important properties of the radiation beam are currently unknown (such as the pulse duration), the source is sufficiently well characterised for

proof of principle experiments to take place and compared to other sources such as undulator radiation. Once a theoretical model is produced that describes the emission process, the XUV source can be optimised where the possibility exists to extend the emission into the water window where a range of experiments with biological samples can be performed.

The measurements in this thesis could be improved by exchanging the CCD camera for a much higher resolution detector, such as colour centres in lithium fluoride (LiF) crystals. This would have a number of advantages, the resolution of the measurements would only be limited by the resolution of the fluorescence microscope used to read out the crystals [224–226], which can be sub-micrometre. This would be a particular advantage for the double slit measurements because much more data will be available for the Fourier transform of the interference pattern, which may allow features such as the modulations in the spectrum to be directly measured. LiF crystals have been demonstrated to have a high dynamic range and therefore saturation, even after hundreds of laser shots, should not be a concern [227, 228]. Lithium fluoride is also transparent to photons with energy less than 14 eV [224], therefore the infra-red light of the high power laser pulse not be detected removing the need for high pass filters. Removing the need to block the laser, removes the chance of damaging filters and detectors, and therefore measurements can be made much closer to the source of the radiation and profile measurements will utilise the full diameter of the beam. However, LiF has the limitation that the crystals must be removed from the beamline to be read out by a fluorescence microscope, and then annealed via thermoluminescence before reusing, which limits the total number of shots that can be taken in a single day of measurements.

A new set of double slits have been precisely manufactured to obtain improved inference pattern data where the widths of the slits and separations are more consistent. The set has 5 slits with the same width and varying separation between 20 and 120 µm so that the source geometry can be obtained by fitting the visibility as a function of slit separation to the models of the different candidate source shapes.

Direct measurements of the XUV source size and geometry may also be possible with the Kirkpatrick Baez microscope in high magnification mode using a CCD camera,

or in the low magnification mode using a LiF crystal, these measurements will give the an independent check of the source size from the double slits and the source geometry to test the assumption of a Gaussian distribution made in this thesis and to test if there is two spots, similar to the measurements by Pirozhkov [156]. A direct measurement of the source shape will help to guide the theoretical description by ruling out some mechanisms and processes.

List of Figures

List of Tables

List of Tables

Bibliography

[1] G. Aad, T. Abajyan, B. Abbott, et al. Observation of a new particle in the search for the standard model higgs boson with the atlas detector at the lhc. *Physics Letters B*, 716(1):1–29, 2012.

[2] S. Chatrchyan, V. Khachatryan, A.M. Sirunyan, et al. Observation of a new boson at a mass of 125 gev with the cms experiment at the lhc. *Physics Letters B*, 716(1):30–61, 2012.

[3] K.R. Hogstrom and P.R. Almond. Review of electron beam therapy physics. *Physics in Medicine & Biology*, 51(13):455, 2006.

[4] W.D. Newhauser and R. Zhang. The physics of proton therapy. *Physics in Medicine & Biology*, 60(8):155, 2015.

[5] M.C. Lagunas-Solar, P.M. Kiefer, O.F. Carvacho, C.A. Lagunas, and Y.P. Cha. Cyclotron production of nca 99mtc and 99mo. an alternative non-reactor supply source of instant 99mtc and 99mo to 99mtc generators. *International Journal of Radiation Applications and Instrumentation. Part A. Applied Radiation and Isotopes*, 42(7):643 – 657, 1991.

[6] R. Mehnert. Review of industrial applications of electron accelerators. *Nuclear Instruments and Methods in Physics Research Section B: Beam Interactions with Materials and Atoms*, 113(1):81 – 87, 1996. Accelerators in Applied Research and Technology.

[7] J.D. Jackson. *Classical electrodynamics*. Wiley, New York, NY, 3rd ed. edition, 1999.

[8] P.R. Ribic and G. Margaritondo. Status and prospects of x-ray free-electron lasers (x-fels): a simple presentation. *Journal of Physics D: Applied Physics*, 45(21):213001, 2012.

[9] B.W.J. McNeil and N.R. Thompson. X-ray free-electron lasers. *Nature photonics*, 4(12):814, 2010.

[10] E.A. Seddon, J.A. Clarke, D.J. Dunning, et al. Short-wavelength free-electron laser sources and science: a review. *Reports on Progress in Physics*, 80(11):115901, 2017.

[11] M.P. Tooley, B. Ersfeld, S.R. Yoffe, et al. Towards attosecond high-energy electron bunches: Controlling self-injection in laser-wakefield accelerators through plasma-density modulation. *Phys. Rev. Lett.*, 119:044801, Jul 2017.

[12] M. K. Weikum. *Generation, acceleration and measurement of attosecond electron beams from laser-plasma accelerators.* PhD thesis, Department of Physics, University of Strathclyde, Glasgow, 2017.

[13] T.J.M. Boyd and J.J. Sanderson. *The Physics of Plasmas.* Cambridge University Press, 2003.

[14] T. Tajima and J.M. Dawson. Laser electron accelerator. *Phys. Rev. Lett.*, 43:267–270, Jul 1979.

[15] D. Strickland and G. Mourou. Compression of amplified chirped optical pulses. *Optics Communications*, 56(3):219 – 221, 1985.

[16] A. Modena, Z. Najmudin, A.E. Dangor, et al. Electron acceleration from the breaking of relativistic plasma waves. *nature*, 377(6550):606, 1995.

[17] P. Sprangle, E. Esarey, J. Krall, and G. Joyce. Propagation and guiding of intense laser pulses in plasmas. *Phys. Rev. Lett.*, 69:2200–2203, Oct 1992.

[18] E. Esarey, J. Krall, and P. Sprangle. Envelope analysis of intense laser pulse self-modulation in plasmas. *Phys. Rev. Lett.*, 72:2887–2890, May 1994.

[19] K. Nakajima, D. Fisher, T. Kawakubo, et al. Observation of ultrahigh gradient electron acceleration by a self-modulated intense short laser pulse. *Phys. Rev. Lett.*, 74:4428–4431, May 1995.

[20] C.A. Coverdale, C.B. Darrow, C.D. Decker, et al. Propagation of intense subpicosecond laser pulses through underdense plasmas. *Phys. Rev. Lett.*, 74:4659–4662, Jun 1995.

[21] R. Wagner, S.-Y. Chen, A. Maksimchuk, and D. Umstadter. Electron acceleration by a laser wakefield in a relativistically self-guided channel. *Phys. Rev. Lett.*, 78:3125–3128, Apr 1997.

[22] D. Umstadter, J.K. Kim, and E. Dodd. Laser injection of ultrashort electron pulses into wakefield plasma waves. *Phys. Rev. Lett.*, 76:2073–2076, Mar 1996.

[23] N.E. Andreev, L.M. Gorbunov, V.I. Kirsanov, AA Pogosova, and RR Ramazashvili. The theory of laser self-resonant wake field excitation. *Physica Scripta*, 49(1):101, 1994.

[24] M.N. Rosenbluth and C.S. Liu. Excitation of plasma waves by two laser beams. *Phys. Rev. Lett.*, 29:701–705, Sep 1972.

[25] Y. Kitagawa, T. Matsumoto, T. Minamihata, et al. Beat-wave excitation of plasma wave and observation of accelerated electrons. *Phys. Rev. Lett.*, 68:48–51, Jan 1992.

[26] C.E. Clayton, K.A. Marsh, A. Dyson, et al. Ultrahigh-gradient acceleration of injected electrons by laser-excited relativistic electron plasma waves. *Phys. Rev. Lett.*, 70:37–40, Jan 1993.

[27] M. Everett, A. Lal, D. Gordon, et al. Trapped electron acceleration by a laser-driven relativistic plasma wave. *Nature*, 368(6471):527, 1994.

[28] D. Umstadter, S.-Y. Chen, A. Maksimchuk, G. Mourou, and R. Wagner. Nonlinear optics in relativistic plasmas and laser wake field acceleration of electrons. *Science*, 273(5274):472–475, 1996.

[29] C. Gahn, G.D. Tsakiris, A. Pukhov, et al. Multi-mev electron beam generation by direct laser acceleration in high-density plasma channels. *Phys. Rev. Lett.*, 83:4772–4775, Dec 1999.

[30] V. Malka, S. Fritzler, E. Lefebvre, et al. Electron acceleration by a wake field forced by an intense ultrashort laser pulse. *Science*, 298(5598):1596–1600, 2002.

[31] S.P.D. Mangles, C.D. Murphy, Z. Najmudin, et al. Monoenergetic beams of relativistic electrons from intense laser–plasma interactions. *Nature*, 431(7008):535, 2004.

[32] J. Faure, Y. Glinec, A. Pukhov, et al. A laser–plasma accelerator producing monoenergetic electron beams. *Nature*, 431(7008):541, 2004.

[33] C.G.R. Geddes, Cs. Toth, J. Van Tilborg, et al. High-quality electron beams from a laser wakefield accelerator using plasma-channel guiding. *Nature*, 431(7008):538, 2004.

[34] A. Pukhov and J. Meyer-ter Vehn. Laser wake field acceleration: the highly non-linear broken-wave regime. *Applied Physics B*, 74(4):355–361, Apr 2002.

[35] A. J. Gonsalves, K. Nakamura, J. Daniels, et al. Petawatt laser guiding and electron beam acceleration to 8 gev in a laser-heated capillary discharge waveguide. *Phys. Rev. Lett.*, 122:084801, Feb 2019.

[36] X. Wang, R. Zgadzaj, N. Fazel, et al. Quasi-monoenergetic laser-plasma acceleration of electrons to 2 gev. *Nature communications*, 4:1988, 2013.

[37] W.P. Leemans, A.J. Gonsalves, H.-S. Mao, et al. Multi-gev electron beams from capillary-discharge-guided subpetawatt laser pulses in the self-trapping regime. *Phys. Rev. Lett.*, 113:245002, Dec 2014.

[38] S. Bulanov, N. Naumova, F. Pegoraro, and J. Sakai. Particle injection into the wave acceleration phase due to nonlinear wake wave breaking. *Phys. Rev. E*, 58:R5257–R5260, Nov 1998.

[39] H. Suk, N. Barov, J.B. Rosenzweig, and E. Esarey. Plasma electron trapping and acceleration in a plasma wake field using a density transition. *Phys. Rev. Lett.*, 86:1011–1014, Feb 2001.

[40] K. Schmid, A. Buck, C.M.S. Sears, et al. Density-transition based electron injector for laser driven wakefield accelerators. *Phys. Rev. ST Accel. Beams*, 13:091301, Sep 2010.

[41] J. Faure, C. Rechatin, O. Lundh, L. Ammoura, and V. Malka. Injection and acceleration of quasimonoenergetic relativistic electron beams using density gradients at the edges of a plasma channel. *Physics of Plasmas*, 17(8):083107, 2010.

[42] M. Hansson, B. Aurand, X. Davoine, et al. Down-ramp injection and independently controlled acceleration of electrons in a tailored laser wakefield accelerator. *Phys. Rev. ST Accel. Beams*, 18:071303, Jul 2015.

[43] K.K. Swanson, H.-E. Tsai, S.K. Barber, et al. Control of tunable, monoenergetic laser-plasma-accelerated electron beams using a shock-induced density downramp injector. *Phys. Rev. Accel. Beams*, 20:051301, May 2017.

[44] M. Chen, Z.M. Sheng, Y.Y. Ma, and J. Zhang. Electron injection and trapping in a laser wakefield by field ionization to high-charge states of gases. *Journal of Applied Physics*, 99(5):056109, 2006.

[45] E. Oz, S. Deng, T. Katsouleas, et al. Ionization-induced electron trapping in ultrarelativistic plasma wakes. *Phys. Rev. Lett.*, 98:084801, Feb 2007.

[46] M. Chen, E. Esarey, C.B. Schroeder, C.G.R. Geddes, and W.P. Leemans. Theory of ionization-induced trapping in laser-plasma accelerators. *Physics of Plasmas*, 19(3):033101, 2012.

[47] C. McGuffey, A.G.R. Thomas, W. Schumaker, et al. Ionization induced trapping in a laser wakefield accelerator. *Phys. Rev. Lett.*, 104:025004, Jan 2010.

[48] A. Buck, J. Wenz, J. Xu, et al. Shock-front injector for high-quality laser-plasma acceleration. *Phys. Rev. Lett.*, 110:185006, May 2013.

[49] B.B. Pollock, C.E. Clayton, J.E. Ralph, et al. Demonstration of a narrow energy spread, ~ 0.5 GeV electron beam from a two-stage laser wakefield accelerator. *Phys. Rev. Lett.*, 107:045001, Jul 2011.

[50] D.A. Jaroszynski and G. Vieux. Coherent radiation sources based on laser plasma accelerators. *AIP Conference Proceedings*, 647(1):902–914, 2002.

[51] D.A. Jaroszynski, R. Bingham, E. Brunetti, et al. Radiation sources based on laser–plasma interactions. *Philosophical Transactions of the Royal Society of London A: Mathematical, Physical and Engineering Sciences*, 364(1840):689–710, 2006.

[52] F. Albert and A.G.R. Thomas. Applications of laser wakefield accelerator-based light sources. *Plasma Physics and Controlled Fusion*, 58(10):103001, 2016.

[53] S. Kneip, C. McGuffey, F. Dollar, et al. X-ray phase contrast imaging of biological specimens with femtosecond pulses of betatron radiation from a compact laser plasma wakefield accelerator. *Applied Physics Letters*, 99(9):093701, 2011.

[54] J.M. Cole, J.C. Wood, N.C. Lopes, et al. Laser-wakefield accelerators as hard x-ray sources for 3d medical imaging of human bone. *Scientific Reports*, 5:13244, 2015.

[55] J. Wenz, S. Schleede, K. Khrennikov, et al. Quantitative x–ray phase-contrast microtomography from a compact laser–driven betatron source. *Nature communications*, 6:7568, 2015.

[56] M.Z. Mo, Z. Chen, S. Fourmaux, et al. Laser wakefield generated x-ray probe for femtosecond time-resolved measurements of ionization states of warm dense aluminum. *Review of Scientific Instruments*, 84(12):123106, 2013.

[57] A. Subiel, V. Moskvin, G.H. Welsh, et al. Dosimetry of very high energy electrons (vhee) for radiotherapy applications: using radiochromic film measurements and monte carlo simulations. *Physics in Medicine & Biology*, 59(19):5811, 2014.

[58] M.P. Anania, E. Brunetti, S.M. Wiggins, et al. An ultrashort pulse ultra-violet radiation undulator source driven by a laser plasma wakefield accelerator. *Applied Physics Letters*, 104(26):264102, 2014.

[59] C.P. Jones, C.M. Brenner, C.A. Stitt, et al. Evaluating laser-driven bremsstrahlung radiation sources for imaging and analysis of nuclear waste packages. *Journal of hazardous materials*, 318:694–701, 2016.

[60] B. Hidding, O. Karger, T. Königstein, et al. Laser-plasma-based space radiation reproduction in the laboratory. *Scientific reports*, 7:42354, 2017.

[61] E. Esarey, B.A. Shadwick, P. Catravas, and W.P. Leemans. Synchrotron radiation from electron beams in plasma-focusing channels. *Phys. Rev. E*, 65:056505, May 2002.

[62] I. Kostyukov, S. Kiselev, and A. Pukhov. X-ray generation in an ion channel. *Physics of Plasmas*, 10(12):4818–4828, 2003.

[63] S. Cipiccia, M.R. Islam, B. Ersfeld, et al. Gamma-rays from harmonically resonant betatron oscillations in a plasma wake. *Nature Physics*, 7(11):867, 2011.

[64] H.-P. Schlenvoigt, K. Haupt, A. Debus, et al. A compact synchrotron radiation source driven by a laser-plasma wakefield accelerator. *Nature Phys.*, 4:130–133, 2008.

[65] M. Fuchs, R. Weingartner, A. Popp, et al. Laser-driven soft-x-ray undulator source. *Nature Phys.*, 5:826–829, 2009.

[66] S. Cipiccia, S.M. Wiggins, R.P. Shanks, et al. A tuneable ultra-compact high-power, ultra-short pulsed, bright gamma-ray source based on bremsstrahlung radiation from laser-plasma accelerated electrons. *Journal of Applied Physics*, 111(6):063302, 2012.

[67] R.D. Edwards, M.A. Sinclair, T.J. Goldsack, et al. Characterization of a gamma-ray source based on a laser-plasma accelerator with applications to radiography. *Applied Physics Letters*, 80(12):2129–2131, 2002.

[68] A. Giulietti, N. Bourgeois, T. Ceccotti, et al. Intense γ-ray source in the giant-dipole-resonance range driven by 10-tw laser pulses. *Phys. Rev. Lett.*, 101:105002, Sep 2008.

[69] Y. Glinec, J. Faure, L. Le Dain, et al. High-resolution γ-ray radiography produced by a laser-plasma driven electron source. *Phys. Rev. Lett.*, 94:025003, Jan 2005.

[70] M.R. Islam, E. Brunetti, R.P. Shanks, et al. Near-threshold electron injection in the laserplasma wakefield accelerator leading to femtosecond bunches. *New Journal of Physics*, 17(9):093033, 2015.

[71] X. Yang, E. Brunetti, D.R. Gil, et al. Three electron beams from a laser-plasma wakefield accelerator and the energy apportioning question. *Scientific reports*, 7:43910, 2017.

[72] X. Yang, E. Brunetti, and D.A. Jaroszynski. High-energy coherent terahertz radiation emitted by wide-angle electron beams from a laser-wakefield accelerator. *New Journal of Physics*, 20(4):043046, 2018.

[73] P. Sprangle, A. Ting, E. Esarey, and A. Fisher. Tunable, short pulse hard xrays from a compact laser synchrotron source. *Journal of Applied Physics*, 72(11):5032–5038, 1992.

[74] H. Schwoerer, B. Liesfeld, H.-P. Schlenvoigt, K.-U. Amthor, and R. Sauerbrey. Thomson-backscattered x rays from laser-accelerated electrons. *Phys. Rev. Lett.*, 96:014802, Jan 2006.

[75] K. Ta Phuoc, S. Corde, C. Thaury, et al. All-optical compton gamma-ray source. *Nature Photonics*, 6(5):308, 2012.

[76] C. Liu, G. Golovin, S. Chen, et al. Generation of 9 mev γ-rays by all-laser-driven compton scattering with second-harmonic laser light. *Opt. Lett.*, 39(14):4132–4135, Jul 2014.

[77] C. Yu, R. Qi, W. Wang, et al. Ultrahigh brilliance quasi-monochromatic mev g-rays based on self-synchronized all-optical compton scattering. *Scientific Reports*, 6:29518, Jul 2016. Article.

[78] A. Döpp, E. Guillaume, C. Thaury, et al. An all-optical compton source for single-exposure x-ray imaging. *Plasma Physics and Controlled Fusion*, 58(3):034005, 2016.

[79] H-E. Tsai, X. Wang, J. Shaw, et al. Compact tunable compton x-ray source from laser wakefield accelerator and plasma mirror. *AIP Conference Proceedings*, 1777(1):080006, 2016.

[80] Constantin Aniculaesei. *Experimental studies of laser plasma wakefield acceleration.* PhD thesis, Department of Physics, University of Strathclyde, Glasgow, 2015.

[81] D.J. Spence and S.M. Hooker. Investigation of a hydrogen plasma waveguide. *Phys. Rev. E*, 63:015401, Dec 2000.

[82] D.J. Spence, A. Butler, and S.M. Hooker. First demonstration of guiding of high-intensity laser pulses in a hydrogen-filled capillary discharge waveguide. *Journal of Physics B: Atomic, Molecular and Optical Physics*, 34(21):4103, 2001.

[83] S. Abuazoum, S. M. Wiggins, R. C. Issac, et al. A high voltage pulsed power supply for capillary discharge waveguide applications. *Review of Scientific Instruments*, 82(6):063505, 2011.

[84] T.P.A. Ibbotson, N. Bourgeois, T.P. Rowlands-Rees, et al. Investigation of the role of plasma channels as waveguides for laser-wakefield accelerators. *New Journal of Physics*, 12(4):045008, 2010.

[85] D.G. Jang, M.S. Kim, I.H. Nam, H.S. Uhm, and H. Suk. Density evolution measurement of hydrogen plasma in capillary discharge by spectroscopy and interferometry methods. *Applied Physics Letters*, 99(14):141502, 2011.

[86] S. Abuazoum, S.M. Wiggins, B. Ersfeld, et al. Linearly tapered discharge capillary waveguides as a medium for a laser plasma wakefield accelerator. *Applied Physics Letters*, 100(1):014106, 2012.

[87] S.M. Wiggins, M.P. Reijnders, S. Abuazoum, et al. Note: Femtosecond laser micromachining of straight and linearly tapered capillary discharge waveguides. *Rev. Sci. Instrum.*, 82(9), 2011.

[88] K. Nakajima. Plasma-wave resonator for particle-beam acceleration. *Phys. Rev. A*, 45:1149–1156, Jan 1992.

[89] V.I. Berezhiani and I.G. Murusidze. Interaction of highly relativistic short laser pulses with plasmas and nonlinear wake-field generation. *Physica Scripta*, 45(2):87, 1992.

[90] S.M. Hooker, R. Bartolini, S.P.D. Mangles, et al. Multi-pulse laser wakefield acceleration: a new route to efficient, high-repetition-rate plasma accelerators and high flux radiation sources. *Journal of Physics B: Atomic, Molecular and Optical Physics*, 47(23):234003, 2014.

[91] C.W. Siders, J.L.W. Siders, A.J. Taylor, S-G. Park, and A.M. Weiner. Efficient high-energy pulse-train generation using a 2n-pulse michelson interferometer. *Appl. Opt.*, 37(22):5302–5305, Aug 1998.

[92] J. Cowley, C. Thornton, C. Arran, et al. Excitation and control of plasma wakefields by multiple laser pulses. *Phys. Rev. Lett.*, 119:044802, Jul 2017.

[93] C.I. Moore, A. Ting, K. Krushelnick, et al. Electron trapping in self-modulated laser wakefields by raman backscatter. *Phys. Rev. Lett.*, 79:3909–3912, Nov 1997.

[94] D. Gordon, K.C. Tzeng, C.E. Clayton, et al. Observation of electron energies beyond the linear dephasing limit from a laser-excited relativistic plasma wave. *Phys. Rev. Lett.*, 80:2133–2136, Mar 1998.

[95] V. Malka, J. Faure, J.R. Marques, et al. Characterization of electron beams

produced by ultrashort (30 fs) laser pulses. *Physics of Plasmas*, 8(6):2605–2608, 2001.

[96] E. Esarey, R.F. Hubbard, W.P. Leemans, A. Ting, and P. Sprangle. Electron injection into plasma wakefields by colliding laser pulses. *Phys. Rev. Lett.*, 79:2682–2685, Oct 1997.

[97] S.Ya. Tochitsky, R. Narang, C.V. Filip, et al. Enhanced acceleration of injected electrons in a laser-beat-wave-induced plasma channel. *Phys. Rev. Lett.*, 92:095004, Mar 2004.

[98] S.Ya. Tochitsky, R. Narang, C.V. Filip, et al. Experiments on laser driven beat-wave acceleration in a ponderomotively formed plasma channel. *Physics of Plasmas*, 11(5):2875–2881, 2004.

[99] T. Katsouleas. Physical mechanisms in the plasma wake-field accelerator. *Phys. Rev. A*, 33:2056–2064, Mar 1986.

[100] I. Blumenfeld, C.E. Clayton, F-J Decker, et al. Energy doubling of 42 gev electrons in a metre-scale plasma wakefield accelerator. *Nature*, 445:741, Feb 2007.

[101] R. Assmann, R. Bingham, and T. others Bohl. Proton-driven plasma wakefield acceleration: a path to the future of high-energy particle physics. *Plasma Physics and Controlled Fusion*, 56(8):084013, 2014.

[102] E. Gschwendtner, E. Adli, L. Amorim, et al. Awake, the advanced proton driven plasma wakefield acceleration experiment at cern. *Nuclear Instruments and Methods in Physics Research Section A: Accelerators, Spectrometers, Detectors and Associated Equipment*, 829:76 – 82, 2016. 2nd European Advanced Accelerator Concepts Workshop - EAAC 2015.

[103] E. Adli, A. Ahuja, O. Apsimon, et al. Acceleration of electrons in the plasma wakefield of a proton bunch. *Nature*, 2018.

[104] M. Gross, J. Engel, J. Good, et al. Observation of the self-modulation instability via time-resolved measurements. *Phys. Rev. Lett.*, 120:144802, Apr 2018.

[105] A. Macchi, M. Borghesi, and M. Passoni. Ion acceleration by superintense laser-plasma interaction. *Rev. Mod. Phys.*, 85:751–793, May 2013.

[106] H. Daido, M. Nishiuchi, and A.S. Pirozhkov. Review of laser-driven ion sources and their applications. *Reports on Progress in Physics*, 75(5):056401, 2012.

[107] S.C. Wilks, A.B. Langdon, T.E. Cowan, et al. Energetic proton generation in ultra-intense lasersolid interactions. *Physics of Plasmas*, 8(2):542–549, 2001.

[108] A. Higginson, R.J. Gray, M. King, et al. Near-100 mev protons via a laser-driven transparency-enhanced hybrid acceleration scheme. *Nature communications*, 9(1):724, 2018.

[109] F. Wagner, O. Deppert, C. Brabetz, et al. Maximum proton energy above 85 mev from the relativistic interaction of laser pulses with micrometer thick ch_2 targets. *Phys. Rev. Lett.*, 116:205002, May 2016.

[110] J. Denavit. Absorption of high-intensity subpicosecond lasers on solid density targets. *Phys. Rev. Lett.*, 69:3052–3055, Nov 1992.

[111] T. Esirkepov, M. Borghesi, S.V. Bulanov, G. Mourou, and T. Tajima. Highly efficient relativistic-ion generation in the laser-piston regime. *Phys. Rev. Lett.*, 92:175003, Apr 2004.

[112] V.A. Vshivkov, N.M. Naumova, F. Pegoraro, and S.V. Bulanov. Nonlinear electrodynamics of the interaction of ultra-intense laser pulses with a thin foil. *Physics of Plasmas*, 5(7):2727–2741, 1998.

[113] B. Gonzalez-Izquierdo, M. King, R.J. Gray, et al. Towards optical polarization control of laser-driven proton acceleration in foils undergoing relativistic transparency. *Nature communications*, 7:12891, 2016.

[114] B. Gonzalez-Izquierdo, R.J. Gray, M. King, et al. Optically controlled dense current structures driven by relativistic plasma aperture-induced diffraction. *Nature Physics*, 12(5):505, 2016.

[115] J. Meyer-ter Vehn, A. Pukhov, and Z-M. Sheng. *Relativistic Laser Plasma Interaction: Atoms, Solids, and Plasmas in Super-Intense Laser Fields*. Springer US, Boston, MA, 2001.

[116] W.L. Kruer. *The Physics of Laser Plasma Interactions*. Addison-Wesley, Redwood City, CA, 1988.

[117] E. Esarey, C.B. Schroeder, and W.P. Leemans. Physics of laser-driven plasma-based electron accelerators. *Rev. Mod. Phys.*, 81:1229–1285, Aug 2009.

[118] D. Bauer, P. Mulser, and W.-H. Steeb. Relativistic ponderomotive force, uphill acceleration, and transition to chaos. *Phys. Rev. Lett.*, 75:4622–4625, Dec 1995.

[119] B. Quesnel and P. Mora. Theory and simulation of the interaction of ultraintense laser pulses with electrons in vacuum. *Phys. Rev. E*, 58:3719–3732, Sep 1998.

[120] L.M. Gorbunov and V.I. Kirsanov. Excitation of plasma waves by an electromagnetic wave packet. *Sov. Phys. JETP*, 66(290-294):40, 1987.

[121] V. Malka. Plasma wake accelerators: Introduction and historical overview. *arXiv preprint arXiv:1705.09584*, 2017.

[122] J.M. Dawson. Nonlinear electron oscillations in a cold plasma. *Phys. Rev.*, 113:383–387, Jan 1959.

[123] R. Lehe, M. Kirchen, I.A. Andriyash, B.B. Godfrey, and J-L Vay. A spectral, quasi-cylindrical and dispersion-free particle-in-cell algorithm. *Computer Physics Communications*, 203:66 – 82, 2016.

[124] I. Kostyukov, A. Pukhov, and S. Kiselev. Phenomenological theory of laser-plasma interaction in bubble regime. *Physics of Plasmas*, 11(11):5256–5264, 2004.

[125] W. Lu, C. Huang, M. Zhou, W.B. Mori, and T. Katsouleas. Nonlinear theory for relativistic plasma wakefields in the blowout regime. *Phys. Rev. Lett.*, 96:165002, Apr 2006.

[126] P. Mora and T.M. Antonsen. Electron cavitation and acceleration in the wake of an ultraintense, self-focused laser pulse. *Phys. Rev. E*, 53:R2068–R2071, Mar 1996.

[127] S. Gordienko and A. Pukhov. Scalings for ultrarelativistic laser plasmas and quasimonoenergetic electrons. *Physics of Plasmas*, 12(4):043109, 2005.

[128] W. Lu, M. Tzoufras, C. Joshi, et al. Generating multi-gev electron bunches using single stage laser wakefield acceleration in a 3d nonlinear regime. *Phys. Rev. ST Accel. Beams*, 10:061301, Jun 2007.

[129] D. Kaganovich, A. Ting, D.F. Gordon, et al. First demonstration of a staged all-optical laser wakefield acceleration. *Physics of Plasmas*, 12(10):100702, 2005.

[130] V. Malka, A. Lifschitz, J. Faure, and Y. Glinec. Staged concept of laser-plasma acceleration toward multi-gev electron beams. *Phys. Rev. ST Accel. Beams*, 9:091301, Sep 2006.

[131] H.T. Kim, K.H. Pae, H.J. Cha, et al. Enhancement of electron energy to the multi-gev regime by a dual-stage laser-wakefield accelerator pumped by petawatt laser pulses. *Phys. Rev. Lett.*, 111:165002, Oct 2013.

[132] S. Steinke, J. van Tilborg, C. Benedetti, et al. Multistage coupling of independent laser-plasma accelerators. *Nature*, 530:190 – 193, Feb 2016.

[133] S. Steinke, J. van Tilborg, C. Benedetti, et al. Staging of laser-plasma accelerators. *Physics of Plasmas*, 23(5):056705, 2016.

[134] J. Luo, M. Chen, W.Y. Wu, et al. Multistage coupling of laser-wakefield accelerators with curved plasma channels. *Phys. Rev. Lett.*, 120:154801, Apr 2018.

[135] E. Esarey, B.A. Shadwick, C.B. Schroeder, and W.P. Leemans. Nonlinear pump depletion and electron dephasing in laser wakefield accelerators. In *AIP Conference Proceedings*, volume 737, pages 578–584. AIP, 2004.

[136] B.A. Shadwick, C.B. Schroeder, and E. Esarey. Nonlinear laser energy depletion in laser-plasma accelerators. *Physics of Plasmas*, 16(5):056704, 2009.

[137] P. Sprangle, J.R. Peano, B. Hafizi, et al. Gev acceleration in tapered plasma channels. *Physics of Plasmas*, 9(5):2364–2370, 2002.

[138] W. Rittershofer, C. B. Schroeder, E. Esarey, et al. Tapered plasma channels to phase-lock accelerating and focusing forces in laser-plasma accelerators. *Physics of Plasmas*, 17(6):063104, 2010.

[139] E. Esarey, P. Sprangle, J. Krall, and A. Ting. Self-focusing and guiding of short laser pulses in ionizing gases and plasmas. *IEEE Journal of Quantum Electronics*, 33(11):1879–1914, Nov 1997.

[140] K. Ta Phuoc, F. Burgy, J-P Rousseau, et al. Laser based synchrotron radiation. *Physics of Plasmas*, 12(2):8, 2005.

[141] F. Albert, R. Shah, K. Phuoc, et al. Betatron oscillations of electrons accelerated in laser wakefields characterized by spectral x-ray analysis. *Phys. Rev. E*, 77:056402, May 2008.

[142] Y. Glinec, J. Faure, A. Lifschitz, et al. Direct observation of betatron oscillations in a laser-plasma electron accelerator. *EPL (Europhysics Letters)*, 81(6):64001, 2008.

[143] S. Corde, K. Ta Phuoc, G. Lambert, et al. Femtosecond x rays from laser-plasma accelerators. *Rev. Mod. Phys.*, 85:1–48, Jan 2013.

[144] D.H. Whittum. Electromagnetic instability of the ion-focused regime. *Physics of Fluids B: Plasma Physics*, 4(3):730–739, 1992.

[145] G.N. Kulipanov. Ginzburg's invention of undulators and their role in modern synchrotron radiation sources and free electron lasers. *Physics-Uspekhi*, 50(4):368, 2007.

[146] H. Motz. Applications of the radiation from fast electron beams. *Journal of Applied Physics*, 22(5):527–535, 1951.

[147] H. Motz, W. Thon, and R.N. Whitehurst. Experiments on radiation by fast electron beams. *Journal of Applied Physics*, 24(7):826–833, 1953.

[148] J.A. Clarke. *The science and technology of undulators and wigglers*. Number 4. Oxford University Press, 2004.

[149] S. Kneip, C. McGuffey, J.L. Martins, et al. Bright spatially coherent synchrotron x-rays from a table-top source. *Nature Physics*, 6(12):980, 2010.

[150] M. Schnell, A. Sävert, B. Landgraf, et al. Deducing the electron-beam diameter in a laser-plasma accelerator using x-ray betatron radiation. *Phys. Rev. Lett.*, 108:075001, Feb 2012.

[151] S. Kiselev, A. Pukhov, and I. Kostyukov. X-ray generation in strongly nonlinear plasma waves. *Phys. Rev. Lett.*, 93:135004, Sep 2004.

[152] S.P.D. Mangles, A.G.R. Thomas, M.C. Kaluza, et al. Laser-wakefield acceleration of monoenergetic electron beams in the first plasma-wave period. *Phys. Rev. Lett.*, 96:215001, May 2006.

[153] W. Yan, L. Chen, D. Li, et al. Concurrence of monoenergetic electron beams and bright x-rays from an evolving laser-plasma bubble. *Proceedings of the National Academy of Sciences*, 111(16):5825–5830, 2014.

[154] A.S. Pirozhkov, M. Kando, T.Zh. Esirkepov, et al. Soft-x-ray harmonic comb from relativistic electron spikes. *Phys. Rev. Lett.*, 108:135004, Mar 2012.

[155] A.S. Pirozhkov, M. Kando, T.Z. Esirkepov, et al. High order harmonics from relativistic electron spikes. *New Journal of Physics*, 16(9):093003, 2014.

[156] A.S. Pirozhkov, T.Z. Esirkepov, T.A. Pikuz, et al. Burst intensification by singularity emitting radiation in multi-stream flows. *Scientific reports*, 7(1):17968, 2017.

[157] T.A. Pikuz, A. Faenov, A. Pirozhkov, et al. High performance imaging of relativistic soft x-ray harmonics by sub-micron resolution lif film detectors. *physica status solidi c*, 9(12):2331–2335, 2012.

[158] V. Malka, J. Faure, Y. Glinec, and C. Rechatin. Principle and applications of electron beams produced with laser plasma accelerators. In *Journal of Physics: Conference Series*, volume 112, page 042029. IOP Publishing, 2008.

[159] K.W.D. Ledingham, P.R. Bolton, N. Shikazono, and C-M.C. Ma. Towards laser driven hadron cancer radiotherapy: A review of progress. *Applied Sciences*, 4(3):402–443, 2014.

[160] K. Kokurewicz et al. Focused vhees for radiotherapy. submitted.

[161] A. Maksimchuk, S. Gu, K. Flippo, D. Umstadter, and V. Yu. Bychenkov. Forward ion acceleration in thin films driven by a high-intensity laser. *Phys. Rev. Lett.*, 84:4108–4111, May 2000.

[162] E.L. Clark, K. Krushelnick, J.R. Davies, et al. Measurements of energetic proton transport through magnetized plasma from intense laser interactions with solids. *Phys. Rev. Lett.*, 84:670–673, Jan 2000.

[163] R.A. Snavely, M.H. Key, S.P. Hatchett, et al. Intense high-energy proton beams from petawatt-laser irradiation of solids. *Phys. Rev. Lett.*, 85:2945–2948, Oct 2000.

[164] S. Backus, C.G. Durfee III, M.M. Murnane, and H.C. Kapteyn. High power ultrafast lasers. *Review of scientific instruments*, 69(3):1207–1223, 1998.

[165] D.A. Jaroszynski, B. Ersfeld, G. Giraud, et al. The strathclyde terahertz to optical pulse source (tops). *Nuclear Instruments and Methods in Physics Research Section A: Accelerators, Spectrometers, Detectors and Associated Equipment*, 445(1):317 – 319, 2000.

[166] D.E. Spence, P.N. Kean, and W. Sibbett. 60-fsec pulse generation from a self-mode-locked ti: sapphire laser. *Optics letters*, 16(1):42–44, 1991.

[167] G.D. Reid and K. Wynne. Ultrafast laser technology and spectroscopy. *Encyclopedia of Analytical chemistry*, 2000.

[168] J.D. Simon. Ultrashort light pulses. *Review of scientific instruments*, 60(12):3597–3624, 1989.

[169] A. Major, F. Yoshino, I. Nikolakakos, et al. Dispersion of the nonlinear refractive index in sapphire. *Optics letters*, 29(6):602–604, 2004.

[170] P.M.W. French, D.U. Noske, N.H. Rizvi, J.A.R. Williams, and J.R. Taylor. Characterisation of a cw titanium-doped sapphire laser mode-locked with a linear external cavity. *Optics Communications*, 83(1):185 – 194, 1991.

[171] N.H. Rizvi, P.M.W. French, and J.R. Taylor. Continuously self-mode-locked ti: sapphire laser that produces sub-50-fs pulses. *Optics letters*, 17(4):279–281, 1992.

[172] A. Offner. Unit power imaging catoptric anastigmat, jul 1973. US Patent 3,748,015.

[173] D. Du, J. Squier, S. Kane, et al. Terawatt ti:sapphire laser with a spherical reflective-optic pulse expander. *Opt. Lett.*, 20(20):2114–2116, Oct 1995.

[174] G. Cheriaux, P. Rousseau, F. Salin, et al. Aberration-free stretcher design for ultrashort-pulse amplification. *Opt. Lett.*, 21(6):414–416, Mar 1996.

[175] E. Treacy. Optical pulse compression with diffraction gratings. *IEEE Journal of Quantum Electronics*, 5(9):454–458, Sep 1969.

[176] Maria Pia Anania. *Towards a free-electron laser driven by a laser wakefield accelerator*. PhD thesis, Department of Physics, University of Strathclyde, Glasgow, 2014.

[177] Parker hannifin corporation. `http://www.parker.com/portal/site/PARKER/`. Accessed October, 8 2018.

[178] Cross section of ccd pixel from andor. `https://andor.oxinst.com/learning/view/article/low-dark-current-deep-depletion-(ldc-dd)-technology`. Accessed 27th January 2019.

[179] C. A. Klein. Bandgap dependence and related features of radiation ionization energies in semiconductors. *Journal of Applied Physics*, 39(4):2029–2038, 1968.

[180] G.W. Fraser, A.F. Abbey, A. Holland, K. McCarthy, A. Owens, and A. Wells. The x-ray energy response of silicon part a. theory. *Nuclear Instruments and Methods in Physics Research Section A: Accelerators, Spectrometers, Detectors and Associated Equipment*, 350(1):368 – 378, 1994.

[181] F. Scholze, H. Rabus, and G. Ulm. Mean energy required to produce an electron-hole pair in silicon for photons of energies between 50 and 1500 ev. *Journal of Applied Physics*, 84(5):2926–2939, 1998.

[182] L. Poletto, A. Boscolo, and G. Tondello. Characterization of a charge-coupled-device detector in the 1100–0.14-nm (1-ev to 9-kev) spectral region. *Appl. Opt.*, 38(1):29–36, Jan 1999.

[183] M.S. del Río and R.J. Dejus. Xop v2.4: recent developments of the x-ray optics software toolkit. In *Advances in Computational Methods for X-Ray Optics II*, volume 8141, page 814115. International Society for Optics and Photonics, 2011.

[184] D.L. Windt. Imdsoftware for modeling the optical properties of multilayer films. *Computers in Physics*, 12(4):360–370, 1998.

[185] Luxel corporation. `https://luxel.com/`. Accessed May, 8 2018.

[186] B. P. Abbott et al. Observation of gravitational waves from a binary black hole merger. *Phys. Rev. Lett.*, 116:061102, Feb 2016.

[187] Y.M. Li and R. Fedosejevs. Density measurements of a high-density pulsed gas jet for laser-plasma interaction studies. *Measurement Science and Technology*, 5(10):1197, 1994.

[188] S. Fourmaux, S. Corde, K. Ta Phuoc, et al. Single shot phase contrast imaging using laser-produced betatron x-ray beams. *Opt. Lett.*, 36(13):2426–2428, Jul 2011.

[189] I. McNulty, J. Kirz, C. Jacobsen, et al. High-resolution imaging by fourier transform x-ray holography. *Science*, 256(5059):1009–1012, 1992.

[190] W.F. Schlotter, R. Rick, K. Chen, et al. Multiple reference fourier transform holography with soft x rays. *Applied Physics Letters*, 89(16):163112, 2006.

[191] S. Marchesini, S. Boutet, A.E. Sakdinawat, et al. Massively parallel x-ray holography. *Nature photonics*, 2(9):560, 2008.

[192] T. Young. II. The Bakerian lecture. On the theory of light and colours. *Philosophical transactions of the Royal Society of London*, 92:12–48, 1802.

[193] F.L. Pedrotti, L.M. Pedrotti, and L.S. Pedrotti. *Introduction to Optics*. Pearson Education Inc., 3 edition, 2007.

[194] E. Hecht. *Optics*. Pearson Education, 5th ed. edition, 2016.

[195] J.W. Goodman. *Statistical Optics*. John Wiley & Sons, 1985.

[196] A. R. Attar, A. Bhattacherjee, C. D. Pemmaraju, et al. Femtosecond x-ray spectroscopy of an electrocyclic ring-opening reaction. *Science*, 356(6333):54–59, 2017.

[197] Y. Pertot, C. Schmidt, M. Matthews, et al. Time-resolved x-ray absorption spectroscopy with a water window high-harmonic source. *Science*, 355(6322):264–267, 2017.

[198] D. Popmintchev, B. R. Galloway, M-C Chen, et al. Near- and extended-edge x-ray-absorption fine-structure spectroscopy using ultrafast coherent high-order harmonic supercontinua. *Phys. Rev. Lett.*, 120:093002, Mar 2018.

[199] P. Kirkpatrick and A.V. Baez. Formation of optical images by x-rays. *J. Opt. Soc. Am.*, 38(9):766–774, Sep 1948.

[200] H. Mimura, S. Matsuyama, H. Yumoto, et al. Hard x-ray diffraction-limited nanofocusing with kirkpatrick-baez mirrors. *Japanese Journal of Applied Physics*, 44(4L):L539, 2005.

[201] H. Yumoto, H. Mimura, T. Koyama, et al. Focusing of x-ray free-electron laser pulses with reflective optics. *Nature Photonics*, 7(1):43, 2013.

[202] Zygo corporation. `https://www.zygo.com/`. Accessed September, 23 2018.

[203] B.R. Maddox, H.S. Park, B.A. Remington, and M. McKernan. Calibration and characterization of single photon counting cameras for short-pulse laser experiments. *Review of Scientific Instruments*, 79(10):10E924, 2008.

[204] C. Fourment, N. Arazam, C. Bonte, et al. Broadband, high dynamics and high resolution charge coupled device-based spectrometer in dynamic mode for multi-kev repetitive x-ray sources. *Review of Scientific Instruments*, 80(8):083505, 2009.

[205] T.M.V. Bootsma, E.J. van Zwet, A.C. Brinkman, et al. Synchrotron calibration and response modelling of back-illuminated xmm-rgs ccds. *Nuclear Instruments and Methods in Physics Research Section A: Accelerators, Spectrometers, Detectors and Associated Equipment*, 439(2):575 – 581, 2000.

[206] A. Owens, T. Mineo, K.J. McCarthy, and A. Wells. Event recognition in x-ray ccds. *Nuclear Instruments and Methods in Physics Research Section A: Accelerators, Spectrometers, Detectors and Associated Equipment*, 346(1):353 – 365, 1994.

[207] D. Reboredo, S. Cipiccia, P. A. Grant, G.H. Welsh, et al. Phase-contrast imaging using radiation sources based on laser-plasma wakefield accelerators: state of the art and future development. *Proc.SPIE*, 9412:9412 – 9412 – 8, 2015.

[208] David Reboredo Gil. *Imaging Applications from a Laser Wakefield Accelerator*. PhD thesis, Department of Physics, University of Strathclyde, Glasgow, 2017.

[209] P.A. Ross. A new method of spectroscopy for faint x-radiations. *J. Opt. Soc. Am.*, 16(6):433–437, Jun 1928.

[210] P. Kirkpatrick. On the theory and use of ross filters. *Review of Scientific Instruments*, 10(6):186–191, 1939.

[211] M. Schnell, A. Sävert, I. Uschmann, et al. Characterization and application of hard x-ray betatron radiation generated by relativistic electrons from a laser-wakefield accelerator. *Journal of Plasma Physics*, 81(4):475810401, 2015.

[212] B.D. Arhatari, T.E. Gureyev, and B. Abbey. Elemental contrast x-ray tomography using ross filter pairs with a polychromatic laboratory source. *Scientific reports*, 7(1):218, 2017.

[213] N.D. Powers, I. Ghebregziabher, G. Golovin, et al. Quasi-monoenergetic and tunable x-rays from a laser-driven compton light source. *Nature Photonics*, 8:28 – 31, Nov 2013.

[214] D.H. Bilderback, P. Elleaume, and E. Weckert. Review of third and next generation synchrotron light sources. *Journal of Physics B: Atomic, Molecular and Optical Physics*, 38(9):S773, 2005.

[215] G.C. Walker, W. Jarzeba, T.J. Kang, A.E. Johnson, and P.F. Barbara. Ultraviolet femtosecond fluorescence spectroscopy: techniques and applications. *J. Opt. Soc. Am. B*, 7(8):1521–1527, Aug 1990.

[216] A.H. Zewail. Femtochemistry: atomic-scale dynamics of the chemical bond. *The Journal of Physical Chemistry A*, 104(24):5660–5694, 2000.

[217] V. Sundström. Femtobiology. *Annual Review of Physical Chemistry*, 59(1):53–77, 2008. PMID: 17892434.

[218] I.A. Vartanyants, I.K. Robinson, I. McNulty, et al. Coherent x-ray scattering and lensless imaging at the european xfel facility. *Journal of Synchrotron Radiation*, 14(6):453–470, Nov 2007.

[219] S. Eisebitt, J. Lüning, W.F. Schlotter, et al. Lensless imaging of magnetic nanostructures by x-ray spectro-holography. *Nature*, 432(7019):885, 2004.

[220] H.N. Chapman, A. Barty, M.J. Bogan, et al. Femtosecond diffractive imaging with a soft-x-ray free-electron laser. *Nature Physics*, 2(12):839, 2006.

[221] C.M. Günther, B. Pfau, R. Mitzner, et al. Sequential femtosecond x-ray imaging. *Nature Photonics*, 5(2):99, 2011.

[222] J. Geilhufe, B. Pfau, M. Schneider, et al. Monolithic focused reference beam x-ray holography. *Nature communications*, 5:3008, 2014.

[223] A. Haboub, A.A. MacDowell, S. Marchesini, and D.Y. Parkinson. Coded aperture imaging for fluorescent x-rays. *Review of Scientific Instruments*, 85(6):063704, 2014.

[224] G. Baldacchini, S. Bollanti, F. Bonfigli, et al. Soft x-ray submicron imaging detector based on point defects in lif. *Review of Scientific Instruments*, 76(11):113104, 2005.

[225] A.Ya. Faenov, Y. Kato, M. Tanaka, et al. Submicrometer-resolution in situ imaging of the focus pattern of a soft x-ray laser by color center formation in lif crystal. *Opt. Lett.*, 34(7):941–943, Apr 2009.

[226] R.M. Montereali, F. Bonfigli, M. Piccinini, E. Nichelatti, and M.A. Vincenti. Photoluminescence of colour centres in lithium fluoride thin films: From solid-state miniaturised light sources to novel radiation imaging detectors. *Journal of Luminescence*, 170:761 – 769, 2016. Light, Energy and Life.

[227] T.A. Pikuz, A. Faenov, Y. Fukuda, et al. Optical features of a lif crystal soft x-ray imaging detector irradiated by free electron laser pulses. *Opt. Express*, 20(4):3424–3433, Feb 2012.

[228] T.A. Pikuz, A.Y. Faenov, Y. Fukuda, et al. Soft x-ray free-electron laser imaging by lif crystal and film detectors over a wide range of fluences. *Appl. Opt.*, 52(3):509–515, Jan 2013.